Ionospheric Scintillation Prediction, Modeling, and Observation Techniques for the August 2017 Solar Eclipse

Kayla Nicole Brosie

Thesis submitted to the Faculty of the

Virginia Polytechnic Institute and State University

in partial fulfillment of the requirements for the degree of

Master of Science

in

Electrical Engineering

Gregory D. Earle, Co-Chair

Robert W. McGwier, Co-Chair

Michael R. Buehrer

Wayne A. Scales

June 30, 2017

Blacksburg, Virginia

Keywords: ionospheric scintillation, solar eclipse, temperature gradient instability, ionospheric instabilities

Ionospheric Scintillation Prediction, Modeling, and Observation Techniques for the August 2017 Solar Eclipse

Kayla Nicole Brosie

Academic Abstract

A total solar eclipse is happening on August 21, 2017 and will be visible for a range of states across the contiguous United States. The solar eclipse is expected to cause changes in the ionosphere, mainly in the electron density and electron temperature, that may lead to scintillation. Ionospheric scintillation is the rapid amplitude and phase fluctuations of a signal caused by irregularities in the electron density in the ionosphere. Ionospheric scintillation is a known phenomenon for equatorial and polar regions of the Earth, but is less common in mid-latitude regions. To that end, this work discusses scintillation receiver development, both hardware and software, to be used in Idaho, Nebraska, and Tennessee to record scintillation during the solar eclipse. Downlinks from NOAA 15, NOAA 18, NOAA 19, SARSAT 7, SARSAT 10, SARSAT 12, and Inmarsat are used to measure scintillation. This work also models a temperature gradient instability (TGI) during normal conditions and under the conditions that may be present due to the solar eclipse. This TGI may grow due to changes in the ionosphere caused by the solar eclipse, thereby causing ionospheric scintillation. A prediction of scintillation is drawn from the models of the instability.

Ionospheric Scintillation Prediction, Modeling, and Observation Techniques for the August 2017 Solar Eclipse

Kayla Nicole Brosie

General Audience Abstract

A full solar eclipse is going to be visible from a range of states in the contiguous United States on August 21, 2017. Since the atmosphere of the Earth is charged by the sun, the blocking of the sunlight by the moon may cause short term changes to the atmosphere, such as density and temperature alterations. There are many ways to measure these changes, one of these being ionospheric scintillation. Ionospheric scintillation is rapid amplitude and phase fluctuations of signals passing through the ionosphere caused by electron density irregularities in the ionosphere. At mid-latitudes, scintillation is not as common of an occurrence as it is in equatorial or high-altitude regions. One of the theories that this paper looks into is the possibility of the solar eclipse producing an instability in the ionosphere that will cause the mid-latitude region to experience scintillations that would not normally be present. Instabilities that could produce scintillation are reviewed and altered further to model similar conditions to those that might occur during the solar eclipse. From this, the satellites that are being used are discuses, as is hardware and software tools were developed to record the scintillation measurements. Although this work was accomplished before the eclipse occurred, measurement tools were developed and verified along with generating a model that predicted if the solar eclipse will produce an instability large enough to cause scintillation for high frequency satellite downlinks.

Contents

List of Figures

List of Tables

Chapter 1

Introduction

1.1 Motivation

On August 21, 2017 a full solar eclipse will be passing over the contiguous United States, with the path of totality passing through 14 states stretching from Oregon to South Carolina [5]. During a total solar eclipse the moon passes between the sun and the Earth, blocking the sun from view. A partial eclipse differs from a total eclipse by only blocking a portion of the sun. Although eclipses themselves are common, with at least one visible a year somewhere in the world [4], a total solar eclipse is less common. A total solar eclipse can be seen about once every eighteen months at some point on Earth, but the last total solar eclipse that was visible in the contiguous United States was in 1979 [6].

Not only is the total eclipse a rarity for those in the contiguous United States, it will also have effects on the Earth's ionosphere. The ionosphere is the ionized portion of Earth's upper atmosphere, where free ions and electrons coexist with the atmospheric neutral gases [2].

The Earth's ionosphere is produced by solar ultraviolet and extreme ultraviolet radiation, therefore the blockage of the sunlight to the ionosphere by the moon during the solar eclipse will cause changes to occur. These disturbances can include a number of effects, the most important of which are electron density and temperature variations. The perturbations caused by the eclipse may differ greatly from those that occur at sunset and sunrise, and research of these perturbations has long been studied [7–14], but such perturbations are still not fully understood.

To remedy this, a group at Space@VirginiaTech is working on a model of how the solar eclipse might alter the ionosphere. The model is important because some communications, such as satellite and amateur radio, interact with and/or depend upon the ionosphere for their signals to get to their rightful destination. For example, amateur radio operators (hams) routinely use refractive effects in the ionosphere to transmit signals over long distances [15].To test this model, multiple types of measurements are to be made during the eclipse, including maximum usable frequency (MUF) for communication between two points, ionosondes, and scintillation receivers. Ionospheric scintillation is random phase and amplitude fluctuations caused by small scale structures in the ionosphere. The focus of this thesis is to investigate whether scintillation is likely to arise due to instabilities created by the solar eclipse, and the development of tools to record scintillation if it occurs.

1.2 Contributions

The work described in this thesis considers the development of scintillation receivers (i.e., receivers made for the purpose of measuring ionospheric scintillation) for the August 21, 2017 solar eclipse as well as scintillation predictions based upon instabilities introduced by the eclipse. Chapter 2 discusses the relationship between the ionosphere, ionospheric scintillation, and the role that the sunspot cycle plays in each. It highlights communication effects of scintillation as well as introducing the concept software defined radios and the use of GNU Radio.

Chapter 3 begins with an introduction to the model that will be used throughout this work. The Temperature Gradient Instability (TGI) and Gradient Drift Instability (GDI) are introduced in Chapter 3 and linked to the development of scintillations. Each of these instabilities can be modeled in kinetic theory using MATLAB, although only the TGI is considered for this work as it is the instability with the largest growth rate for expected eclipse conditions. The TGI models are used to predict performance for normal conditions, if the eclipse were not occurring, and then the effects of the eclipse are imposed by changing the electron density of the ionosphere during the eclipse using previous eclipse responses as a guide. This technique allows conclusions to be drawn about the driving factors that cause instabilities that may produce scintillation. These model results are then compared to investigate whether ionospheric scintillation is likely to occur during the solar eclipse.

Chapter 4 describes the setup of the scintillation receivers for the eclipse. The chapter

starts with a discussion of the satellites that are being used in the study and why they were chosen. The physical locations of the scintillation receivers are described, as well as the look angles associated with each site. The look angles and access times for each location were found using System Tool Kit (STK) and the simulation is highlighted for accuracy. Finally, the chapter describes the hardware and software measurement tools that are used for the receivers, and considers how the receivers will be set up during the eclipse.

Chapter 5 presents the measurements that were taken before the eclipse under normal ionospheric conditions. The tool to measure scintillation indexes is introduced and the steps taken to further validate the data are discussed. These measurements are then analyzed and compared with the theoretical values of scintillation for the region. From this comparison the measurements are able to be validated to ensure that when the eclipse occurs, the analysis of received scintillation is accurate. This effort is meant to verify the scintillation measurement tools rather than the models, as under normal conditions TGI is not large enough to introduce scintillations at the frequencies of interest. Therefore, it cannot be validated until the eclipse.

The final chapters, Chapter 6 and 7, summarize the work that has been done to date to prepare for the August 21, 2017 total solar eclipse. This is also where the future work on the project is discussed and where recommendations are made for moving forward with the work. Ultimately, since the entire project is based upon the August 2017 solar eclipse, the next step is to deploy the scintillation receivers to their designated locations to take data for the eclipse. Beyond that, additional simulations could be ran and combined with the TGI model to have an all-encompassing instability model. The takeaway from this work is to

introduce a TGI model that predicts ionospheric scintillation during the August 2017 solar eclipse and tools that will measure the received scintillations.

Chapter 2

Background

2.1 Ionospheric Science

This chapter examines ionospheric scintillation and the role sunspot cycle and the ionosphere play in producing it. Alongside that, software defined radios are discussed and GNU Radio is introduced.

2.1.1 Sunspot Cycle

The Sun is the driving factor in the creation of free electrons and ionized molecules in the ionosphere, therefore the activity associated with the Sun is important to keep in mind when discussing ionospheric scintillation. Sunspot number is the measure of the Sun's activity and is used to quantify the solar radiation intensity at ionizing wavelengths [3]. The sunspot number is still used today, even though it can be subjective, because it is the only metric of solar activity that dates back centuries [16]. There is a daily sunspot number associated

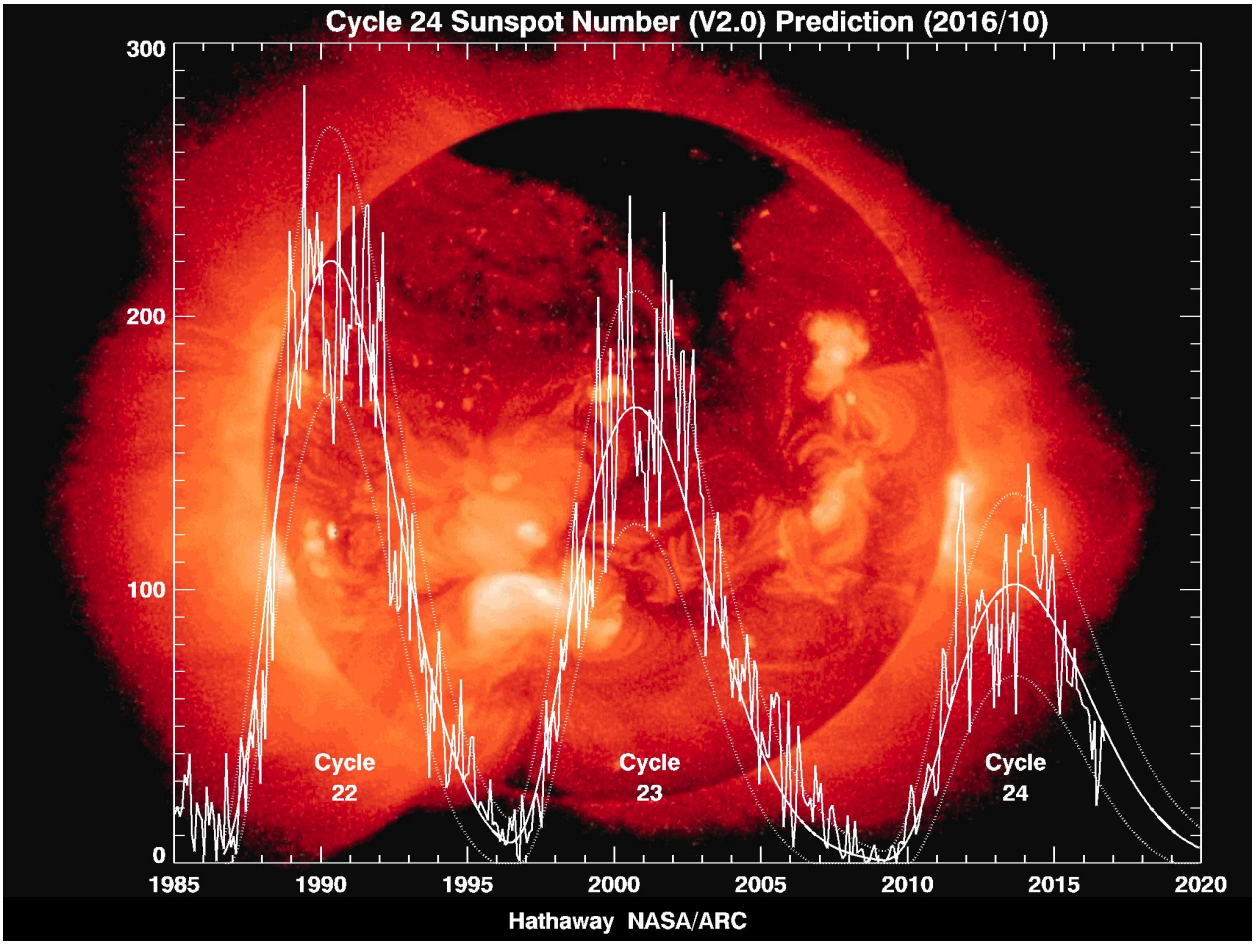

Figure 2.1: The current sunspot cycle, 24, along with past measurements of cycle 22 and 23 [1].

with the number of sunspots seen on a given day. This value can be added over monthly time frames, and this monthly value in turn plotted over years. This produces a graphical representation of the sunspot cycle, as shown in Figure 2.1.

Notice that the year 2017 falls towards the bottom of cycle 24, though not at its predicted minimum. The expectation from this information is that there will be fewer disturbances in the ionosphere in 2017 compared to an average year or a year that falls near a maximum in

the cycle. This is because the lower activity of the sun corresponds to a less dense and less dynamic ionosphere where instabilities are less likely to occur. If a monthly sunspot number falls below 30, then ionospheric scintillation may be nonexistent at frequencies above 1 GHz [3].

The exception to this statement would be if a geomagnetic storm were to occur in 2017, causing more disturbances in the ionosphere than would be expected for a typical day near solar minimum. In short, a geomagnetic storm is caused by an intense dissipation of solar wind energy into Earth's atmosphere. Geomagnetic storms can lead to large-scale ionospheric density perturbations [17] For this work it is assumed there are no geomagnetic storms that are to occur during the August 21, 2017 eclipse. Since storms are less prevalent during solar minimum this assumption is likely to be valid. If a storm does occur on the eclipse date its role in causing scintillations would need to be accounted for in further analysis.

The variability of the sunspot number gives predicted values associated with it, such as ionospheric scintillation, a large margin of error. Scintillation, in the form being used here, does not directly depend on the sunspot number. However, sunspot number and other values associated with it are used in modeling predictions of ionospheric parameters, as discussed in 3.1.1. These values are assumed to be low due to the closeness in the sunspot cycle to a minimum.

2.1.2 Earth's Ionosphere

The Earth's ionosphere is a region of ionized plasma in the Earth's upper atmosphere that is roughly defined at altitudes 60-000 km above the Earth's surface [18]. Ultraviolet and X-radiation from the Sun creates the ionized plasma found here [19]. The ionosphere is an important component of Earth's atmosphere because of its effect on electromagnetic signals. The ionosphere causes alterations to the time varying electromagnetic fields of a signal by allowing the flow of electric currents. This layer of the Earth's atmosphere alters the signal by refraction, reflection, attenuation, or rotation of the plane of polarization [2].

A mix of quasi-neutral gases make up the ionosphere, as shown in Figure 2.2. This figure shows that the electron density, e^-, is equal to the sum of the positive ion densities so that the gases remain electrically neutral on macroscopic scales [2]. From the gas composition, a classification of regions of the ionosphere can be drawn, as seen in Table 2.1. It should be noted that the heights associated with these regions change throughout the day, seasonally, and based on solar activity, and therefore should be considered approximations. Figure 2.3 provides a global view of how the thickness and altitude of the layers can vary from day to night. This figure shows how the ionosphere changes from day to night, which can be used to limit the work presented here to only the F region in the ionosphere between 200 km - 650 km.

These variations cause the ionosphere's density peak to fluctuate between $1-30 \text{ x } 10^{11} \text{m}^{-3}$ at roughly 220-400 km [2]. Scintillation primarily occurs in the F region, more specifically

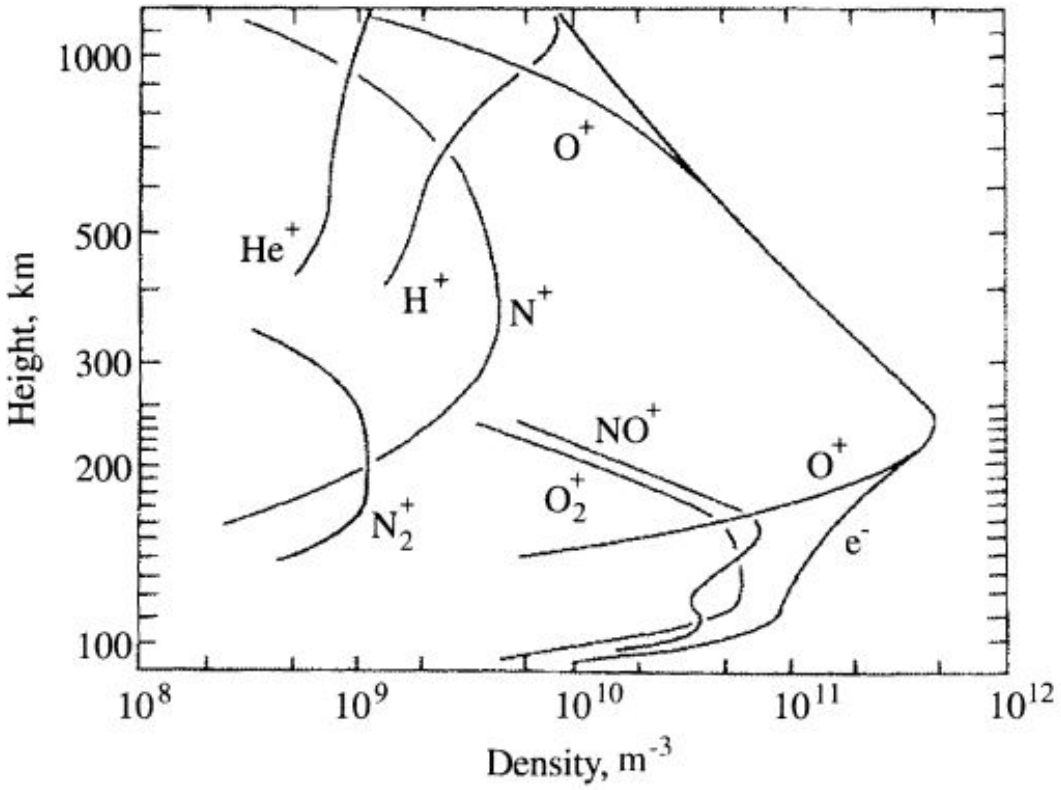

Figure 2.2: Composition of Ionosphere with Postive Ion and Electron Densities [2].

near the peak of the plasma density [20]. The variations due to time, season, and solar activity also create the plasmasphere, where H^+ starts to dominate the ion composition. This occurs between 600-2,000 km [2]. For this reason, the work presented here will not consider heights above 650 km as scintillations are less likely to occur in the plasmasphere.

Figure 2.4 compares the neutral gas temperature, T_n, ion temperature, T_i, and electron temperature, T_e. Above a height of 150 km the electron temperature breaks away from the neutral gas temperature, while the ion temperature continues to closely match the neutral gas temperature until 350 km. The ion temperature continues in thermal equilibrium

Ionosphere		
Region	Height Estimations	Primary Ions
D Region	<90 km km	H_3O^+, $(H_2O)_n$, NO_3^-
E Region	90 - 170 km	O_2^+, NO^+
F Region	170 - 1000 km	O^+
Plasmasphere	>1000 km	H^+

Table 2.1: Regions of the Ionosphere Estimated by Composition

with the neutrals over a larger range of altitudes because of the efficiency of momentum transform between ions and neutrals, and because the electrons are directly stimulated by solar radiation. Similar masses of ions and neutral particles is conducive to energy and momentum exchange, so the ions and neutrals have similar temperatures at altitudes where collisions are common. Since electrons and ions interact through Coulomb collisions and can absorb solar energy at extreme ultraviolet wavelengths, their temperatures continue to increase with altitude. The ion temperature will not reach the electron temperature, but will tend toward it due to electromagnetic collisions. The different temperatures of the three gas components result in a continual heat flux from the electrons to the ions and from the ions to the neutral gas [2]. However, this is no longer true at nighttime, when the three temperatures are roughly equal below 500 km [2].

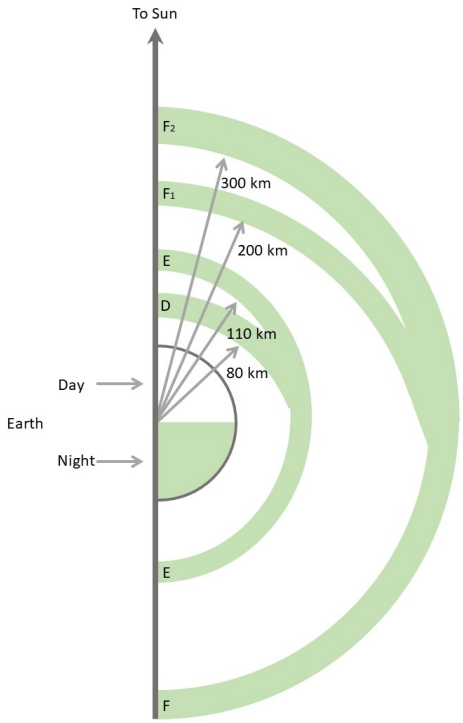

Figure 2.3: Change in ionosphere regions as a function of time, based on those shown in Allnutt [3].

2.1.3 Ionospheric Scintillation

Irregularities in the electron density cause the refractive index of the ionosphere to fluctuate, thereby causing signals passing through to experience scattering and refraction. This scattering can be in the form of rapid phase and amplitude fluctuations, otherwise known as scintillation [21]. One of the primary causes of irregularities in the ionosphere can be traced to plasma instabilities [22]. Though phase and amplitude fluctuations are the common outcomes of scintillation, a signal can also experience a change in direction of propagation and polarization

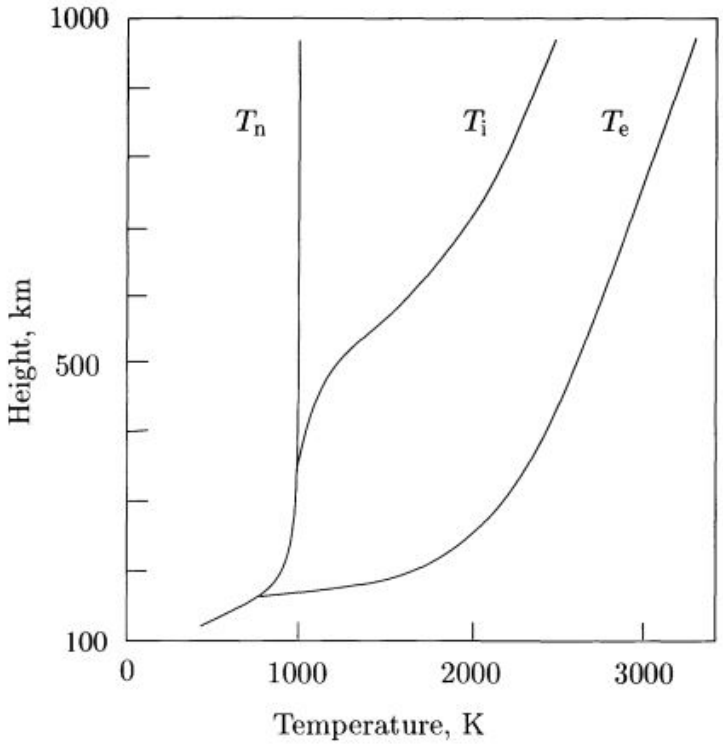

Figure 2.4: Theoretical values for mid-latitude neutral temperature, ion temperature, and electron temperature [2].

[20].

The most common way to characterize scintillation is through the parameter S_4, defined below. In this case, <> denotes averaging and I represents the intensity of the signal which is proportional to the signal amplitude squared.

$$S_4 = \left(\frac{< I^2 > - < I >^2}{< I >^2}\right)$$

Scintillation may be categorized into three groups: strong, moderate, and weak. Strong

scintillation correlates to an S_4 index that is greater than 0.6, moderate scintillation occurs between 0.3 and 0.6, while weak scintillation has an S_4 index that is less than 0.3 [23]. An empirically based generalization between peak to peak fluctuations (P_{fluc}) and the S_4 index is shown below [23]:

$$P_{fluc} = 27.5 S_4^{1.26}.$$

There are three regions that break the Earth into thirds and can be used to further distinguish scintillation: low-latitude (or equatorial), mid-latitude, and high-latitude (otherwise known as polar or auroral). These regions are distinguished by the dip angle of the magnetic field, which is near zero at low latitudes, and greater than or equal to 70^o at high latitudes. The mid-latitude region can be classified as geomagnetic latitudes between 30^o and 60^o.

Scintillation is a frequent occurrence in the equatorial region, starting at sunset and often continuing for many hours [23]. Ionospheric disturbances are also commonplace in the polar regions where geomagnetic storms can have strong effects [23]. High-latitude regions may also experience scintillation during the daytime [24]. Mid-latitude regions are associated with weak scintillation, other than during geomagnetic storms [23], although recent study suggests it may be more active than previously thought [25]. This work focuses on the mid-latitude region because that is where the eclipse occurs and where data will be collected.

2.1.4 Communication Effects

The effects that ionospheric scintillation have on the electromagnetic signals depends on the type of system. Some systems, such as a data relay link, may be able to work around the amplitude and phase fluctuations. A communication system that transmits voice or audio may see a reduction in performance. This is especially important to keep in mind if the system requires a high level of performance, and should be accounted for when designing the system. On the other hand, a synthetic aperture radar (SAR) requires coherent phase and accurate timing information, so scintillation can be a problem if not properly accounted for [3].

Disturbances in the ionosphere cause amplitude variations that dominate other factors (differential phase effects, ranging errors, etc.) at frequencies above 1 GHz [3]. An increase in signal power may seem like a good thing, but it can actually be harmful to the system. Depending on how the receiver is set up, it will most likely receive more than one signal. If that is the case, power monitoring of the received signals is probably in place making a spike in power likely to increase the inter-modulation products of the two signals [3].

Scintillation also has effects on Global Positioning System (GPS) signals. The signal fluctuations can be large enough that it causes the GPS to go through a loss of lock, or failure to track, for up to fifteen seconds at a time during strong fluctuations [26]. This loss of lock can cause large errors, diluted precision, and potential navigation failure [26]. This lead to a large problem as dependency on GPS grows.

2.2 Software Defined Radio

Software defined radio (SDR), otherwise known as software based radio (SBR) or software radio (SR), was first introduced by Mitola [27]. SDR does not have a set definition as there are varying implementations of the technology. Instead, a broad accepted understanding of the concept is applied, where software is implemented on a radio to utilize digitized radio signals [28]. This departs from the traditional idea that the entirety of the transmitter and receiver environment needs to be completed in hardware. Instead, much of the radio is now implemented in software where digital signal processing is done in flexible and reconfigurable functionality blocks [28].

2.2.1 GNU Radio

GNU Radio is an open source software development toolkit designed for signal processing for software defined radios. GNU Radio can be used either with or without hardware, allowing the user to work in a simulation environment or interact with a Universal Software Radio Peripheral (USRP) or other readily available hardware. This software enables the use of blocks that are either preexisting or can be created by a user to implement a SDR. A flowgraph is the term used to define a program in GNU Radio Companion, the GUI for GNU Radio. GNU Radio blocks can transmit, receive, and perform various signal processing implementations. The blocks are Python executable swig-wrapped C/C++ and can be used with a graphical tool known as GNU Radio Companion [29, 30].

Chapter 3

Scintillation Model

There are numerous preexisting models that estimate scintillation for a given time, day, and location. The models of Fremouw and Rino (1973), Aarons (1985), Franke and Liu (1985), Iyer et al. (2006), 3D Ionospheric Plume models [20], and the Wideband Model (WBMOD) [20] were considered as possible tools to predict scintillation during the eclipse. However, these models were not right for this work as they were not valid for the frequency range of interest, the region of interest, not valid for weak scattering, or were not easily altered to account for the rapidly changing temperature and electron densities that may be associated with the eclipse [20].

Instead of using preexisting models, the focus of this work is plasma instabilities. These instabilities are more general, in that all parameters can be modified and are more customizable to the situation at hand. Three instabilities: the Kelvin-Helmholtz instability, gradient drift instability (GDI), and temperature gradient instability (TGI), are thought of as possible

causes for plasma instabilities in the mid-latitude region [25]. Of these, Kelvin-Helmholtz was found to be stable under the eclipse conditions and was therefore discarded [31]. Between TGI and GDI, TGI is expected to be the more dominant of the two instabilities [25, 31, 32] and thus is used here to predict scintillation during the 2017 eclipse.

3.1 Temperature Gradient Instability (TGI)

The temperature gradient instability can be classified as a collisional drift wave instability [33] that is created when the electron density and temperature density gradients in the F region are perpendicular to the magnetic field [34] In the mid-latitude region small density and temperature gradients are continually present, and are related to fluctuations of the electric field in the ionosphere [35]. These gradients may become quite large during the solar eclipse. Under normal conditions TGI produced in the F region can be damped by the conducting E region, causing the instability to occur at night when the E region conductivity is at very low values [36].

There are two different approaches for modeling TGI, stemming from fluid and kinetic theory. Paired with Maxwell's equations, a kinetic equation can be used to describe plasma phenomena, known as kinetic theory [37]. Fluid theory uses a set of fluid equations paired with Maxwell's equations to describe this phenomena if certain conditions are held [37]. Fluid theory is a simplification of kinetic theory and only depends on space and time, while kinetic theory depends on time, space, and velocity [37]. Kinetic theory must be used at

small scales because fluid theory breaks down when the scale size of the instability is smaller than 30 m, as described in Eltrass [25]. This work is intended to include all scale sizes though only the large scale sizes need to be considered for the downlinks of interest.

3.1.1 Parameters

Full kinetic effects for Landau damping, finite gyro-radius ($k_{perp}\rho_{ci} \geq 1$), temperature anisotropy ($v_{t\perp}$,$v_{t||}$), and electron-neutral collisions have been used to solve the TGI kinetic dispersion relation [38]. Similar simplifications have been made in fluid theory, thus the extension of those simplifications into kinetic theory leads to neglecting electron gyro-radius, parallel temperature gradient, and temperature anisotropy shows the growth rate, γ, below [38]. This growth rate simplification is only valid for frequencies below the ion gyro frequency [25]. The growth rate is approximately given by:

$$\gamma \approx \frac{2\nu_e \omega^* \omega_T \Gamma_0(b_i)}{k_{||}^2 v_{te}^2 [\Gamma_0(b_i) - (1+\tau)]^2}$$

where

$$\omega^* = k_\perp (\frac{k_B T_e}{qB_0}) \frac{\kappa_{ne}}{n_0}$$

$$\omega_T = k_\perp (\frac{k_B T_e}{qB_0}) \frac{\kappa_{Te}}{T_e}$$

$$\Gamma_0(b_i) = I_0(b_i) e^{-b_i}$$

Known Constants	
k_B	1.38e−23 J/K
q	1.60e-19 C
m_e	9.11e-31 kg

Assumed Constants	
B_0	4.5e-5 T
m_i	2.66e-26 kg

Table 3.1: Constants used for TGI, both known and assumed.

$$b_i = (k_\perp \rho_i)^2$$

$$\rho_i = \sqrt{\frac{m_i k_b T_i}{q^2 B_0^2}}$$

$$\tau = \frac{T_e}{T_i}$$

In the equations above ν_e is the electron collision frequency, ω^* is the diamagnetic frequency, ω_T is the temperature drift frequency, $k_{||}$ is the perturbed wave number that is parallel to the magnetic field, v_{te} is the electron thermal velocity, κ_{Te} is the electron temperature gradient, κ_{ne} is the electron density gradient, T_e is the electron temperature, T_i is the ion temperature, the ion gryoradius is ρ_i, and $k_\perp$ is perturbed wave number parallel to the magnetic field. It is also worth noting that the product of the diamagnetic frequency and the temperature gradient drift frequency, $\omega^*\omega_T$, are proportional to the growth rate of TGI, γ [25].

Table 3.1 shows all the constants used in the growth rate, both assumed and known.

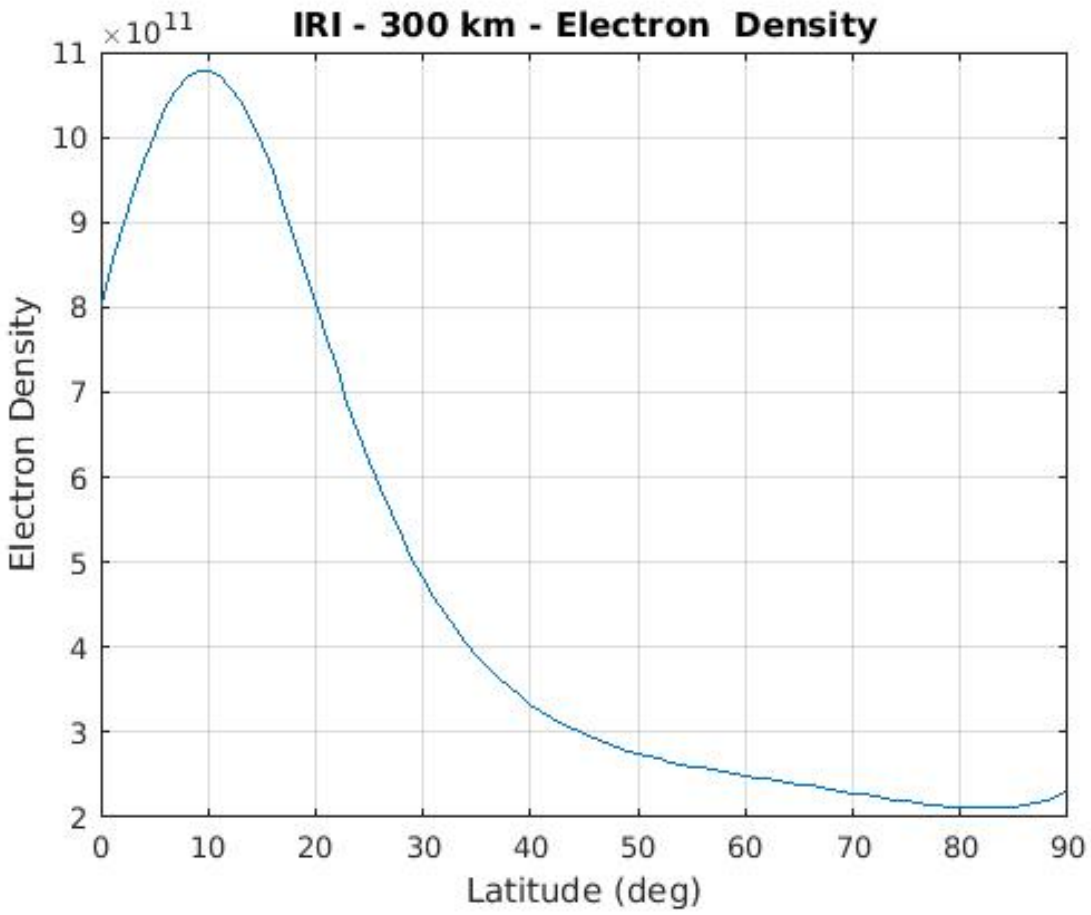

Figure 3.1: Electron density changes by latitude according to IRI model data at 300 km on August 21, 2017 under the conditions specified in Table 3.2.

The known constants are Boltzmann's constant (k_B), the charge on an electron (q), and the mass of an electron (m_e). The magnetic field, B_0, can be estimated as a constant for TGI at $4.5 * 10^{-5}$ T [39]. It can be assumed that the dominating ion for the region of interest is oxygen, as seen in Figure 2.2. Therefore the mass of an ion, m_i, can be modeled as the mass of oxygen.

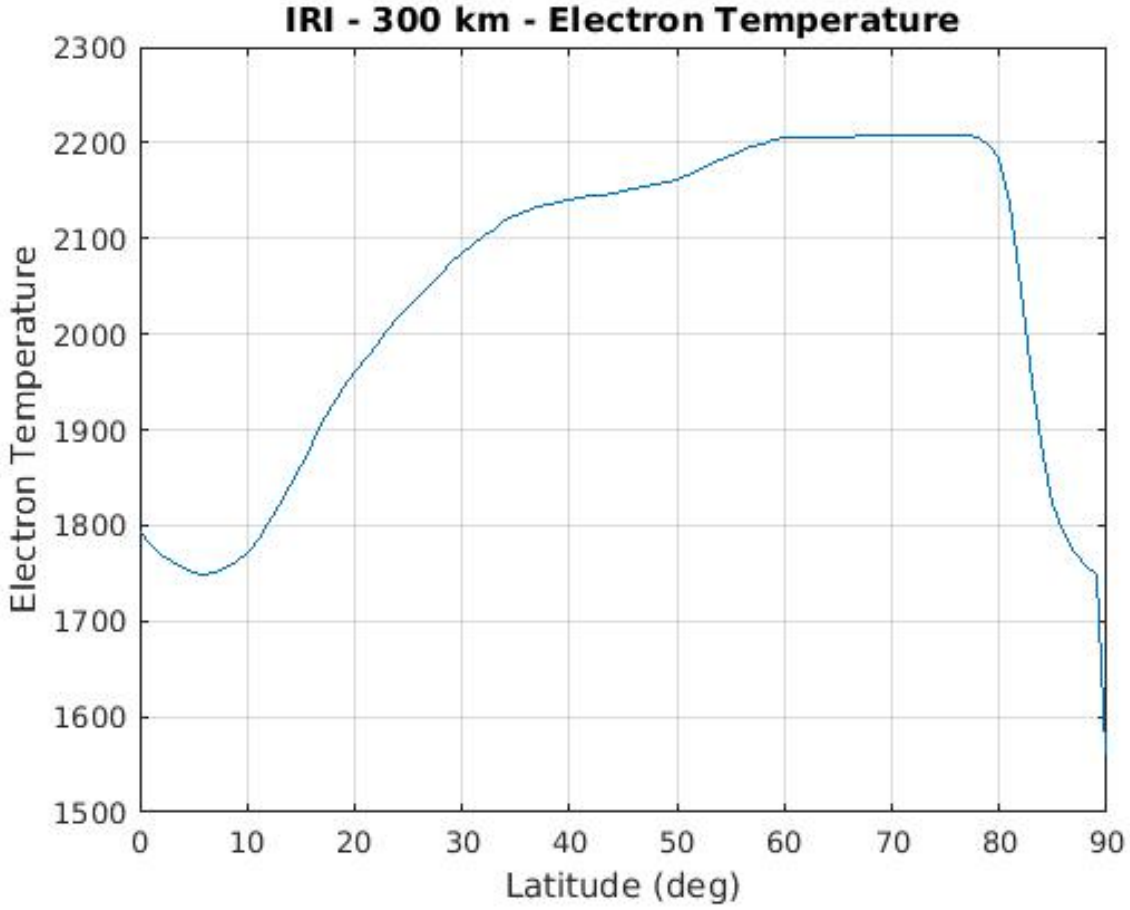

Figure 3.2: Electron temperature changes by latitude according to IRI model data at 300 km on August 21, 2017 under the conditions specified in Table 3.2.

3.1.1.1 IRI Model

The International Reference Ionosphere (IRI) model is used to generate predictions of ionospheric parameters for August 21, 2017. The IRI model is an empirically standard model of the ionosphere that utilizes a worldwide network of ionosondes, incoherent scatter radars, the ISS and Alouette topside sounders, and in situ measurements [40]. The inputs to the model are location, time, date, and height range with options to add solar indexes if desired. Table

Model Inputs	
Year	2017
Month	August
Day	21
Hour of the Day	18.5 UTC
Latitude	39.1141° N
Longitude	265.3725° E
Height Profile	120 - 1,000 km
Stepsize	1 km
Sunspot Number	20.9
F10.7	78.8

Table 3.2: Inputs to the IRI and MSISE model.

3.2 shows the parameters used in the IRI 2016 model to generate expected values for neutral temperature, ion temperature, electron temperature, and electron density.

Kansas City, KS was chosen as the location for the IRI parameters as it is in the middle of the country, therefore the data generated would be a close fit for all sites. Unreliable data were generated below 120 km, so nothing below this value is used. The time of day was chosen to be 18.5 Coordinated Universal Time (UTC) as that is the estimate of when the eclipse will be occurring at the Kansas City site [41]. All values other than those specified in Table 3.2 are left in their defaulted state. The values for sunspot number and F10.7 radio flux were found in [42] for August 2017 monthly predictions. A plot of the different temperatures generated by the IRI 2016 model under these conditions is shown in Figure 3.3 and closely matches the ideal case shown in Figure 2.4. Figures 3.2 and 3.1 show how the electron temperature and density, respectively, change with latitude at 300 km.

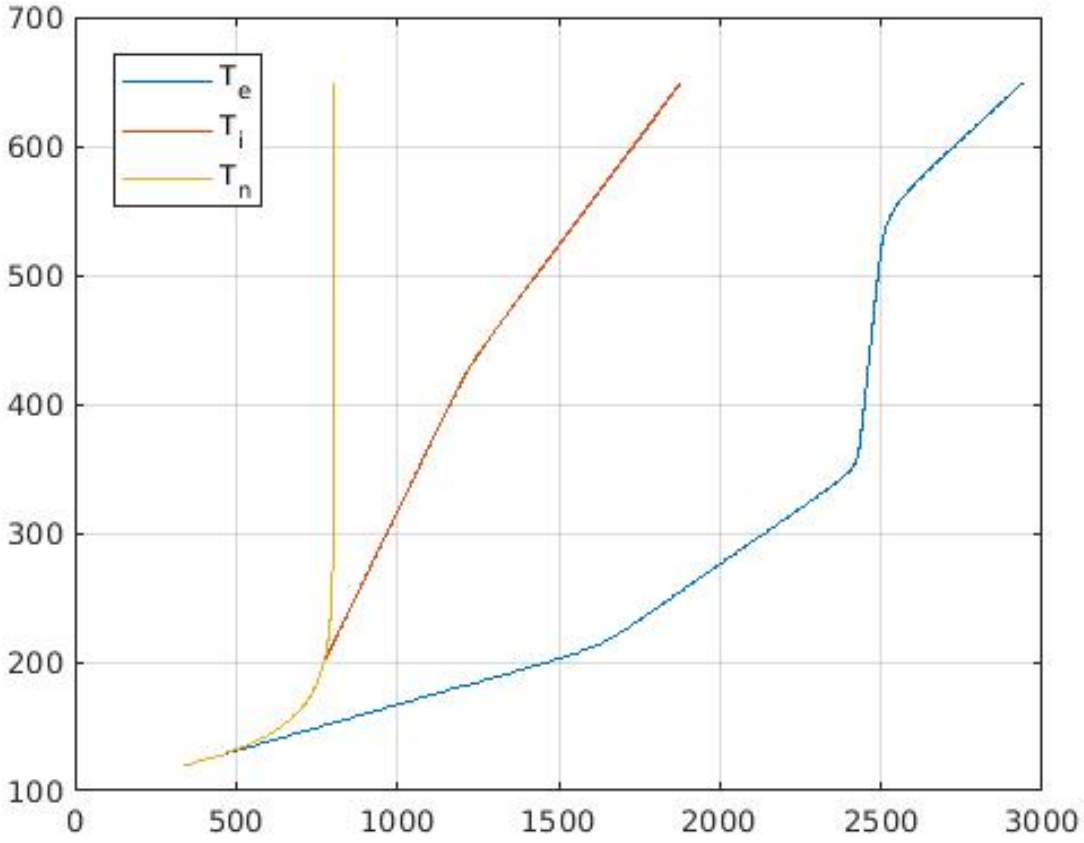

Figure 3.3: Temperature values generated by the IRI Model for August 21, 2017 at 18.5 UTC.

3.1.1.2 MSISE Model

The Mass Spectrometer Incoherent Scatter Radar (NRLMSISE-00) model is an empirical atmospheric model [43] that is used to generate neutral density data for the TGI model. MSISE has similar parameters to IRI, including location, time, date, and height range plus similar options to add solar indexes. To maintain consistency, the same input parameters are used in the MSISE model as in the IRI model data shown in Table 3.2, with two caveats.

First, MSISE-00 is not able to generate data above 1,000 km, therefore this was used as an upper limit. Another limitation of MSISE-00 is that it cannot give information for August 2017, so the year 2016 was used instead. The densities in the MSISE-00 model return a value in number of particles per cubic centimeter, while the TGI model requires units of m^{-3}. To remedy this, the densities were multiplied by 1e6 to convert the values into cubic meters.

MSISE gives the individual neutral densities by molecule, therefore these are added together to generate values for the TGI model. Although O^+ will be the dominant neutral molecule at the altitudes of interest, all other densities are included for thoroughness. Figure 3.4 depicts the individual and total neutral densities and electron density over a range of heights, and is similar to the theoretical densities shown in Figure 2.2.

3.1.1.3 Other Parameters

The two input variables of the kinetic TGI model are the scale size associated with the instability and the height of the instability. The instability is most likely to be operative in the high density F region [35], therefore this work focuses on altitudes from 120 650 km. Scale size denotes the size of an irregularity and in terms of scintillation, is most effective when it is equal in dimension to the first Fresnel zone [3], as denoted below.

$$d = \sqrt{\frac{\lambda d_T d_R}{d_T + d_R}}$$

Here d is the Fresnel zone radius, λ is the wavelength of the transmitted signal, d_T is the

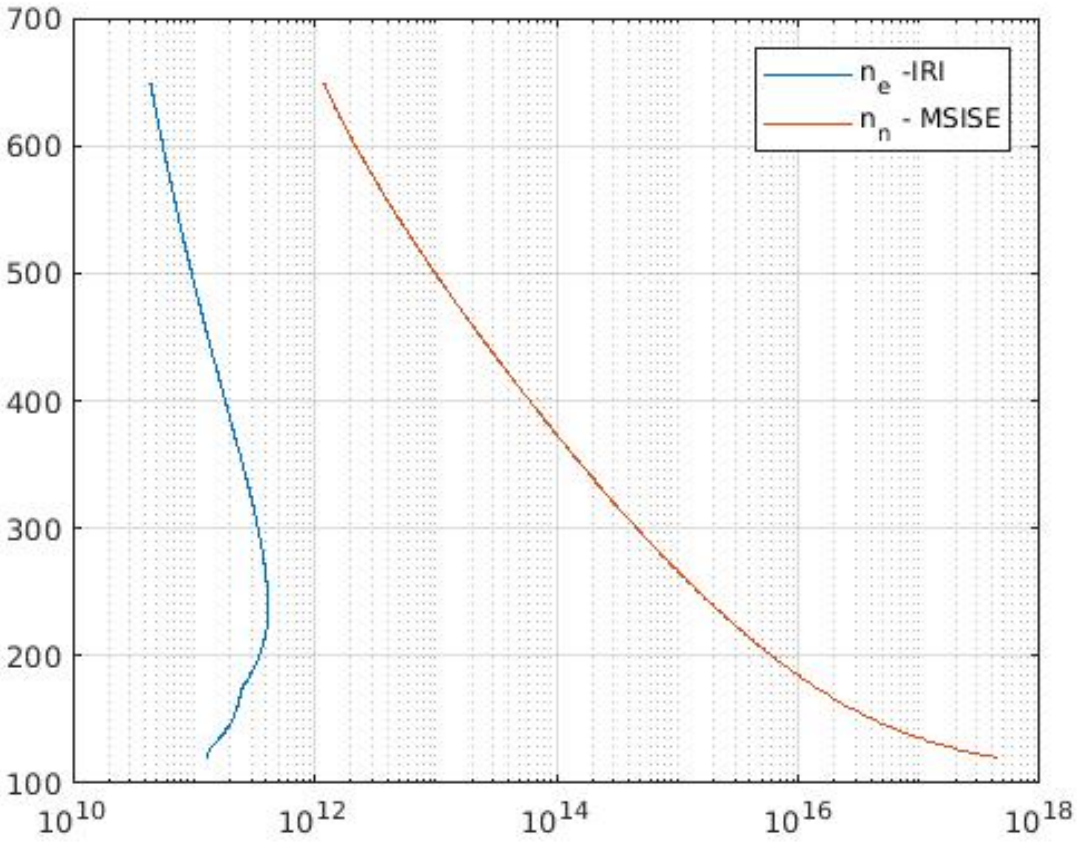

Figure 3.4: Density values generated by the IRI Model and MSISE Model for August 21, 2017 at 18.5 UTC.

distance from the transmitter to the Fresnel zone, and d_R is the distance from the receiver to the Fresnel zone. Scale sizes associated with scintillation can range from centimeters all the way up to hundreds of kilometers [44] Table 3.3 shows the scale sizes associated with scintillation for each of the transmitters over a variety of altitudes. The scale size is a function of the frequency of the transmitted signal as well as the height at which the instability occurs.

	Scale Sizes (m)						
Active Height	NOAA 15	NOAA 18	NOAA 19	SARSAT 7	SARSAT 10	SARSAT 12	Inmarsat
200 km	572.7	577.2	580.5	170.9	172.5	173.0	196.7
250 km	613.3	620.2	624.4	183.1	185.3	186.0	219.8
300 km	641.0	650.6	655.8	191.3	194.4	195.4	240.6
350 km	657.3	670.3	676.6	196.2	200.3	201.6	259.7
400 km	663.1	680.1	687.6	198.0	203.2	204.9	277.4
450 km	658.8	680.5	689.5	196.6	203.3	205.4	294.0
500 km	643.9	671.5	682.1	192.2	200.6	203.2	309.7
550 km	617.9	652.6	665.3	184.4	195.0	198.2	324.6
600 km	579.2	623.0	638.3	172.9	186.2	190.2	338.8
650 km	525.0	581.2	599.7	156.7	173.7	178.7	352.4

Table 3.3: Scale size needed to produce scintillation for NOAA, SARSAT, and Inmarsat downlinks with various active height regions.

As Table 3.3 shows, scale sizes of a few hundred meters have to be present in order to see scintillation in the received signal at the frequencies of the receivers. The TGI model varies scale size from 15 m to 5 km to cover a variety of scale sizes, as it is better to simulate more scale sizes than necessary for comparison purposes.

When discussing TGI, the wavenumber k is not the wavenumber of the transmitted signal but rather the wavenumber of the instability. This wavenumber is found by taking $2\pi/\lambda_{inst}$ where λ_{inst} is the scale size of the instability.

To find the parallel $k_{||}$ and perpendicular $k_{\perp}$ components of the wavenumber k to the magnetic field, it was assumed that the parallel component of the wavenumber was constant over the calculated range of scale sizes. The underlying assumption is that the height difference corresponding to one e-fold value of electron density is an approximation for the wavenumber component parallel to the magnetic field. This e-folding value was found at 289

km, as it is a constant part of the neutral density graph. This leads to a change in height of 160 m, or a parallel wavenumber of $0.04m^{-1}$.

Finding $k_\perp$ was a matter of using Pythagorean theorem with k and k, as shown below.

$$k_\perp = \sqrt{k^2 - k_{||}^2}$$

The other parameters in TGI that has not already been discussed is the total collision frequency. The total collision frequency is the sum of the electron neutral collision frequency and the electron ion collision frequency, as shown below [45]:

$$\nu_e = \nu_{en} + \nu_{ei}$$

where

$$\nu_{en} = 5.4 * 10^{-10} n_n T_e^{1/2}$$

$$\nu_{ei} = [34 + 4.18 ln(\frac{T_e^3}{n_e})] n_e T_e^{-3/2}.$$

In this equation, T_e is the electron temperature measured in Kelvin and each of the densities, neutral and electron, is measured in cm^{-3}. The MSISE-00 corrected densities are in cubic meters and must be converted back to cubic centimeters by multiplying it by $1e-6$. Figure 3.5 shows each collision frequency (ion, electron, and total), calculated using theoretical values from Kelley [45].

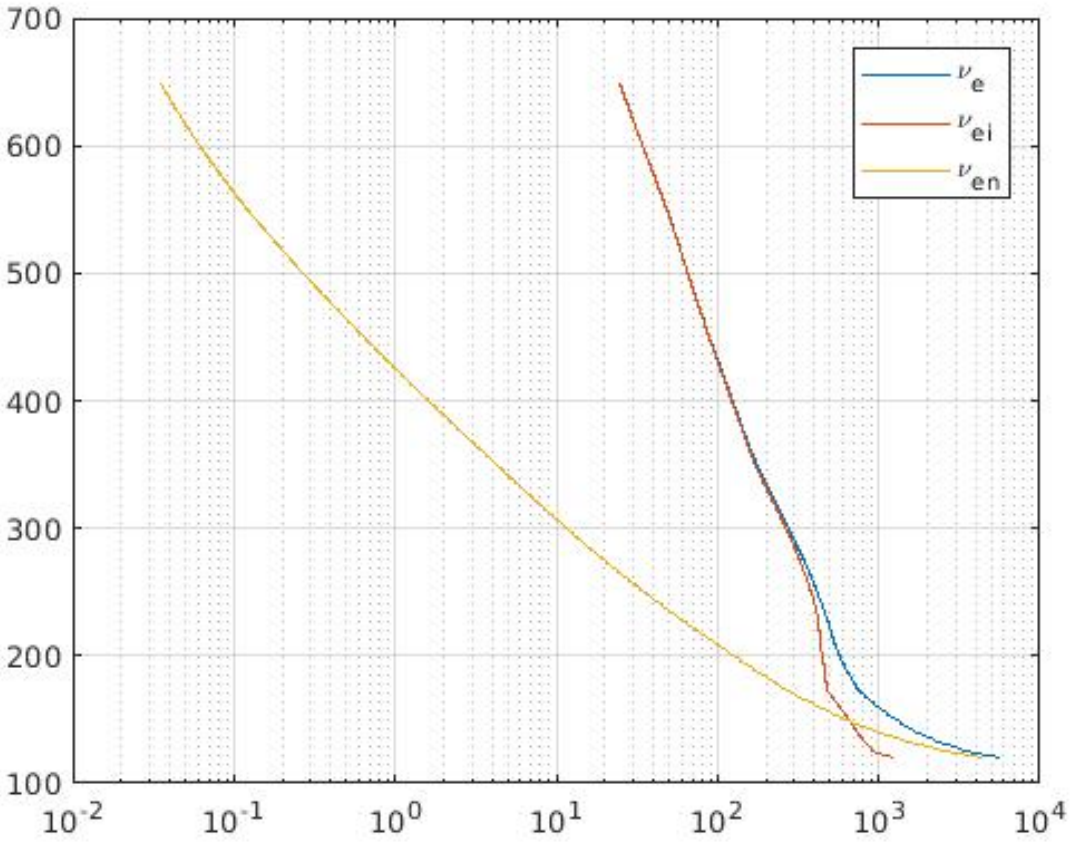

Figure 3.5: Collision frequency values generated for August 21, 2017 at 18.5 UTC under normal mid-latitude conditions.

3.1.2 Normal Conditions

The radius of the penumbra of the eclipse is approximately 50 km, as shown in Figure 4.2. To ensure that the TGI model for normal conditions can be properly compared with the TGI model for the eclipse, this same distance measurement must be used. In order to estimate irregularity growth rates, the electron temperature gradient, κ_{te}, and electron density gradient, κ_{ne}, need to be quantified.

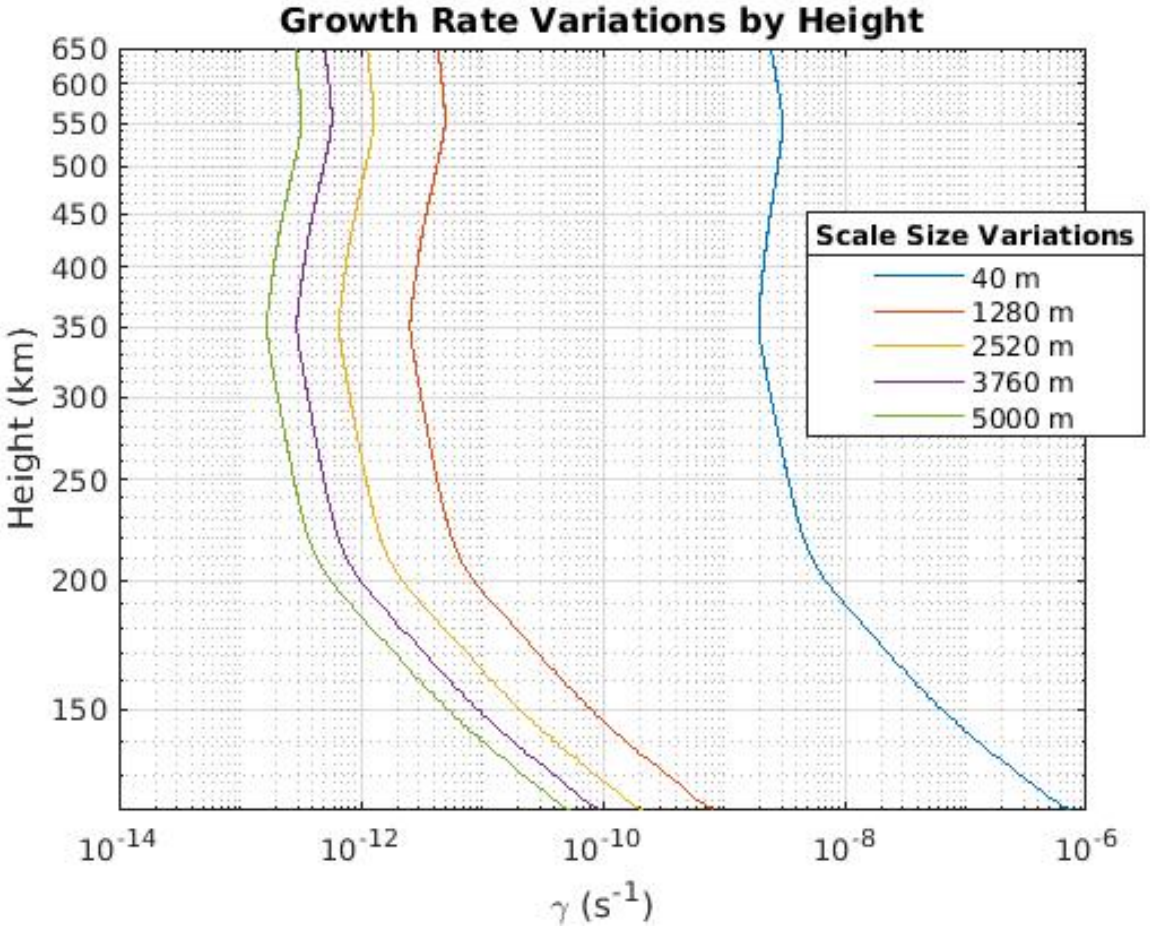

Figure 3.6: Temperature gradient instability growth rate by height with variations in scale size under normal conditions.

Modeling normal conditions can be estimated using the IRI and MSISE models to find κ_{te} and κ_{ne} under normal mid-day conditions, over a 50 km range, north of Kansas City. At this point, the IRI model was re-run using the same conditions as before. The electron temperature and electron density of the two points are then subtracted and divided by the 50 km that separates them. In turn, this derivative is normalized by either the electron temperature or electron density, whichever is applicable. The equations for these two gradients are below:

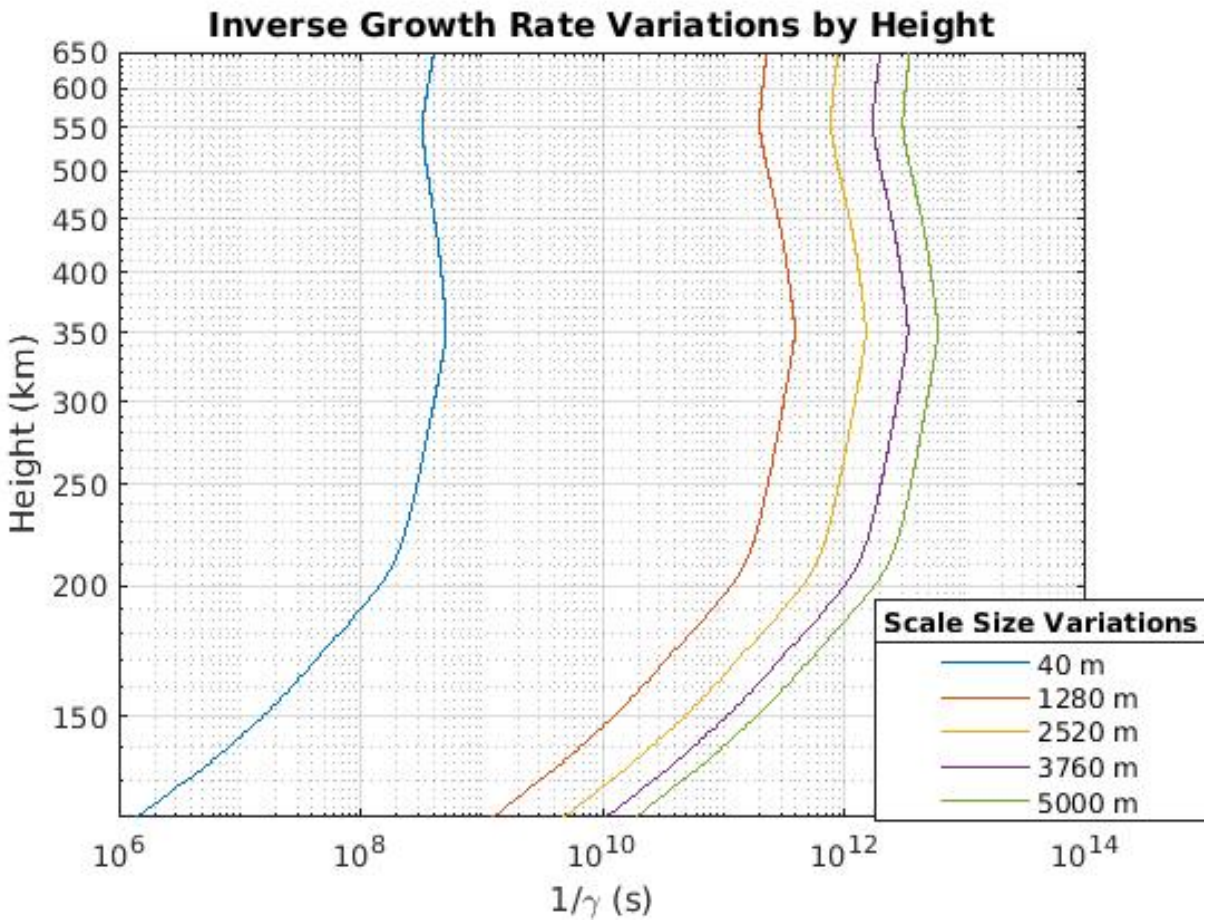

Figure 3.7: Inverse temperature gradient instability growth rate by height with variations in scale size under normal conditions.

$$\kappa_{ne} = \frac{dn_e}{dx}\frac{1}{n_e} = \frac{\Delta n_e}{\Delta x}\frac{1}{n_e}$$

$$\kappa_{te} = \frac{dT_e}{dx}\frac{1}{T_e} = \frac{\Delta T_e}{\Delta x}\frac{1}{T_e}$$

The parameters, including those described above, are used in a MATLAB script to find the growth rate dependencies on height and scale size. The parameter outputs are shown in Table 3.4, which assumes a height of 300 km and 450 km. Figure 3.6 shows how the growth

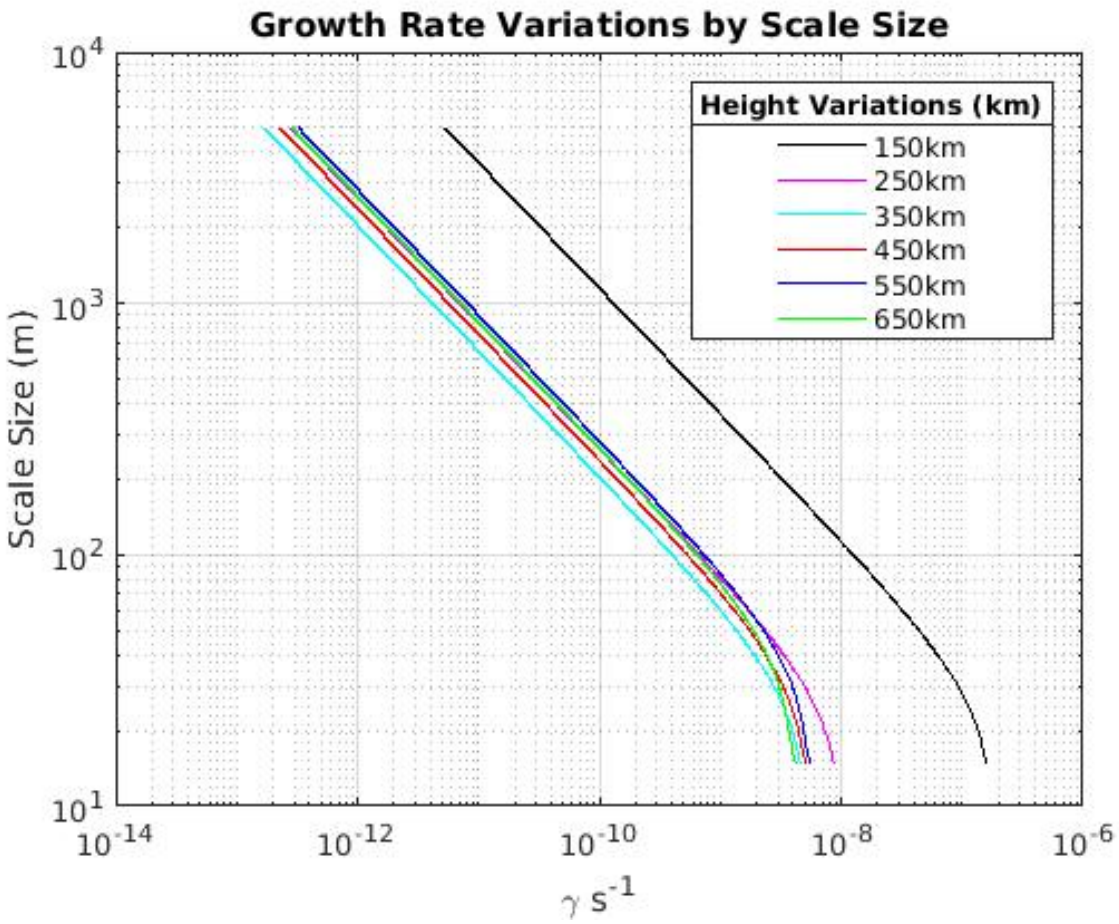

Figure 3.8: Temperature gradient instability growth rate by scale size with variations in height under normal conditions.

rate, γ, changes with height for various scale sizes. In turn, Figure 3.7 shows the inverse growth rate, or how long it takes for the given instability to develop. While the model may not be accurate for shorter scale sizes, it does appear to be accurate for larger scale size variations over all heights. The figure shows that the growth rate for the TGI is largest at altitudes below 200 km, and also that smaller scale irregularities will grow considerably faster than larger scales. Comparison with Figure 2.2 shows that these large growth rates occur at and below the bottom-side F region density "ledge", where the plasma density has

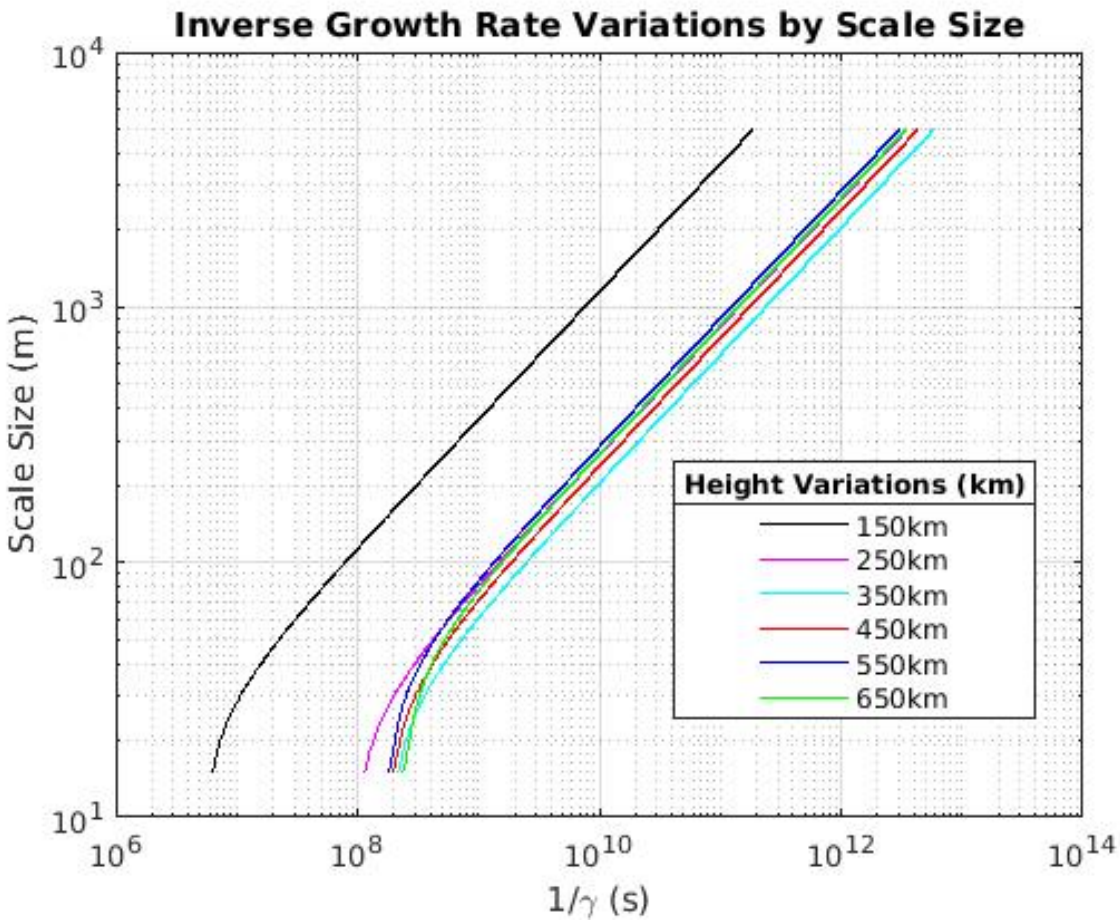

Figure 3.9: Inverse temperature gradient instability growth rate by scale size with variations in height under normal conditions.

a strong gradient versus height.

Though these values are smaller than those found in [25], there are differences in the fundamental makeup of the two. The results in [25] are found for nighttime conditions, whereas this model is near noontime during the day, which decreases the growth rates because of the normalization of κ_{te} and κ_{ne}. In other words, T_e and n_e are both large in the daytime, so the κ_{te} and κ_{ne} terms are smaller.

Output Parameters Under Normal Conditions		
Parameter	300 km	450 km
T_e, K	2139.2	2469
T_i, K	968	1282.9
τ	2.21	1.92
n_o, m^{-3}	3.41 x 10^{11}	1.32 x 10^{11}
n_n, m^{-3}	4.64 x 10^{14}	2.39 x 10^{13}
ω_t, rad/s	6.35 x 10^{-7}	6.35 x 10^{-7}
ω^*, rad/s	3.59 x 10^{-6}	1.08 x 10^{-5}
ρ_i, m	2.62	3.01
b_i	2.71 x 10^{-4}	3.59 x 10^{-4}
κ_{ne}, km^{-1}	1.40 x 10^{-7}	3.62 x 10^{-7}
κ_{te}, km^{-1}	2.46 x 10^{-8}	2.13 x 10^{-8}
Γ_o	0.9997	0.9996
ν_{ei}, Hz	265.32	88.68
ν_{en}, Hz	11.59	0.64
ν_e, Hz	276.91	89.32
v_{te}, m/s	1.80 x 10^5	1.93 x 10^5
γ, s$^-$1	5.17 x 10^{-12}	5.71 x 10^{-12}
$\frac{1}{\gamma}$, s	1.93 x 10^{11}	1.75 x 10^{11}

Table 3.4: Output parameters for TGI Model under normal conditions for 300 km and 450 km.

Figure 3.8 shows the growth rate of TGI as a function of scale size for specific heights, while Figure 3.9. Looking more in depth at the figure, it shows that for all of the F region heights the general shape is the same. However, it can be seen that the shapes are not exact copies of each other and there is dependency on height for scale size measurements. Smaller scales are again seen to have the largest growth rates at all altitudes, and the growth rates are largest at altitudes below 250 km.

Both figures agree that the lower altitude regions, below 200 km, have the largest growth

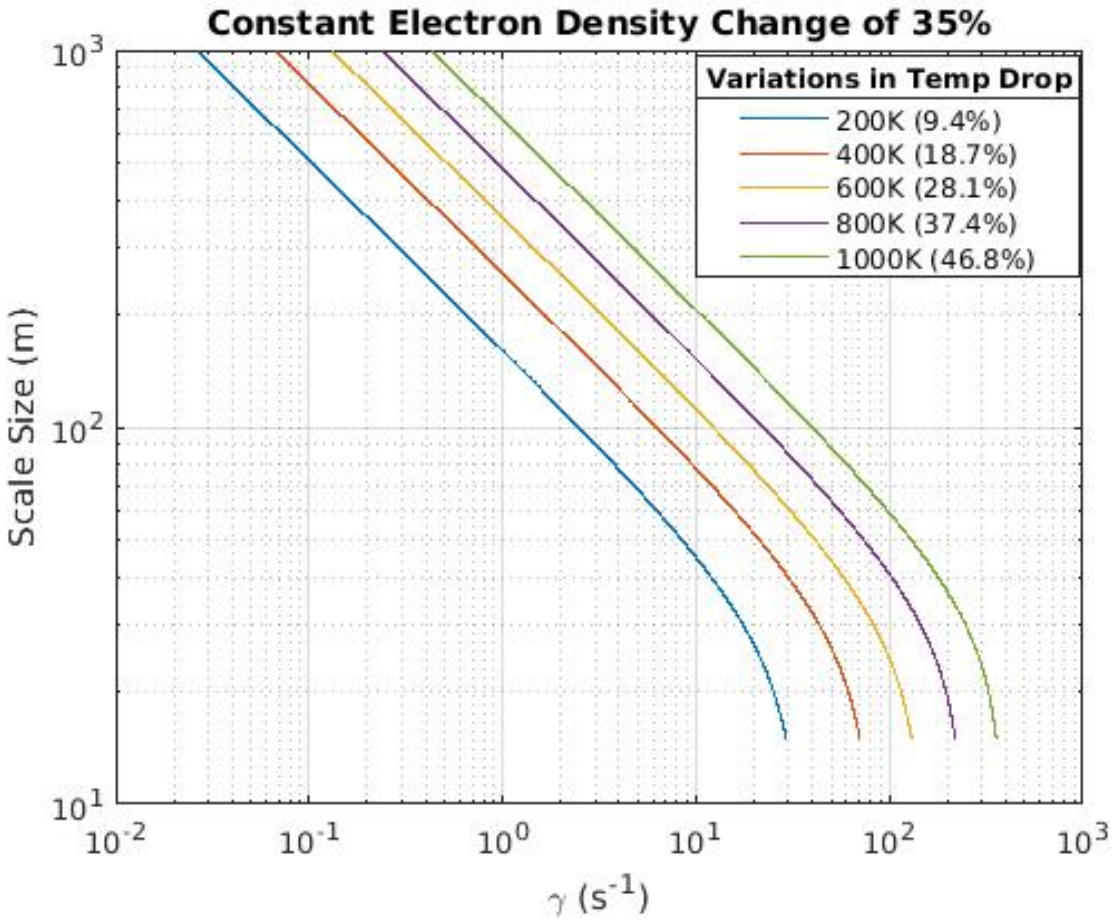

Figure 3.10: Temperature gradient instability growth rate by scale size with variations in electron temperature drop, assuming an electron density decrease of 35 percent.

rate. However, this region range is generally considered to be in the E region while the focus of this work is the F region. Comparison to Figure 2.2 shows that the altitudes of maximum instability growth occur in the range where the molecular ions (NO^+ and O_2^+) become larger than the O^+ density. This important point will be revisited in the next section, where eclipse conditions are considered.

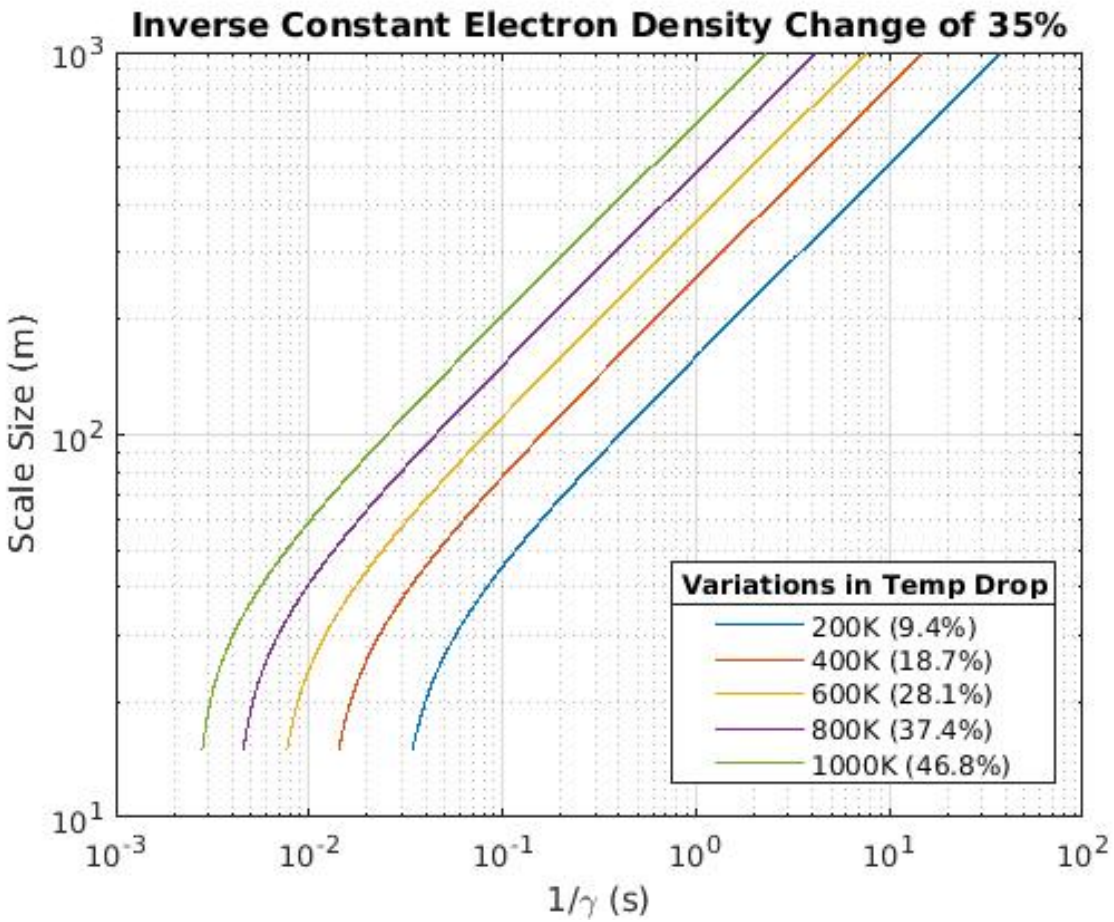

Figure 3.11: Inverse temperature gradient instability growth rate by scale size with variations in electron temperature drop, assuming an electron density decrease of 35 percent.

3.1.3 Eclipse Conditions

A prediction of an electron temperature drop, up to 800 K, [46] and an electron density drop of 0.35 have been estimated based on previous observations [41,47], so these values are used here to examine the TGI model under eclipse conditions. This drop in electron temperature and density is referring to the differences associated with the center of the penumbra versus outside of the umbra, so it is implicitly assumed that conditions in the penumbra do not

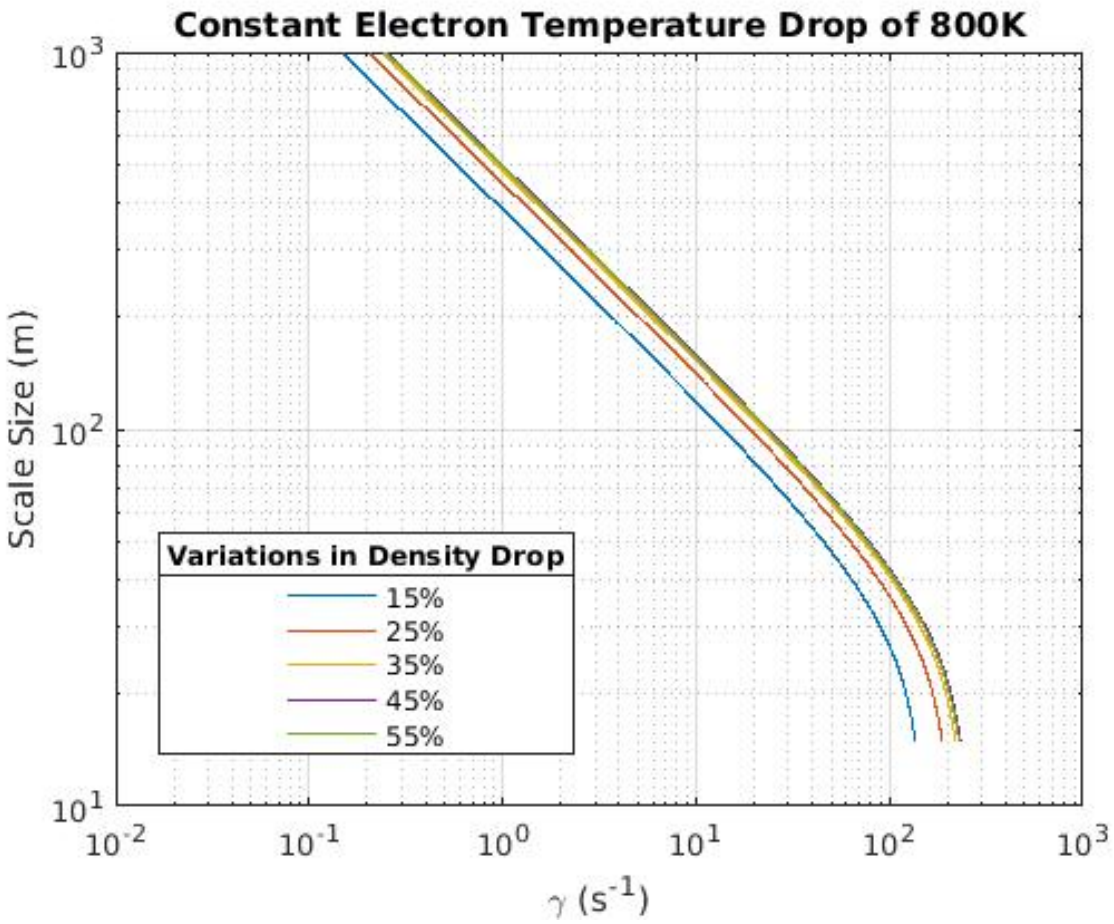

Figure 3.12: Temperature gradient instability growth rate by scale size with variations in electron density drop, assuming an electron temperature decrease of 800 K.

vary much from the normal background. Table 3.5 compares parameters generated by the normal TGI model to those in the eclipse TGI model at 300 km when a temperature drop of 800 K was applied and a drop in density gradient of 35 percent.

The values mentioned above were used to generate a MATLAB function for a three point spline fit for the electron temperature gradient and the electron density gradient, based off of work by Magda Moses [41]. For the electron temperature spline fit, inputs included IRI

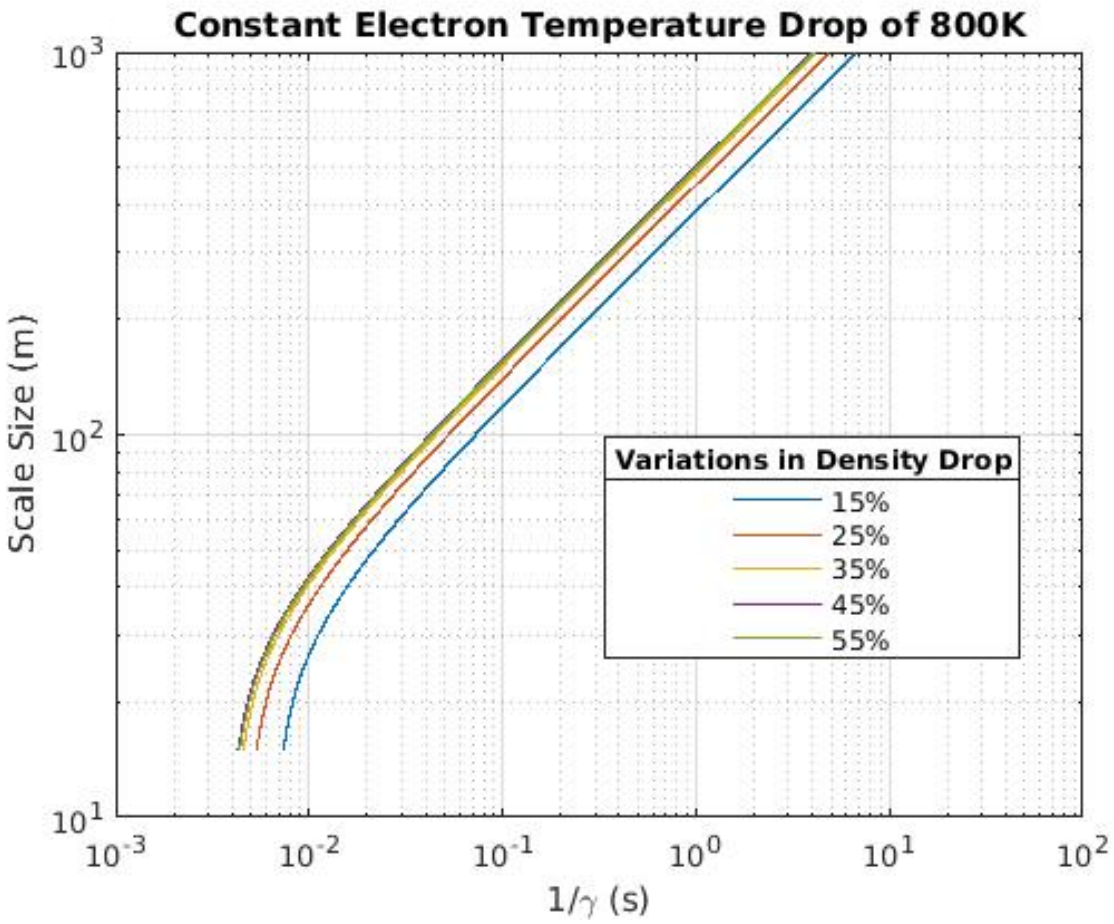

Figure 3.13: Inverse temperature gradient instability growth rate by scale size with variations in electron density drop, assuming an electron temperature decrease of 800 K.

electron temperature data as well as the specified drop in temperature [46]. From this spline, the maximum derivative was found and returned from the function. A similar approach was used for the electron density gradient, with inputs being the IRI electron density and the percentage drop in the density corresponding to the center of the eclipse.

A range of five different electron temperature drops and another five different electron density drops were assumed to see estimate the role of these changes on the TGI growth rate.

Output Parameters at 300 km		
Parameter	Normal	Eclipse
T_e, K	2139.2	1339.2
T_i, K	968	968
τ	2.21	1.38
n_o, m^{-3}	3.41 x 10^{11}	1.19 x 10^{11}
n_n, m^{-3}	4.64 x 10^{14}	4.64 x 10^{14}
ω_t, rad/s	6.35 x 10^{-7}	1.45 x 10^{-1}
ω^*, rad/s	3.59 x 10^{-6}	0.25
ρ_i, m	2.62	2.62
b_i	2.71 x 10^{-4}	2.71 x 10^{-4}
κ_{ne}, km^{-1}	1.40 x 10^{-7}	1.57 x 10^{-2}
κ_{te}, km^{-1}	2.46 x 10^{-8}	9.00 x 10^{-3}
Γ_o	0.9997	0.9997
ν_{ei}, Hz	265.32	183.86
ν_{en}, Hz	11.59	9.17
ν_e, Hz	276.91	193.03
v_{te}, m/s	1.80 x 10^5	1.42 x 10^5
γ, s^1	5.17 x 10^{-12}	0.237
$\frac{1}{\gamma}$, s	1.93 x 10^{11}	4.22

Table 3.5: Output parameters for TGI Model under normal conditions compared with those generated by eclipse conditions at 300 km. The eclipse conditions applied were a drop in temperature of 800 K and a drop in density of 35 percent.

The temperature drops were 200 (9.35%), 400 (18.7%), 600 (28.1%), 800 (37.4%), and 1000 (46.8%) K while the density drops were 15%, 25%, 35%, 45%, and 55%. A range of values above and below the predicted values were used in an effort to show the trends over ranges encompassing those predicted. These values are all plotted at a height of 300 km in Figures 3.10, 3.12, 3.14, and 3.15.

All of these parameters were then inputted into a MATLAB script that generated the

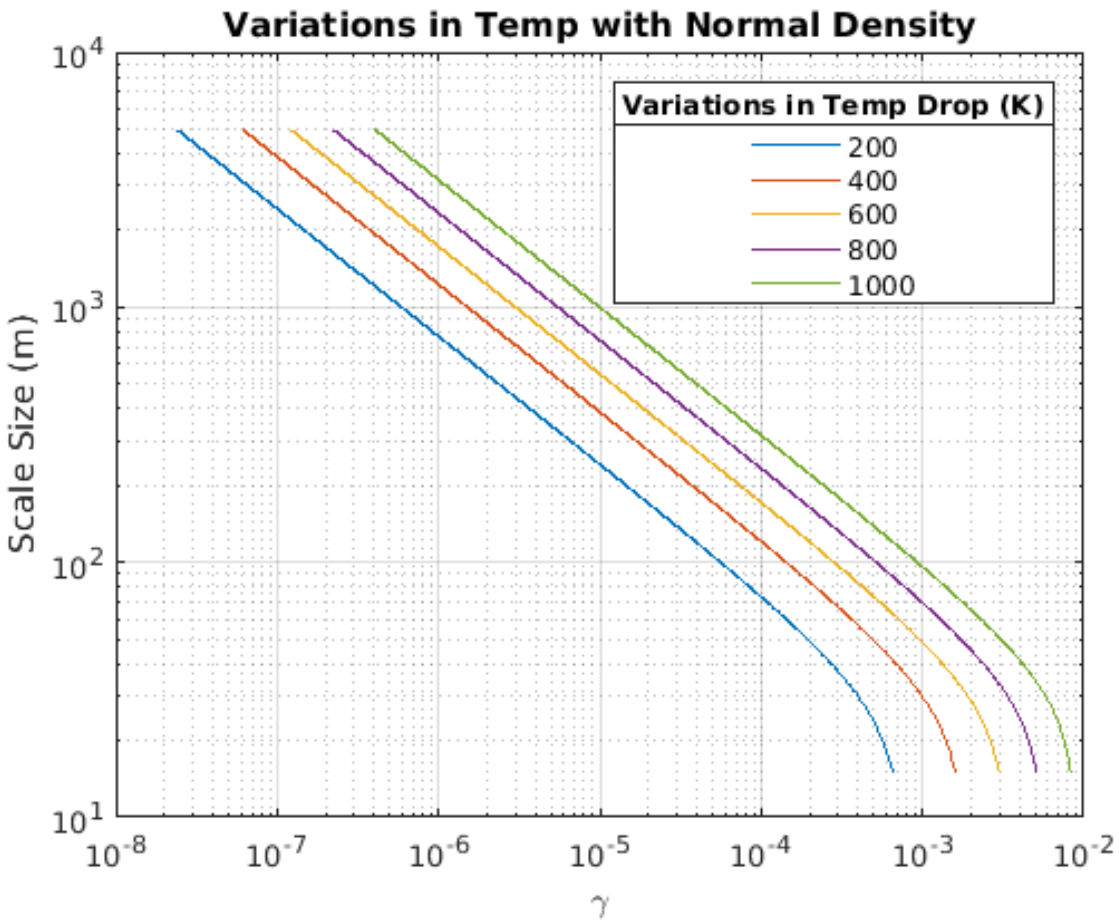

Figure 3.14: Temperature gradient instability growth rate by scale size with variations in electron temperature decrease with only electron temperature experiencing eclipse conditions of 800 K.

TGI model for eclipse conditions. By comparing Figure 3.10 and Figure 3.12, it is easy to see that the change in temperature plays a larger role than changing the electron density. Figures 3.11 and 3.13 show the inverse growth rate, or how long it will take the instability to grow one e-fold and develop. However, these figures show both a change in the electron density and in the electron temperature. If only one were to occur, it would look more like Figure 3.14 and Figure 3.15. While only the plots for a electron temperature drop of 800

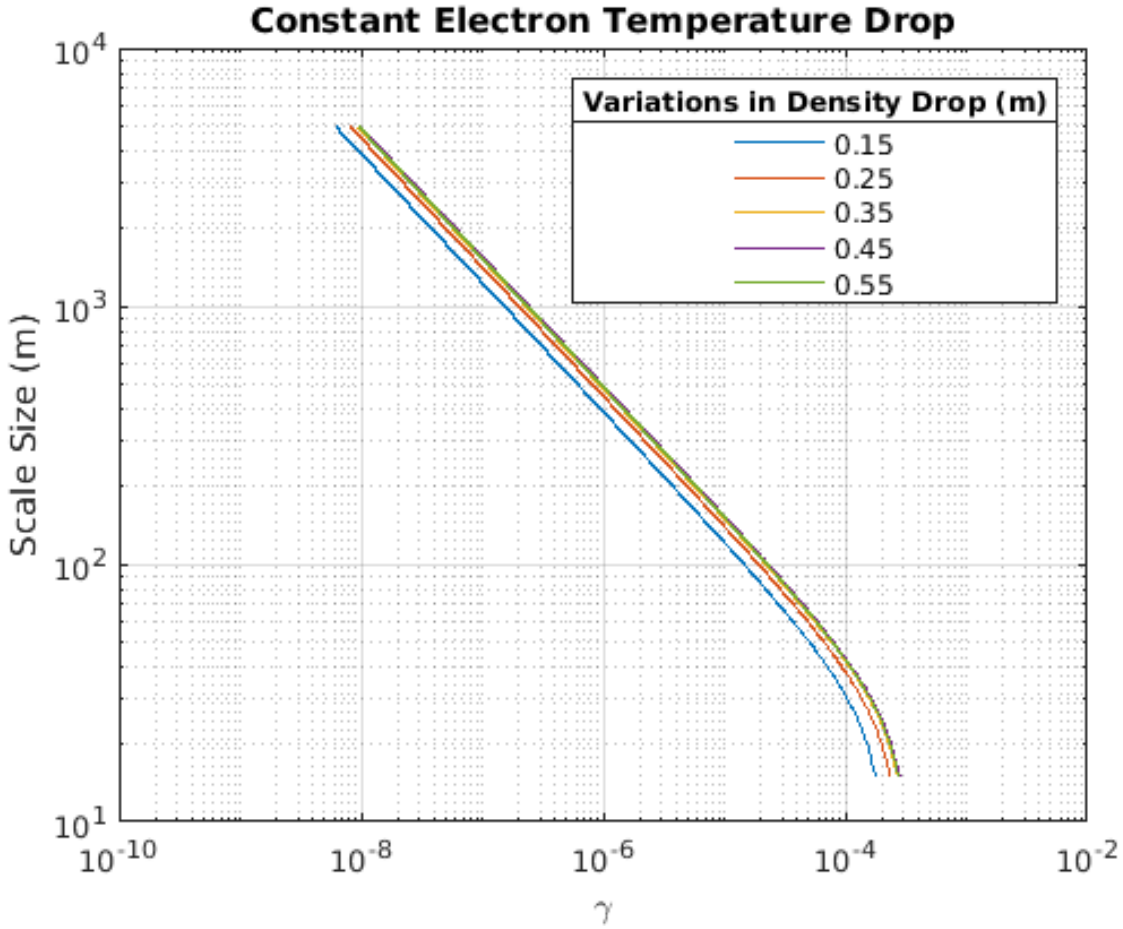

Figure 3.15: Temperature gradient instability growth rate by scale size with variations in electron temperature drop with only electron density experiencing eclipse conditions of 35 percent.

K and electron density drop of 35 percent are included here, the rest of the values can be found in Appendix A.1.

3.2 Discussion

According to the TGI model under normal conditions, ionospheric scintillation would not be present on August 21, 2017 because the growth rates shown in Figures 3.6 and 3.8 are very small. However, if the eclipse were to affect both the electron temperature and the electron density, there is a possibility of seeing scintillation for small scale sizes. The scale sizes that are needed to see scintillation on Inmarsat and SARSAT are on the order of 10 s, while NOAA has a scale size growth rate on the order of 10^{-1} s.

One of the assumptions that was made for TGI was a constant $k_{||}$. While overall not a bad assumption, it did cause the growth rate to exponentially increase when $b_i \approx 1$. For this reason, information above $b_i \approx 1$ is not considered. The satellites being considered have longer scale sizes (and correspondingly small k values), meaning that not considering data that is larger than $b_i \approx 1$ is acceptable.

Ion and electron production rates are slower than recombination rates [3] therefore faster changes are expected at the onset of the eclipse compared to the ending of the eclipse. Taking it one step further, if scintillation were to occur it is more likely to occur at the beginning half of the eclipse compared with the ending of the eclipse. Though this prediction is only valid for an altitude between 200 km and 650 km do to the difference in molecular ions outside of this range.

Figures 3.11 and 3.13 depict how long the TGI will take to develop one e-fold. Looking at this graph and comparing it to the length of totality, it can be seen that under these

conditions scintillation is likely to be present in the scale sizes of interest. However, this assumes that all the assumptions and simplifications made thus far and valid. One such assumption is the direction of the electron density and electron temperature gradients. In the simplification found in Eltrass [25], the gradients were in opposing directions.

From this, it needs to be determined if the sign of the gradients matter. In this work, the magnitude of the values were used since the gradients are in the same direction. When using the non-simplified version of kinetic theory, at least in those used to generate the simplification, the gradients were in opposing directions [48].

To determine if the sign of the gradient altered the results, instances of the full non-simplified kinetic theory [25] were generated for both opposing and similar direction gradients with no difference in output. However, when the electron temperature gradient was increased significantly and the sign changed imposed, the outputs did vary from each other. This could mean that the results presented here are an idealistic case and may not be valid if the electron temperature and density gradients are in the same direction, as expected during the solar eclipse.

Chapter 4

Measurement Setup

In order to get reliable scintillation measurements, the satellites utilized for measurements must be observable by the receivers during the time of interest. This time of interest begins a couple hours before the eclipse starts, lasts through the eclipse, and culminates a few hours after the eclipse. The physical locations of the receivers are spread throughout the United States to provide a variety of measurements. As discussed in Chapter 2 ionospheric scintillation may vary at different geographic locations, leading to the need to have receiver locations throughout the United States. The scintillation receivers must be built, coded, and tested to verify that their measurements are accurate. The following sections discuss these considerations in detail.

4.1 Satellites Used

Since planning began months prior to the eclipse and atmospheric drag is not predictable with sufficient accuracy, it was difficult to determine which satellites will be visible during the event due to their constantly changing orbital elements. Low Earth Orbiting (LEO) satellites were initially thought of as possible solution due to their short period of rotation around the Earth. This short period ensures that the LEO satellite transmission will be able to be received somewhere in the United States every couple of hours. If a network of LEO satellites were to be considered, for example three or more satellites instead of one, there would be it is likely that at least one LEO satellite in the constellation would be observable during a portion of the time interval of interest.

Geostationary (GEO) satellites are also considered as they provide an unchanging geometry in a constant frame of reference. This frame of reference is advantageous when a LEO satellite is not overhead, since it allows continuous measurements to be taken throughout the eclipse. Since there will be multiple receiver locations stationed across the United States, the GEO satellite should be observable at all locations. All satellites that were considered, whether LEO or GEO, need to have a constant downlink to provide continuous scintillation measurements. Scintillation is a relatively fast-occurring phenomenon, so bursty transmissions are not suited to scintillation measurements.

Due to these restrictions, the National Oceanic and Atmospheric Administration (NOAA) Polar Operational Environmental Satellites (POES) were chosen for the LEO satellites, while

Low Earth Orbit Satellites		
Host Satellite	Transmitter	Frequency
NOAA 15	NOAA 15	137.62 MHz
NOAA 15	SARSAT 7	1544.5 MHz
NOAA 18	NOAA 18	137.9125 MHz
NOAA 18	SARSAT 10	1544.5 MHz
NOAA 19	NOAA 19	137.1 MHz
NOAA 19	SARSAT 12	1544.5 MHz

Geostationary Satellite	
Transmitter	Frequency
Inmarsat 4F-3	1525-1559 MHz

Table 4.1: LEO and GEO Relevant Satellite Parameters

the Inmarsat 4-F3 was chosen for the GEO satellite. Both LEO and GEO satellites are used in order to have multiple points of measurement. Table 4.1 shows that Inmarsat utilizes a higher frequency than the NOAA POES, which is why all three are used. One of the benefits of using the NOAA POES is that there is a NOAA Search and Rescue Satellite Aided Tracking (SARSAT) transceiver on board, enabling two different scintillation measurements to be taken from the same satellite, as both downlinks will be recorded by the receivers. Since scintillation is frequency dependent, this allows for more complete study of scintillation effects. Table 4.1 shows the frequencies associated with each downlink that is used to take scintillation measurements.

4.1.1 NOAA POES

NOAA POES have many uses, but is primarily used for environmental and weather research. The NOAA POES satellites have an Automatic Picture Transmission(APT) transmitter that provides a constant downlink and making it available for continuous scintillation measurements. If decoded, these pictures give a live view of what the NOAA satellite is seeing while passing overhead. The frequencies at which the pictures are transmitted change slightly with each satellite, with each having a downlink specified in Table 4.1. NOAA 15, 18 and 19 are the only NOAA POES currently in orbit, therefore they are the only ones being used for this study.

4.1.2 SARSAT

SARSAT is an international search and rescue initiative that detects distress beacons at 406 MHz from all over the globe at every hour of the day. The information associated with this emergency beacon is then transmitted on one of SARSAT's downlink signals. SARSAT has a dedicated downlink of 1544.5 MHz that is used for every SARSAT in orbit as seen in Table 4.1. It should be stressed that the SARSAT transmitters used to take scintillation measurements are on-board the NOAA satellites as there are also dedicated SARSAT satellites that are not being used in this work. SARSAT 7 is on-board NOAA 15, SARSAT 10 is on-board NOAA 18, and SARSAT 12 is on NOAA 19. Scintillation measurement will be taken simultaneously for the NOAA and SARSAT satellites.

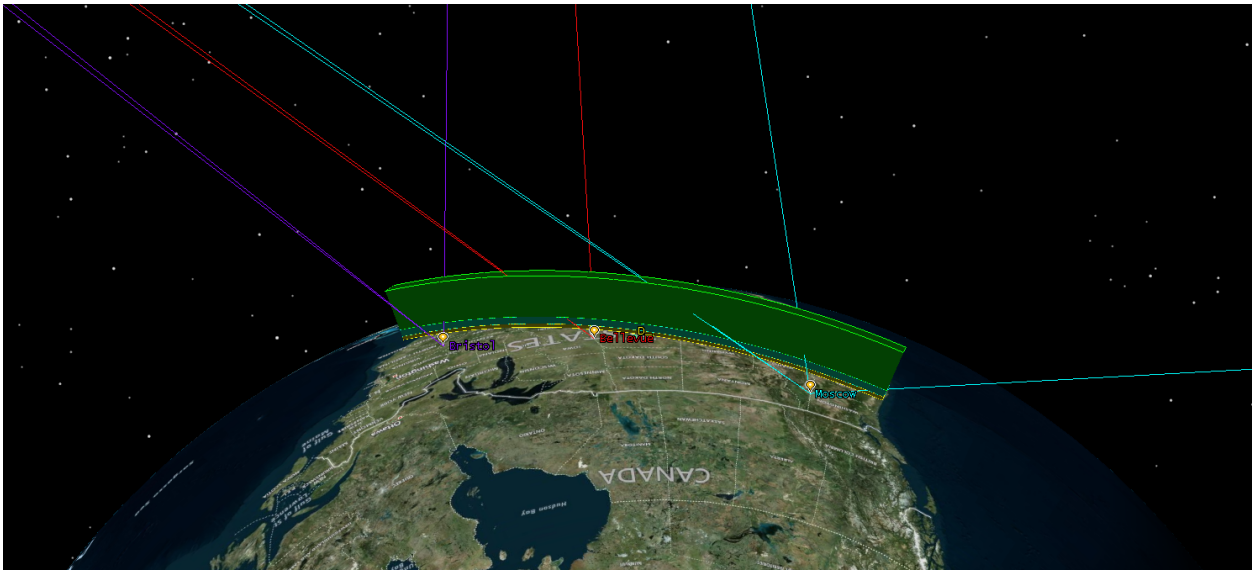

Figure 4.1: The three receiver node locations receiving downlinks from visible Inmarsat. Only I4F3, middle, goes through the eclipse region (green) for all three locations.

4.1.3 Inmarsat

Inmarsat is a constellation of private satellites used for communications. The satellites allow paid users to access the Internet and make voice calls anywhere in the world. There are twelve satellites currently deployed, all in geostationary orbit [49]. Although multiple Inmarsat satellites can be seen from the United States, only I-4 F3 Americas can clearly be seen by every location of interest while passing through the eclipse region, as shown in Figure 4.1. Each scintillation receiver location is a different color, and only the I4-F3 downlink (shown center) passes through the eclipse region (green) for each receiver location. Table 4.1 shows that the transmitted signal of interest for Inmarsat is between 1525 and 1559 MHz, meant for space-to-Earth transmissions.

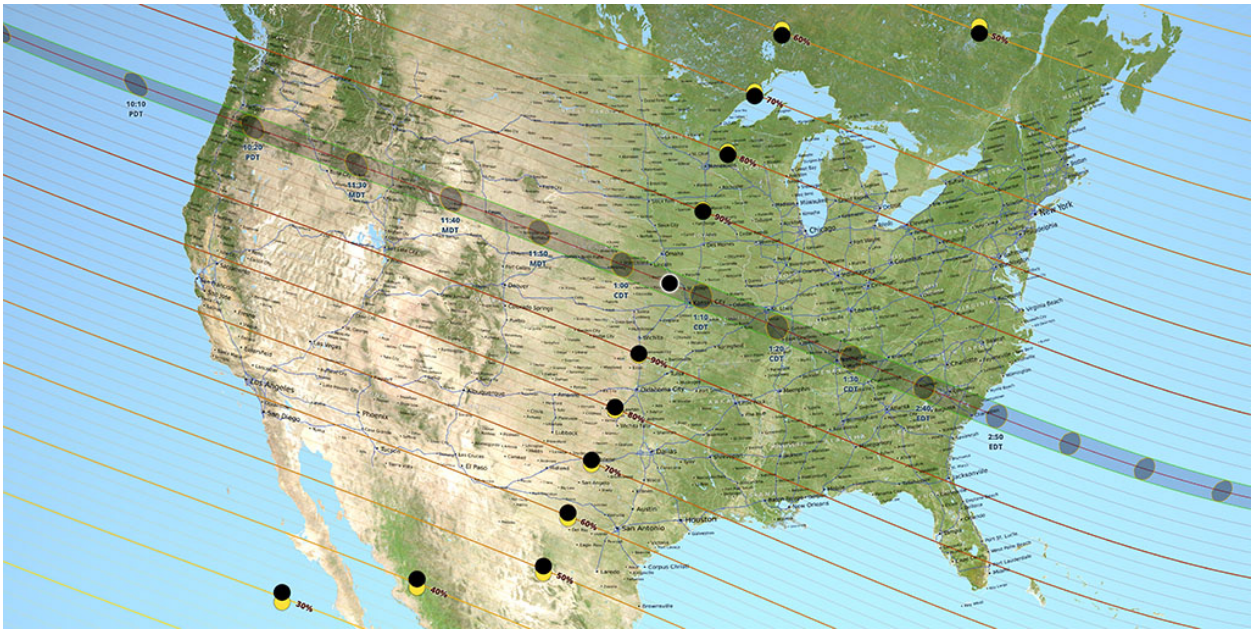

Figure 4.2: Map of totality of eclipse region [4].

4.2 Physical Location for Measurements

Since the solar eclipse will be visible throughout the majority of the continental United States, the scintillation receivers are scattered across the North American continent. While there may be a benefit to having the receivers within the same area to ensure the integrity of the measurements, it is even more beneficial to have them throughout the United States to gain more measurement data as the look directions to the satellites will be geographically different. As discussed later, the measurement tools were tested prior to the deployment of the scintillation receiver, so the integrity of the measurements are ensured by verifying the proper functionality of the receivers.

The eclipse will be begin off the coast of Oregon and continue across the United States to

South Carolina, as shown in Figure 4.2. There are only three scintillation receivers available due to budget constraints, so it was decided to place one receiver in Moscow, Idaho; one in Bellevue, Nebraska; and one in Bristol, Tennessee.

The locations were chosen to be north of the eclipse region so that the scintillation receivers will look through the F region in the eclipse path of totality when taking measurements, as shown in Figure 4.3. Figure 4.4 shows what would happen if the receiver nodes were placed in the path of the eclipse instead of north of it. Offsetting the receivers to the north of the eclipse path helps maximize the effects of the eclipse on the measurements. If instead the receivers were located in the eclipse region itself, the received signal path through the eclipsed portion of the ionosphere would be relatively short. This concept is illustrated in Figure 4.3, where the left shows the placement of the node in Nebraska to the north of the eclipse region, while the right side is a node in Kansas that is in the eclipse region. The D, E, and F regions of the atmosphere in the eclipse region are denoted by the varying colors of the region. The red line indicating a received signal is from the Inmarsat 4F-3 satellite.

The goal of the scintillation receiver is to have the received signal travel through the F regions of the atmosphere in the eclipse region. If scintillation occurs it will likely be in this region due to the instabilities that develop in this region. Figure 4.5 uses STK to verify the geometry of the Inmarsat's downlink by showing the received signal goes through the F region in the path of totality for the eclipse. Figure 4.6 shows the signals penetrating the F region of the eclipse. Both figures show that the received downlink signals pass through the eclipse region at varying heights. This enables the measurements to vary by height and by

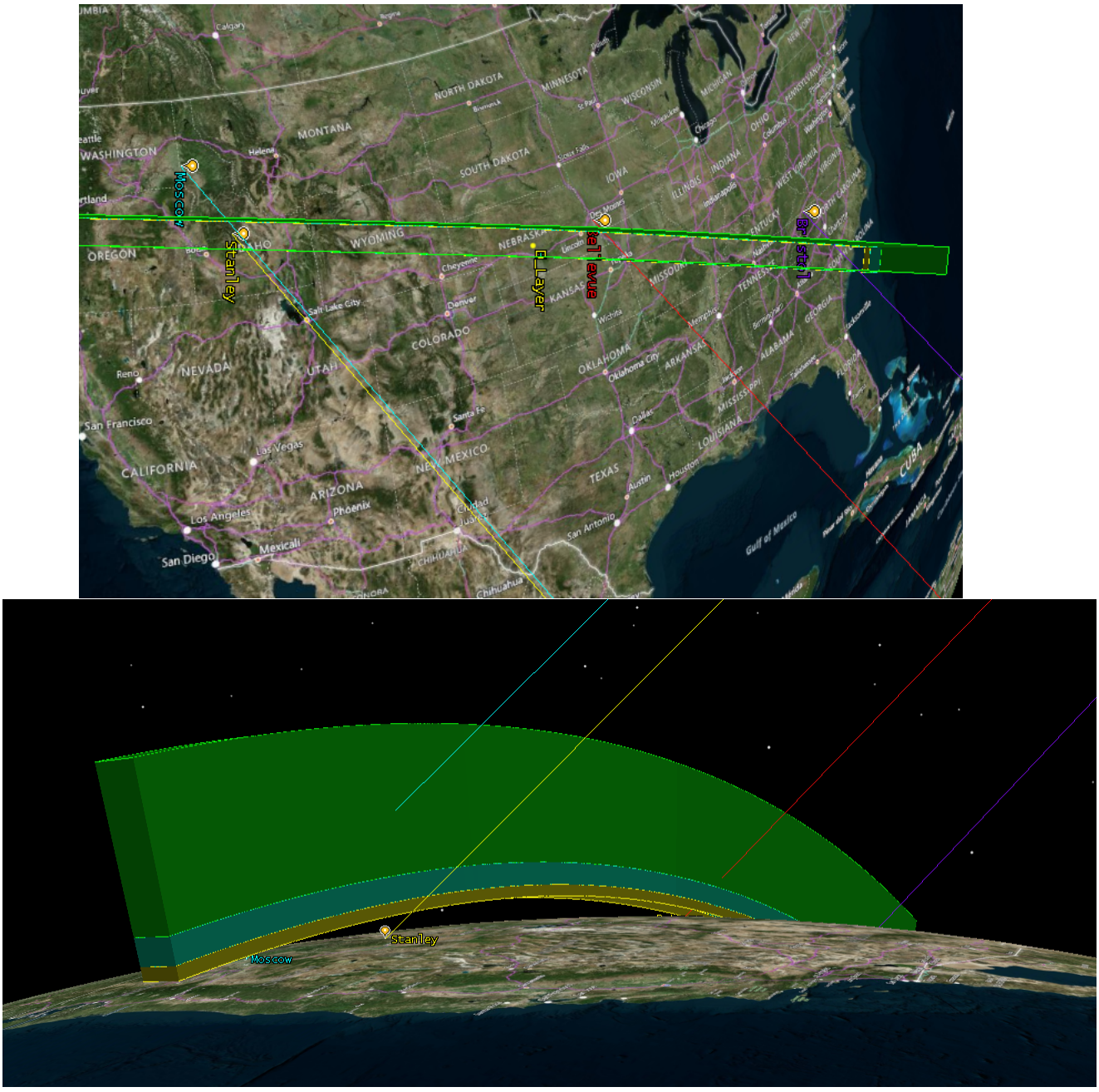

Figure 4.3: Stanley, ID, a city in the eclipse region (yellow), cannot be used as the received signal does not pass through the F region totality region (green).

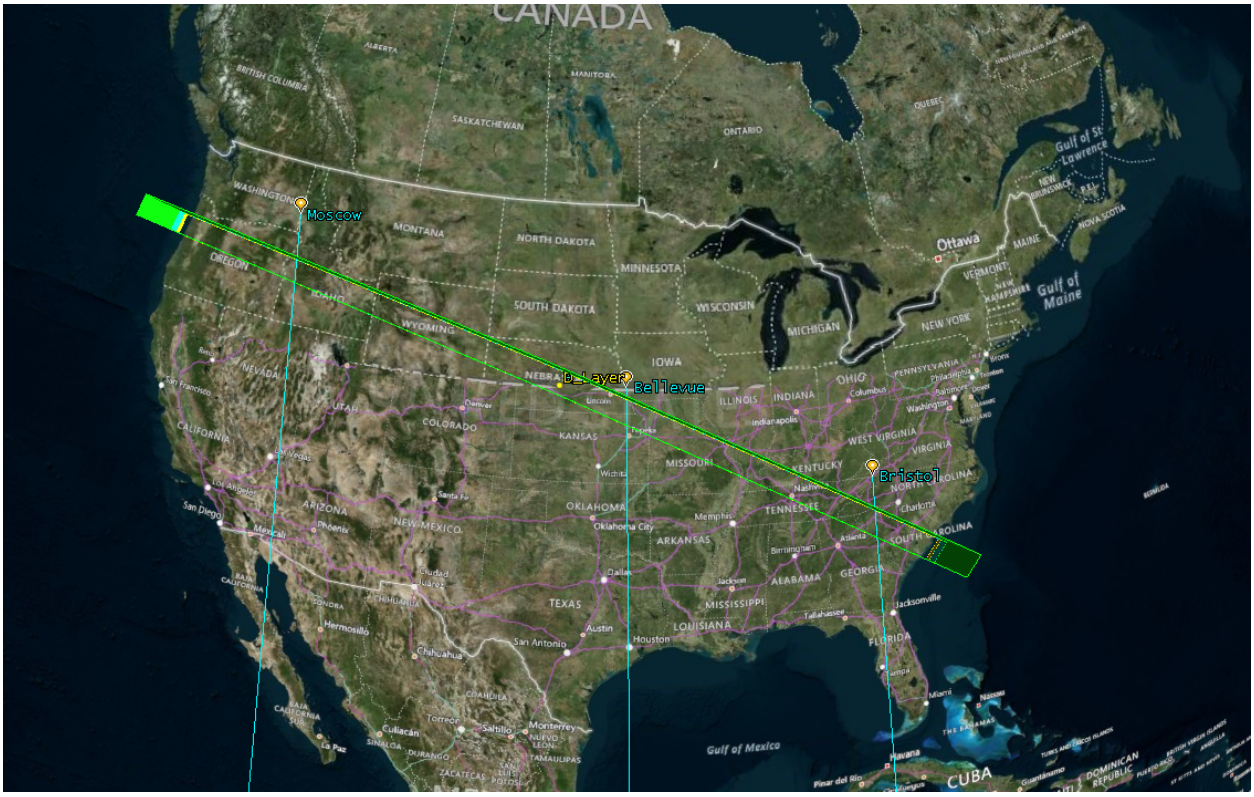

Figure 4.4: STK simulation showing the receiver node locations north of the eclipse region.

geographic location.

After figuring out the geometry needed to receive the signal and having the general areas of interest that were scattered throughout the country, it was determined to have one receiver node in the West, Midwest, and East in the United States. This is how Moscow, Idaho; Bellevue, Nebraska; and Bristol, Tennessee were chosen to be the deployment locations for the scintillation receiver nodes.

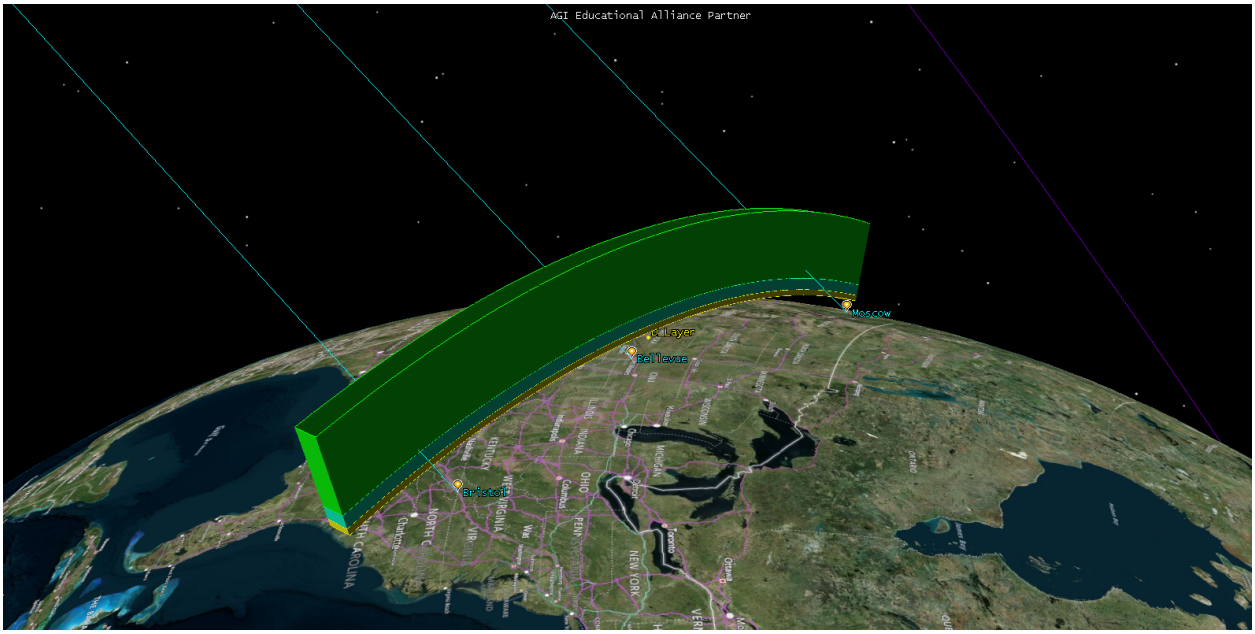

Figure 4.5: STK simulation showing the F,E, and D regions of the eclipse path with the receiver node locations shown.

4.3 STK Simulation

The System Tool Kit (STK) simulation of the satellite passes were started with Xiaoyu (Harry) Han and extended throughout this work. The STK simulation has the locations of interest (Bristol, TN; Moscow, ID; Bellevue, NE), satellites of interest (NOAA 15, NOAA 18, NOAA 19, Inmarsat), and the the connections made between the satellites and locations. This STK simulation uses the coordinates associated with the eclipse path of totality to show the regions of the ionosphere over this path, as shown in Figure 4.7. In this figure, the D region is in yellow, the E region is in blue, while the green depicts the F region in the ionosphere. This is important when determining physical locations for the measurements to ensure that the received signal would pass through the F region of the eclipse path as this

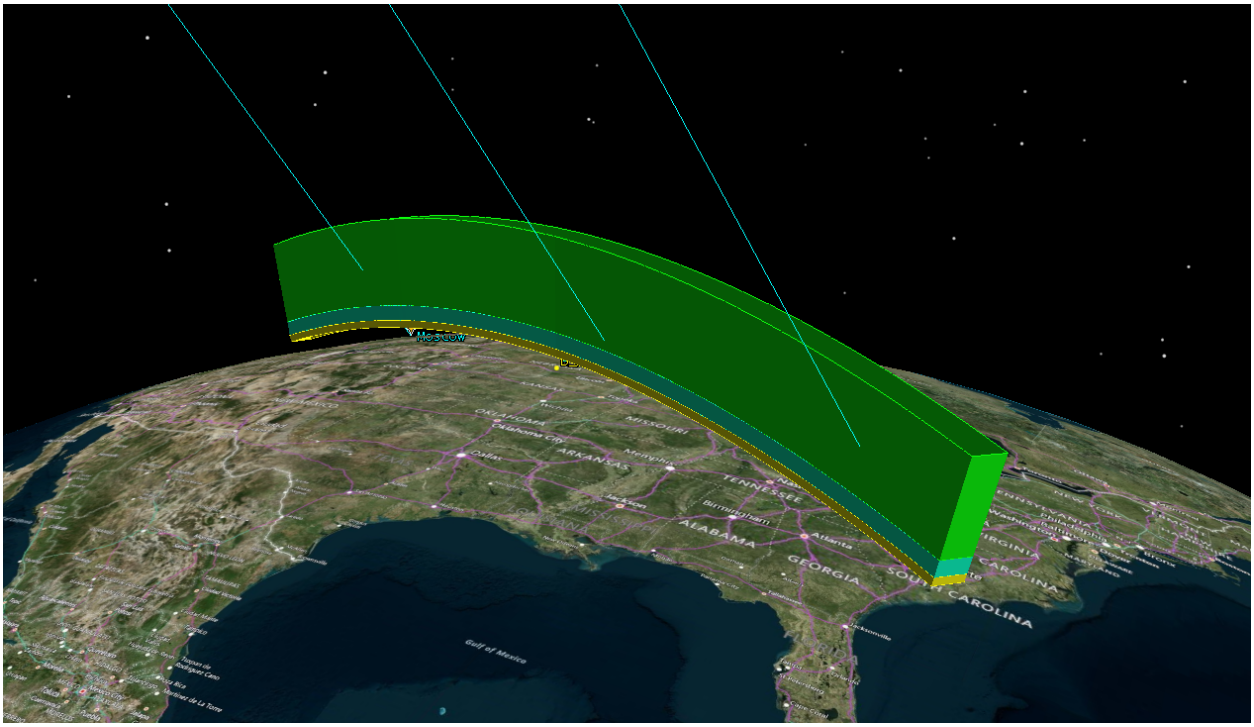

Figure 4.6: STK simulation showing the Inmarsat downlink going through the F, D, and E region of the eclipse.

is where scintillation will likely occur.

4.3.1 Look Angles

The patch antennas for receiving Inmarsat downlink need to have proper pointing in order to avoid having loss in the link budget associated with pointing offsets. The downlink for SARSAT also uses the patch antenna, but because the NOAA satellite is not able to be seen the entire time by the scintillation receivers (nodes), it was determined to point the nodes to the Inmarsat downlink since it will always be there. This also means that the receiver nodes will not be tracking the NOAA satellites as they pass overhead and instead remain in

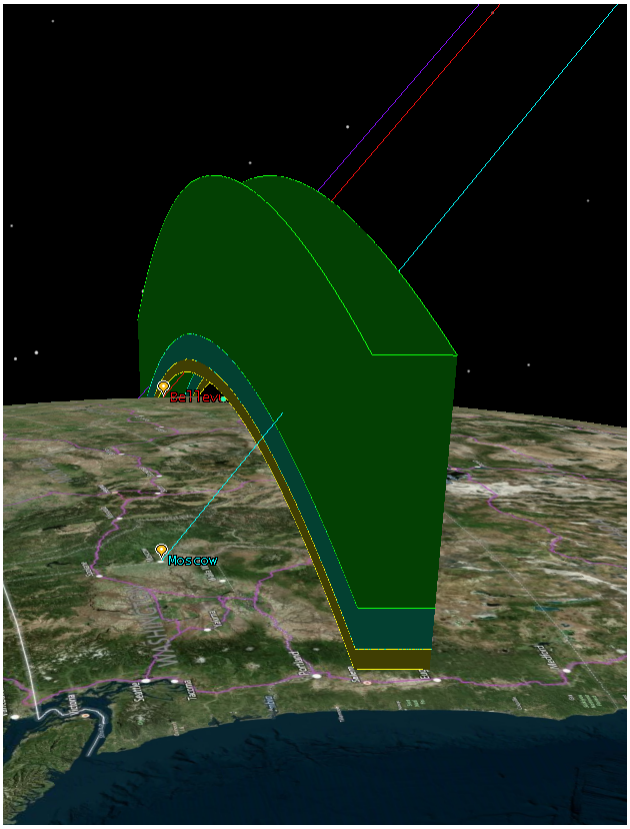

Figure 4.7: STK simulation of eclipse region with the ionosphere regions in the path of totality for the eclipse. Yellow is the D region, blue is the E region, and green is the F region in the ionosphere.

the fixed position.

There is a small amount of NOAA and SARSAT data lost by doing this, but if the nodes instead tracked the NOAA satellites as they passed overhead there would be losses to the Inmarsat data. Further, there would be risk of not returning the node to the original position which might affect the integrity of the data collected. The good news is that the egg beater antenna for the NOAA downlink is, for these idealistic purposes, omnidirectional and will not lose much by not tracking the NOAA satellites as they pass. Therefore it was decided

to keep the nodes at the fixed position looking towards the Inmarsat downlink.

The look angles were determined separately for each receiver node site. The look angle determines what azimuth and elevation angle the receive antenna need to be aligned to in order to maximize the receive signal. Each of these angles depend on the latitude and longitude of the earth station and the satellite. Since Inmarsat is in geostationary orbit, there were simplifications that could be made to the original equations, shown below [50].

$$cos(\gamma) = cos(L_e)cos(l_s - l_e)$$

$$El = tan^{-1}\frac{(6.6107345 - cos(\gamma))}{sin(\gamma)} - \gamma$$

$$tan(\alpha) = \frac{tan|(l_s - l_e)|}{sin(L_e)}$$

$Az = 180° - \alpha$ if the satellite is southeast of the earth station, and $Az = 180° + \alpha$ if the satellite is southwest of the earth station [50].

L_e is the latitude of the earth station in degrees north, l_e is the longitude of the earth station in degrees west, l_s is the longitude of the satellite in degrees west, Ez is the elevation angle needed in the earth station, and Az is the azimuth angle needed in the earth station for that satellite.

Table 4.2 shows the latitude, longitude, azimuth, and elevation angle for each of the node locations where the longitude of the satellite is 98.4°W [49]. These values were found using the equations above in a Matlab script.

Moscow, ID			
Latitude ($^\circ N$)	Longitude ($^\circ W$)	Elevation ($^\circ$)	Azimuth ($^\circ$)
46.73	117.00	33.24	115.19
Bellevue, NE			
Latitude ($^\circ N$)	Longitude ($^\circ W$)	Elevation ($^\circ$)	Azimuth ($^\circ$)
41.16	95.91	42.37	183.77
Bristol, TN			
Latitude ($^\circ N$)	Longitude ($^\circ W$)	Elevation ($^\circ$)	Azimuth ($^\circ$)
36.56	82.21	44.26	206.00

Table 4.2: Look angles for each receiver node location.

4.3.2 Access Times

When attempting to model satellite passes using the orbital elements gathered from two line elements (TLEs) associated with the satellite, keep in mind that irregularities in the space environment cause the satellite's orbit to slightly change over time. Atmospheric drag (for a LEO satellite), gravitational fields of the sun and moon, solar radiation pressure, and asymmetry of the earth's gravitational field all cause the satellite's orbit to slightly change [50]. For this reason, the STK simulations presented here may be slightly inaccurate and the simulation should be re-ran closer to the eclipse time. Nonetheless, the current simulation, using TLEs obtained on June 4th, 2017, should be close to the actual event.

To get the access times for the three node locations with NOAA 15, 18, and 19, approximations to the receiver antennas had to be made. Sensors were used to model the antennas in STK,

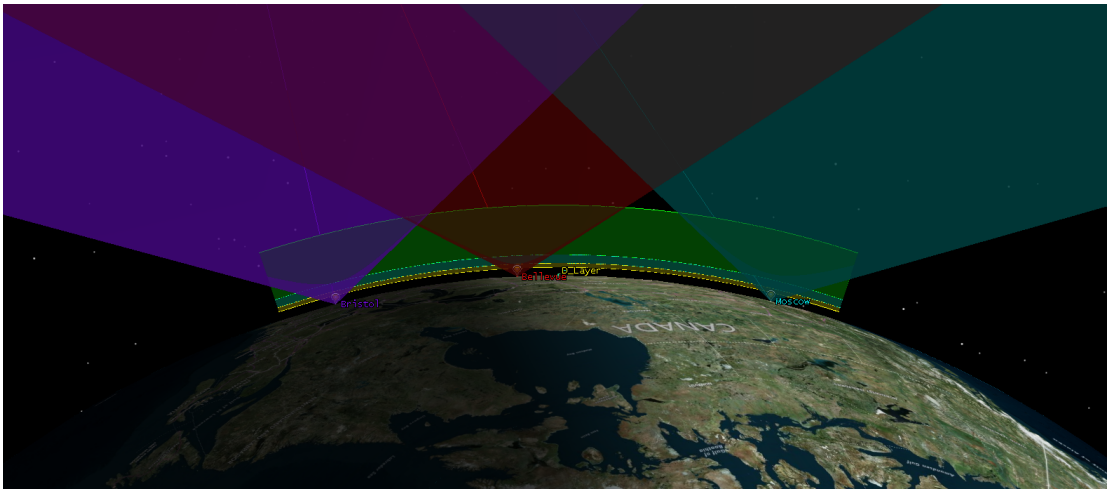

Figure 4.8: STK simulation representation of Inmarsat patch antenna before pointing is applied with each receiver location modeled as a different color.

one NOAA sensor and one SARSAT sensor per location. The NOAA sensor was modeling an egg-beater and had a 80° half angle beamwidth. The SARSAT patch antennas roughly have a 60° half angle beamwidth. Since the look angles were known for each location, the node was modeled as having the patch antenna pointed towards Inmarsat while the egg-beater had no pointing associated with it (was pointed straight up), shown in Figure 4.8 with each receiver location denoted as a different color.

From here, access points were generated for each antenna interacting with the NOAA satellites. These times were then checked for any cross-listing, shown in Table 4.3. This cross-listing signifies the NOAA satellite being visible for both the NOAA egg-beater antenna and the SARSAT patch antenna. These times are important since they determine when the NOAA and SARSAT receiver GNU Radio flowgraphs will be running. The receivers for SARSAT and NOAA will only be on for these access times since there is no need to waste

Moscow, ID			
Satellite	Start Time (UTC)	Stop Time (UTC)	Duration (s)
NOAA 19	22:53:14	22:55:06	113

Bellevue, NE			
Satellite	Start Time (UTC)	Stop Time (UTC)	Duration (s)
NOAA 19	21:10:24	21:13:46	203

Bristol, TN			
Satellite	Start Time (UTC)	Stop Time (UTC)	Duration (s)
NOAA 19	21:08:39	21:11:37	179

Table 4.3: Access times for each location and relevant NOAA satellite passes.

limited storage space when the satellite is not present. At all other times, even when the SARSAT and NOAA receivers are running, the receiver for Inmarsat will be collecting data.

Although there is NOAA 15 passing over the Bristol location around the time of the eclipse, it is not visible to both the patch and egg-beater antennas and may not be considered. A similar situation is for NOAA 18, so none of those passes are used either. Still, the best luck is with NOAA 19. NOAA 19 is visible to all locations at some point within a few hours of the eclipse passing over, detailed in Table 4.3.

According to the current TLEs, none of the NOAA satellites will be overhead during the totality of the eclipse. However, there will be several passes by NOAA 19 close afterwards which may still lead to interesting data.

4.4 Measurement Tools Developed

Although there may be pre-made solutions to take scintillation measurements, it was decided that these tools should be developed in house to ensure the quality of the work, allows for customization, and to help with the budget. Chapter 5 discusses the measurements that were taken with the scintillation receiver nodes to verify proper operation and setup.

4.4.1 Hardware

All of the components, aside from the antennas and cables, will be inside a weatherproof enclosure as shown in Figure 4.11 and 4.9. Inside this enclosure there will be a B200 USRP that receives the VHF transmitted signals. The B200 is ran by an ODROID XU4, a single-board computer. This computer controls the elements comprising the scintillation receiver (node), and is remotely controlled people in the Virginia Tech Ground Station operation center. The ODROID XU4 also controls a USB 2.0 hub where two RTL-SDRs are connected to the L band patch antennas. A GPS antenna is also connected to the USB Hub as a reference to ensure the accuracy of the received signals by allowing a high-accuracy reference. There are large file sizes associated with each capture, so a 1 Terabyte solid state hard drive was added in for data storage. When the nodes are deployed and after the initial setup, all that the nodes need to operate is Ethernet for remote access and file sharing and power to run. Since the budget is small, the ability to remotely operate the nodes and not have to have a person present at all times is a huge advantage.

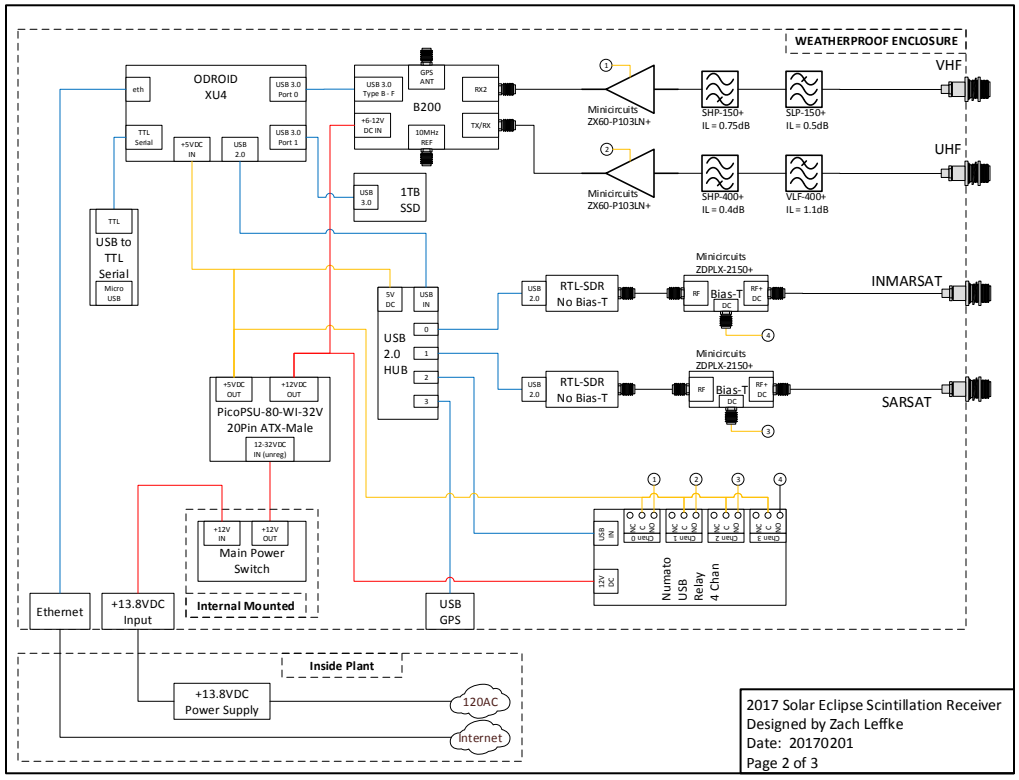

Figure 4.9: Detailed block diagram of inside the weatherproof enclosure of the scintillation receiver node.

After deciding which satellites would be used to take scintillation measurements, the hardware tools to record these measurements were finalized. Zach Leffke and Xiaoyu (Harry) Han were the driving forces in designing and building the hardware for the scintillation receivers, otherwise known as nodes.

As discussed in Section 4.1, even though the downlinks of Inmarsat and SARSAT are close to one another, the difference in polarization introduces a need to have separate antennas for each. This leads to the requirement for three receive antennas at each scintillation receiver site. Each receiver will be reproduced three times in order to have the exact same

Figure 4.10: Scintillation receiver node.

scintillation receiver at each location.

The NOAA downlink is in Very High Frequency (VHF, 30-300 MHz), so an egg-beater antenna was used. The antenna came in a kit with a UHF egg-beater antenna so that was mounted on the node as well. Patch antennas are used for the L-band (1-2 GHz) downlinks, one is right-hand polarized for the Inmarsat receiver and the other is left-hand polarized for the SARSAT receiver.

4.4.2 Software

Scintillation is measured by finding the peak average power ratio (PAPR) of the received signal [3]. PAPR can be found by finding the maximum power over a certain time period

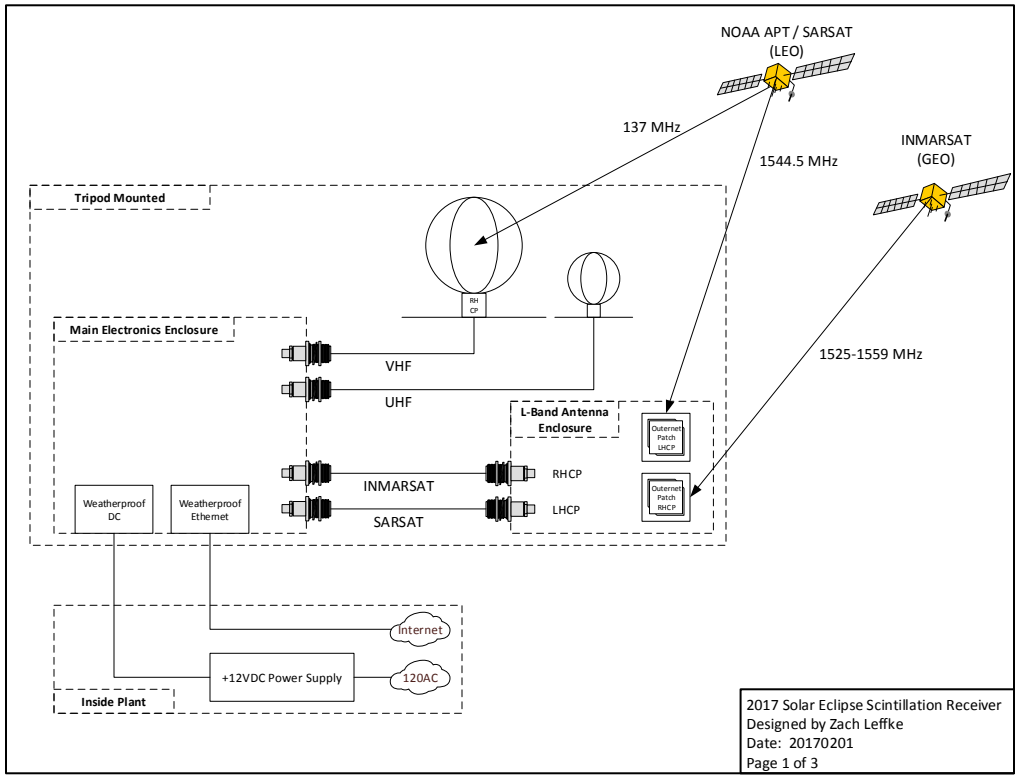

Figure 4.11: Block diagram showing receiver node setup.

and dividing that by the average power of the signal over the same time period. PAPR is easier to accomplish in decibel units. Therefore, instead of dividing the two values they can instead be converted into decibels and subtracted.

Finding the PAPR of the received signal can done on most programming platforms, but in this project GNU Radio was used. Although other languages could have been used, GNU Radio was chosen due to the familiarity and capabilities of the software as discussed in 2.2.1. This experiment uses pre-made blocks to ensure that no specialty scripts had to be included for each node. Although using only the blocks that came with the standard instillation

complicates the flowgraph, it reduces the possibility of problems.

Due to the heavy averaging that is done by the GNU Radio flowgraph, it was decided that during the eclipse raw data would be recorded and stored in a file. The files would then be analyzed in post-processing to find the scintillation measurements, as discussed in Chapter 5. Because of this, only the initial receive chain flowgraph is discussed here. One of the only differences between the flowgraphs is the received frequency of each is matched to the downlink frequency of the satellites. Additionally, the flowgraph associated with the NOAA downlink will have GUI frequency sink to ensure that data for the NOAA and SARSAT downlinks are only being recorded when the satellites can receive the signal. For instance, if NOAA 18 is passing over one of the sites, at a certain point the satellite will go behind the patch antenna meaning SARSAT downlink can no longer be recorded since the patch can no longer detect the satellite.

The receive-chain flowgraph itself is simple, with the majority of the work being done post-processing. The initial receive chain flowgraph has an UHD input that links the B200's and RTL SDRs with the GNU Radio flowgraph. This USRP Hardware Driver (UHD) input then goes to the file sink that records the raw signal. Although things like Doppler could have been accounted for at this stage, Inmarsat will incur very little Doppler since it is in geostationary orbit. The Doppler associated with the transmitters on-board the NOAA satellites can be used as a comparison tool post-processing that is beyond the scope of this work. Decimation of the signal is also done in order to reduce the file size of the capture, since there is a finite storage space to hold the recordings. A sample rate of 250k samples

per second is used for all recordings as both the B200 and RTL-SDR clock rate handle this value well. A higher sample rate could have been used but was found unnecessary as the bandwidth of the signals are small and there is a finite amount of storage available for the signal recordings.

Chapter 5

Measurements and Results

The scintillation measurement flowgraph, as shown in Figure 5.1, measures amplitude fluctuations of the received signal over a fifteen second period. The flowgraph starts with a file source, as scintillation measurements are done after the eclipse. The gain associated with the antennas is not large and the DC spike can rival that of the signal, so a DC Blocker was used for the NOAA and SARSAT recordings. It is not needed on the Inmarsat recordings as those should be close to DC and a blocker at DC may harm the integrity of the signal. On the other hand, SARSAT and NOAA recordings will have signals that move in accordance to Doppler and a DC blocker will be useful as long as the signal does not pass over DC. A throttle is needed in GNU Radio companion when using a file source so the data is limited to the provided sample rate.

The throttled signal is then put into a vector form and undergoes a fast Fourier Transform, FFT, to find the maximum signal strength in frequency. The size of the FFT was increased

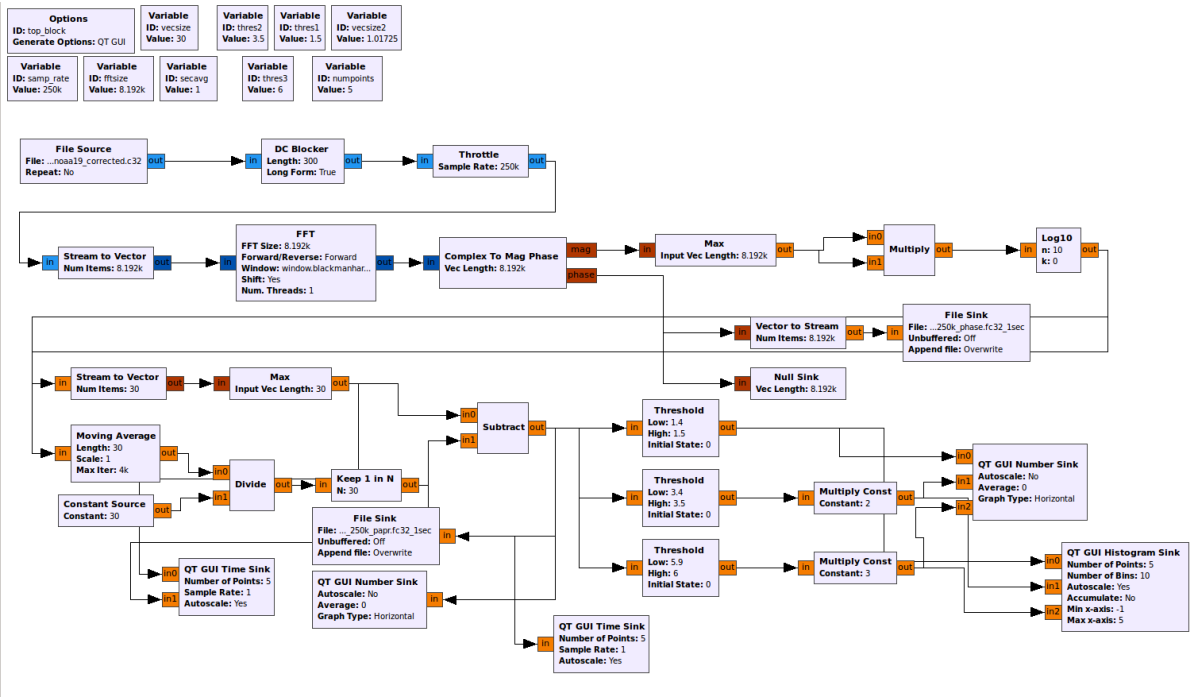

Figure 5.1: GNU Radio ionospheric scintillation receive flowgraph, post processing.

from 1024 to 8192 in order to more accurately find the maximum signal strength. From there, the signal's magnitude and phase is found. Although the phase scintillation could be measured from here, it is a first priority to measure amplitude scintillation. This is why the phase scintillation goes directly to a file sink after converting to the right file type.

The maximum of the magnitude of the FFT is found first. The scintillation measurements require the maximum of the signal and discards the rest of the information. The maximum of the FFT signal is converted into decibels by squaring the magnitude and taking the log of it. From this point, the peaked to average power ratio takes over. There are two streams coming from the log block, one that finds the largest maximum over a specified interval and another that finds the average maximum over that same interval.

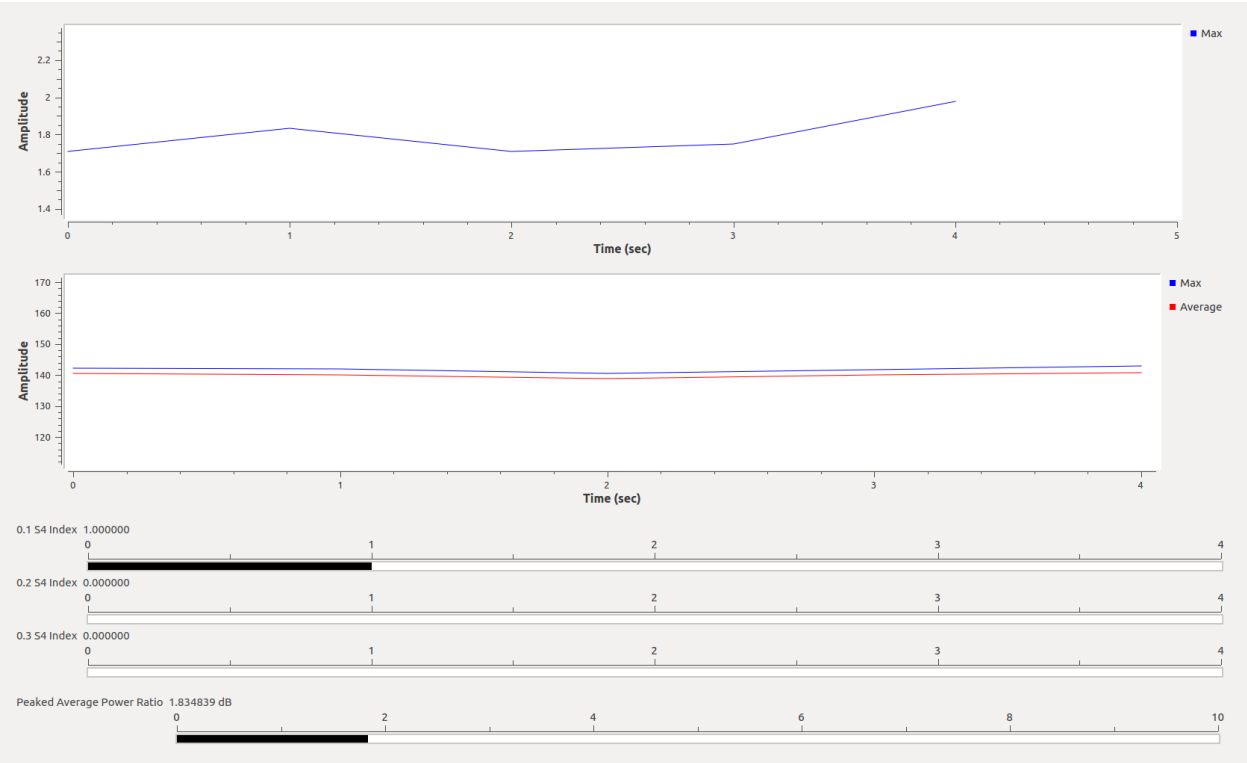

Figure 5.2: Graphical output of GNU Radio scintillation receive flowgraph.

To find the average of the maximums, a moving average block is used. The moving average is not scaled properly, and needs to be divided by the time interval it is taken over. From there, only one of the averages is used. The moving average is a continuous moving average, but for the purposes of this work a vector average is needed, thus the use of the keep one in n block. This average is then subtracted by the maximum of all the maximums over the time interval, since it is in decibels rather than linear units, thus producing the peaked to average power ratio. A graph showing the maximum versus the average of the maximums is shown in Figure 5.2. This figure shows the PAPR on the top graph, while the average (red) and maximum (blue) are compared on the graph below. The number sinks below that

show the corresponding S_4 indexes as well as the actual value of PAPR.

The scintillation measurement, in decibels, is recorded in a data file. In order to keep from having to go through the entirety of the file, thresholds were used to determine if the power fluctuation went above nominal values. These common threshold values for S_4 are 0.1, 0.2, and 0.3 as these are all under the category of weak scintillation. The S_4 values are not in decibels and must be converted using the equation discussed in 2.1.3. Figure 5.2 shows the output of the flowgraph, where scintillation in mid-latitude regions rarely go above an S_4 index of 0.1, except for in the case of geomagnetic storms, but S_4 values below this value can be assumed categorized as scintillation not being present.

Traditionally, a fifteen second time period is used to measure scintillation, even though the period of scintillation is around one second [3]. Modern technology allows the use of the time period scintillation is measured to be shortened, and this work uses one second averages. This allows for the one second intervals to be averaged over fifteen seconds to compare with the traditional S_4 indexes if needed. Since the scintillation measurements are made post-processing, the value that the scintillation measurements are averaged over can be changed if needed.

SARSAT 7 and SARSAT 12 downlinks were recorded on June 9th with the original flowgraph at the Virginia Tech Ground Station. This run showed that there was weak to moderate scintillation present at 6:30 pm Eastern Time when, in theory, there should not have been any scintillation present. A MATLAB script was then created to account for the slant range and antenna beam pattern offset, yielding the Figures 5.6, 5.5, 5.4, 5.3.

The original file was cut to where it only showed when the satellite downlink was received. Original captures typically have a buffer before and after the satellite passes over to ensure the recording of as much of the downlink as possible. The start of the signal being visible was found in GNU Radio and the cut was implemented in the MATLAB script, with the new cut file being stored separate from the original capture.

For slant range effects to be accounted for, the range of the pass was found using STK. This STK simulation created a link to NOAA 15 and NOAA 19 and calculated the range as the satellites passed across, using the antenna patterns specified in 4. The range value was found in one second intervals and was squared and applied to the satellite downlink, thereby correcting slant range offsets present in the signal.

The antenna beam pattern offset was found by assuming there was a 6 dB offset on the edge of the antenna while a 0 dB offset in the middle of it. A spline fit was then converted into linear units and used to match this curve to the time of the capture. The inverse offset antenna beam pattern was multiplied to the corrected slant range signal and saved to a complex binary output that was ran in GNU Radio.

5.1 SARSAT 7 Recordings

SARSAT 7 is on-board NOAA 15 and was recorded on June 9, 2017 around 6:30 Eastern Time. The one second averages have strong fluctuations when compared to that of the fifteen second averages. In Figure 5.3 and 5.4, the red line shows a S_4 index of 0.1, while the yellow

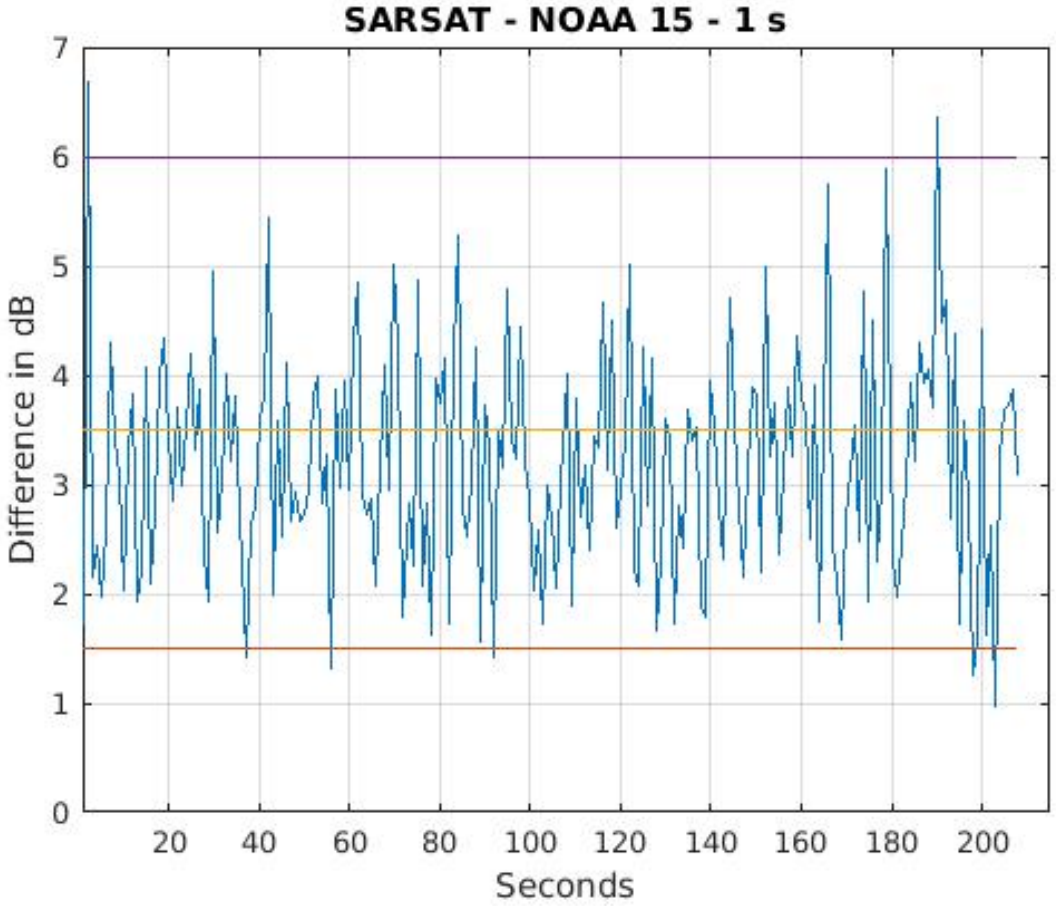

Figure 5.3: Scintillation indexes for SARSAT 7 pass over Blacksburg, VA June 9,2017 with one second averages.

line is 0.2, and finally the purple line is 0.3. The one second averages are relatively constant around S_4 index of 0.2, with a few strong distinct peaks that are close to 0.3. When averaged across fifteen seconds, these averages drop and all but one of the fifteen second averages are below 0.2. While slightly high for the region, the fifteen second averages are a cleaner, more constant value of S_4 and leads to a more reliable average.

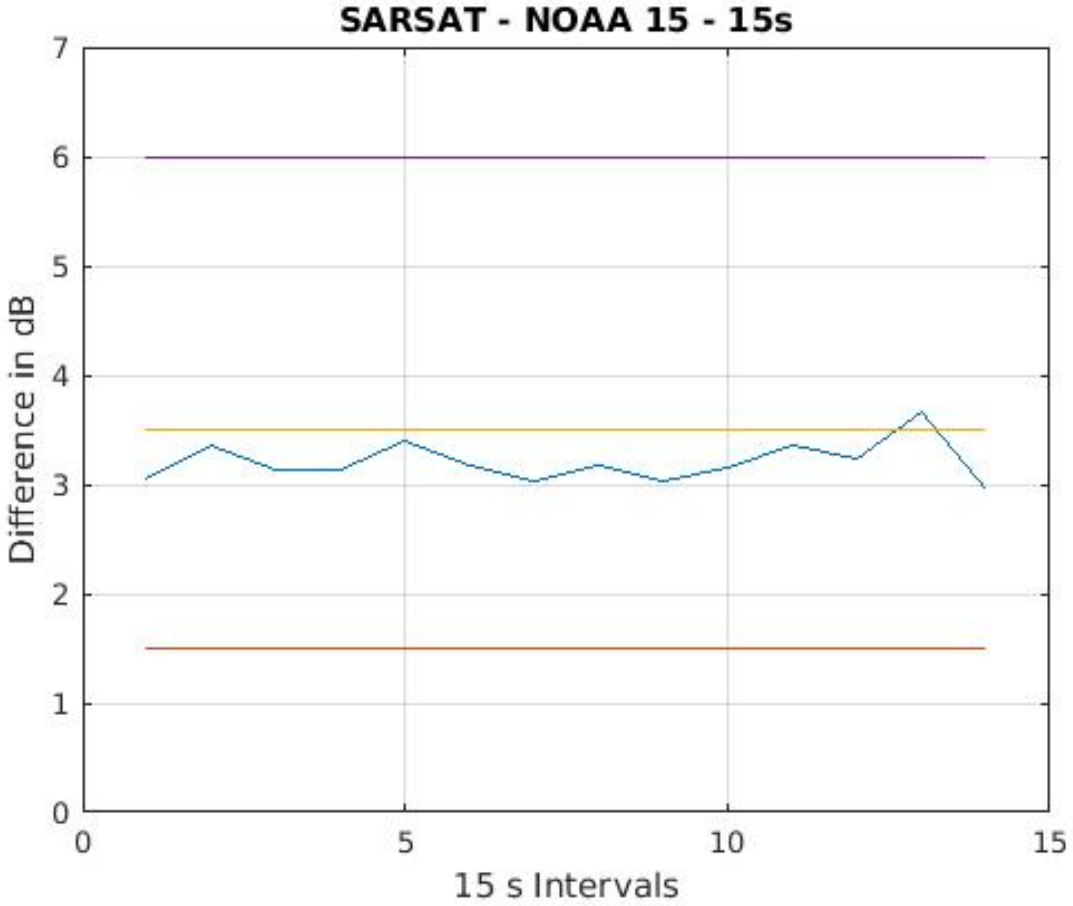

Figure 5.4: Scintillation indexes for SARSAT 7 pass over Blacksburg, VA June 9,2017 with fifteen second averages.

5.2 SARSAT 12 Recordings

NOAA 19 passed over the Virginia Tech ground station on June 9th around 6:30 pm Eastern Time. On-board this satellite was SARSAT 12 and the downlink associated with SARSAT 12 was recorded for scintillation measurements. The one second averages, Figure 5.3 do not have large spikes of high S_4 indexes like the SARSAT 7 downlink and are overall lower in S_4 values. Figure 5.4 match the one second averages of SARSAT 7 well, with a more accurate

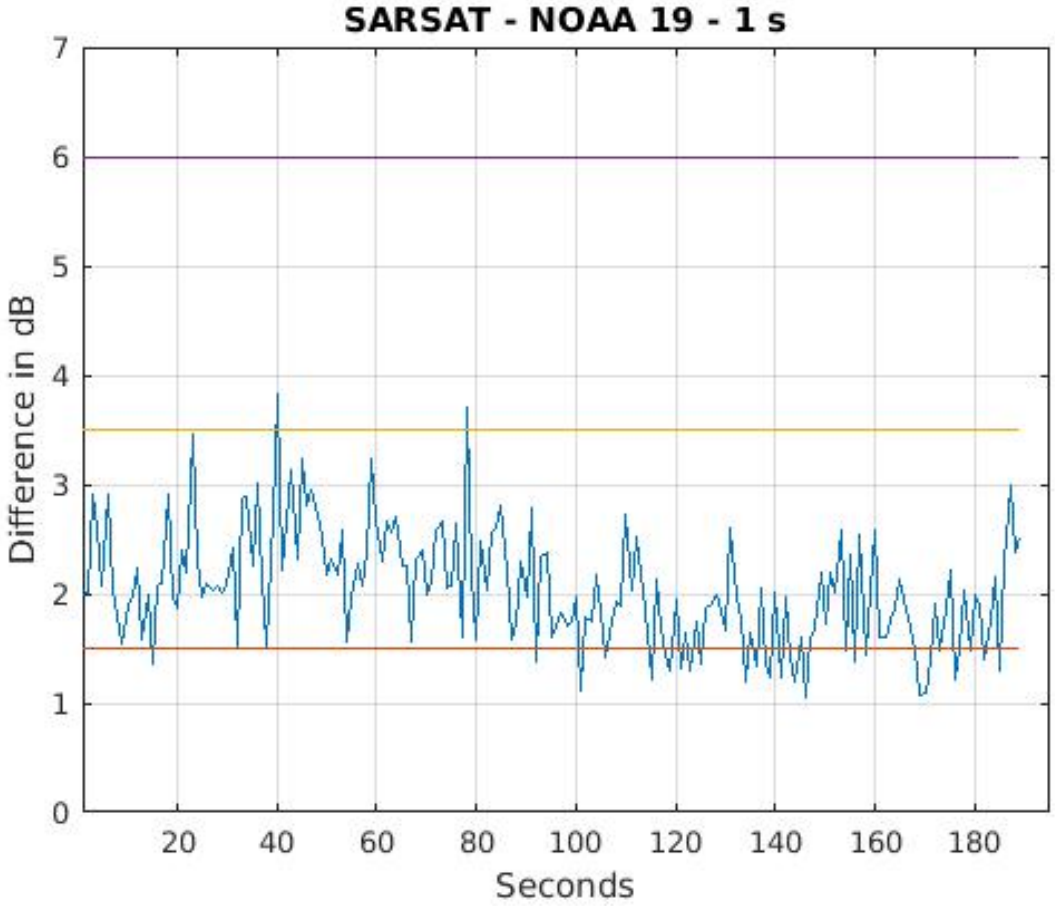

Figure 5.5: Scintillation indexes for SARSAT 12 pass over Blacksburg, VA June 9,2017 with one second averages.

lower value of S_4 index. Overall, the scintillation measurements for SARSAT 12 for both the fifteen second and one second averages show very promising results.

5.3 Discussion

The recordings of the SARSAT downlink signals by the receiver nodes show that data was accurately received and stored. This is a needed validation to have faith that the

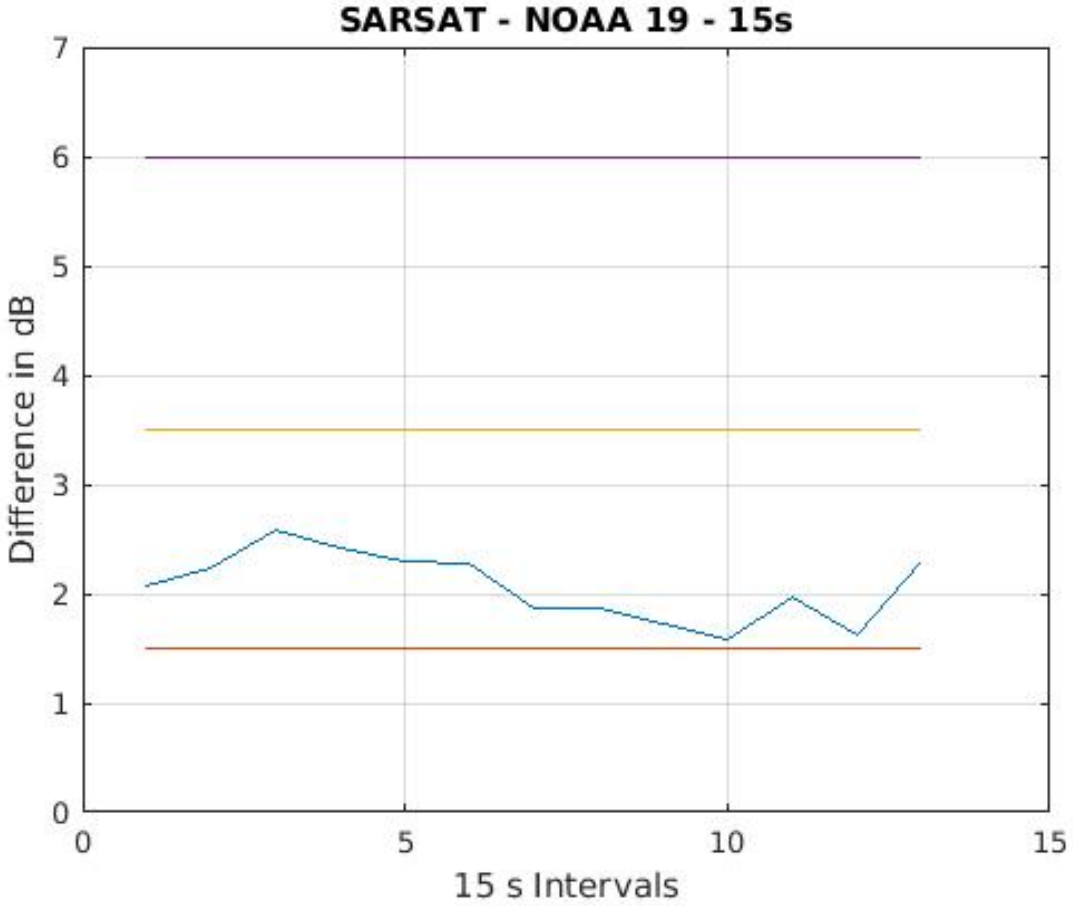

Figure 5.6: Scintillation indexes for SARSAT 12 pass over Blacksburg, VA June 9,2017 with fifteen second averages.

eclipse measurements are recorded properly. The post-processing scintillation measurement produces scintillation measurements in power fluctuation values and needs to be converted to S_4 indexes if it is to be compared with historical results. For this work, the scintillation measurements were left in decibel form, as many tend to think in decibels rather than S_4 indexes.

The post-processing scintillation measurement flowgraph and MATLAB script pairing are

working. However, one additional consideration might be to add a more accurate antenna beamwidth correction. This can be seen by comparing Figure 5.4 to Figure 5.6. The SARSAT 12 pass had better geometry for passing closer to the node while the SARSAT 7 pass was closer to the edge of the beamwidth. By being further on the edge of the beamwidth, the antenna beamwidth correction was not as accurate which led to a higher S_4 index. Overall, the scintillation measurement flowgraph and corresponding MATLAB script are successful in measuring scintillation regimes (weak, moderate, strong), though the exact value of the indexes may need to be corrected for satellite passes on the edge of the antenna beam pattern.

Chapter 6

Future Work

This chapter introduces work that could be done in the future to further extend the project. This includes things that could be done before the eclipse as well as things that could be done afterwards once the data has been collected.

6.1 STK Simulation

As discussed in 4, the TLEs that were used to generate the access times may have a margin of error associated with them. Because of this, the STK simulation should be updated at regular intervals, such as bi-weekly, in order to ensure that the access times are correct. These times are important for knowing when to turn on NOAA and SARSAT data collectors.

6.2 Data Collection

Something that was not discussed in this work is the timing of the data collection. Due to the high file size and limited storage space, the data may not be able to be collected throughout the entire duration of the eclipse. The total eclipse will only last for around three minutes, so data could be collected this whole time. The time surrounding this totality is also important and data should be collected as much as possible once the eclipse starts to occur. After the eclipse has passed and before it begins data should be collected sparingly. A script to automatically turn on data collection associated with the timing of the eclipse would be a useful tool for data collection.

6.3 Phase Scintillation

Phase scintillation was beyond the scope of this work. Phase scintillation is more applicable to higher altitude regions, but its role in mid-latitude scintillation is still being studied. For this reason, once the data from the eclipse is recorded phase scintillation measurements should also be taken and compared to nominal values.

6.4 Converting Platforms

The run time of the scintillation measurement flowgraph is rather long due to the heavy averaging that has to take place. To remedy this, it is suggested that a different platform

be used instead of GNU Radio to measure scintillation. GNU Radio could still be used to separate the magnitude and phase of the recordings, but from there a tool like python or C++ should be looked into for possible solutions to the delay time associated with the averaging.

6.5 Gradient Drift Instability

Although the TGI was found to grow faster than GDI, it would still be worthwhile to model GDI as well. GDI is the more traditional instability between the two, with TGI becoming a popular theory recently. GDI would offer another explanation of any instabilities that may arise during the eclipse as the interaction between the two has not been extensively studied.

6.6 Combining Instabilities

The TGI and GDI model are normally modeled separately, but an extension of this work would be to combine these instability models into one. This single model would be able to see how the TGI and GDI models mesh with one another and if the interaction between the two produce a greater scintillation scale size.

Chapter 7

Conclusions

This work discusses the possibility of ionospheric scintillation occurring because of the August 21, 2017 solar eclipse. Ionospheric scintillation is not common in mid-latitudes, but the instabilities that develop from the solar eclipse might cause scintillation to occur.

The temperature gradient instability (TGI) was modeled using data from the IRI and MSISE model for normal and eclipse conditions in Kansas City, KS. Under normal conditions and at the time of interest, the TGI would not be strong enough to produce scintillation. However, if both a strong electron temperature and electron density gradient are present, there is a possibility of scintillation being present.

The times associated with the inverse growth rates for TGI during the solar eclipse are small enough to develop during totality in the scale sizes of interest bounded by the altitude range of 200 km to 650 km. However, during the eclipse the electron temperature and electron density gradients are assumed to be going in the same direction which is different

than the geometry assumed in the TGI growth rate simplification. This means that the results presented in this chapter are an idealistic case and may not hold true during the eclipse.

NOAA 15, NOAA 18, NOAA 19, SARSAT 7, SARSAT 10, SARSAT 12, and Inmarsat 4-F3 downlinks are all used to measure scintillation during the eclipse. There are three scintillation receivers to the north of the eclipse region: Moscow, Idaho; Bellevue, Nebraska; and Bristol, Tennessee. These scintillation receivers will record the raw data of the received downlinks by utilizing GNU Radio. Corrections are made to the raw data in a MATLAB script to correct for slant range and antenna beam pattern offsets. In post-processing, the peak average power ratio is found of the recorded signal, linking it to S_4 scintillation measurement indexes.

Once it is closer to August 21st, the STK simulation should be re-run in order to get the most accurate timing information for satellite passes. Ultimately, there is a chance for ionospheric scintillation to occur due to the total solar eclipse, as discussed in Section 3.2. This information may help to better understand scintillation in mid-latitudes and the ionosphere as a whole. Although this work is completed before the eclipse, it provides the necessary tools and resources to measure and analyze ionospheric scintillation that may be produced by the event.

Appendix A

Appendices

A.1 TGI Eclipse Condition Plots

These figures are variations of the TGI model under eclipse conditions.

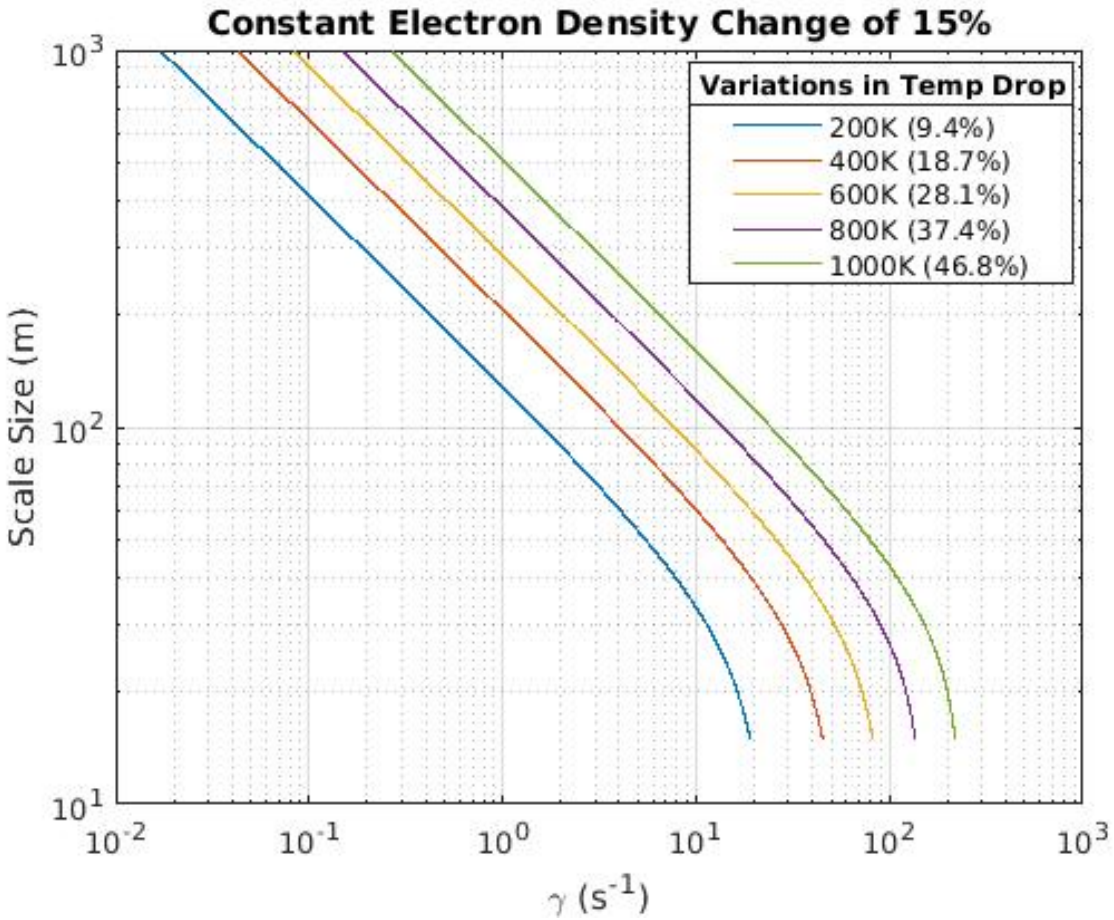

Figure A.1: Temperature gradient instability growth rate by scale size with variations in electron temperature drop under a electron density drop of 15 percent.

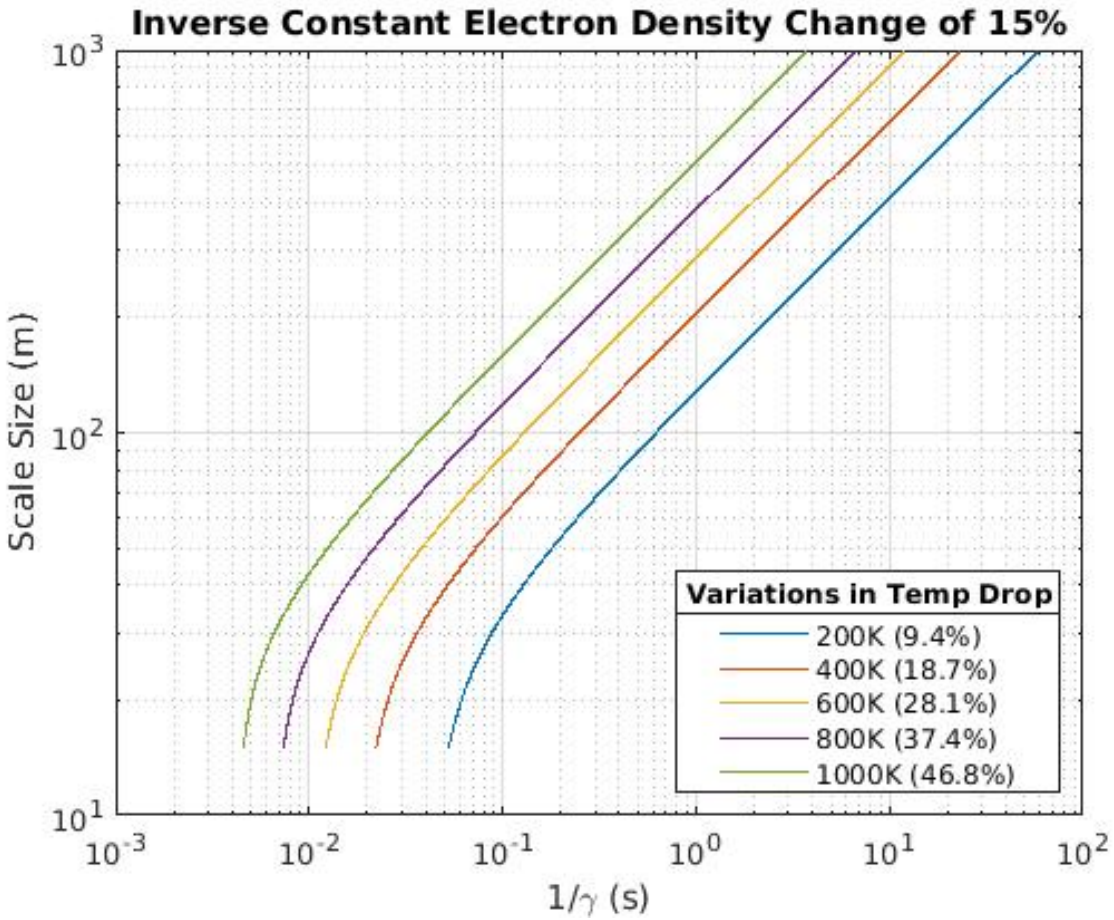

Figure A.2: Inverse temperature gradient instability growth rate by scale size with variations in electron temperature drop under a electron density drop of 15 percent.

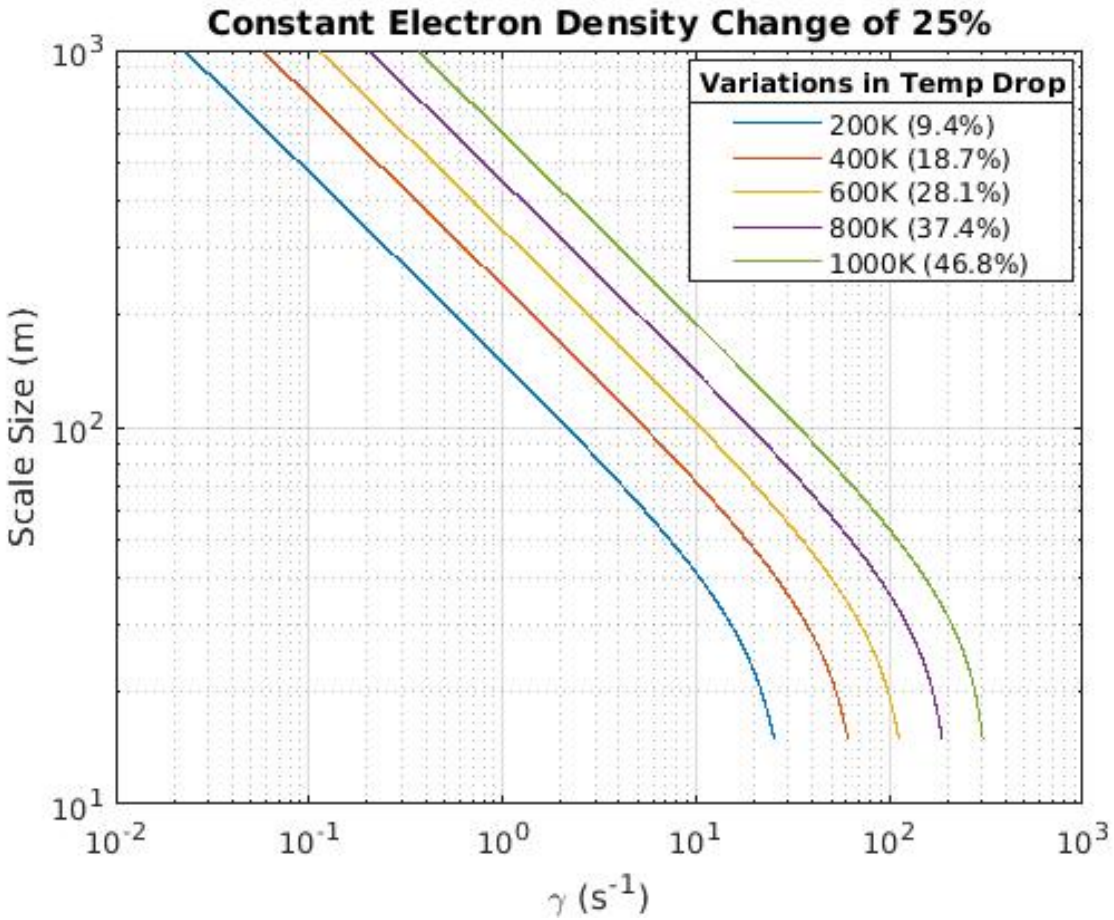

Figure A.3: Temperature gradient instability growth rate by scale size with variations in electron temperature drop under a electron density drop of 25 percent.

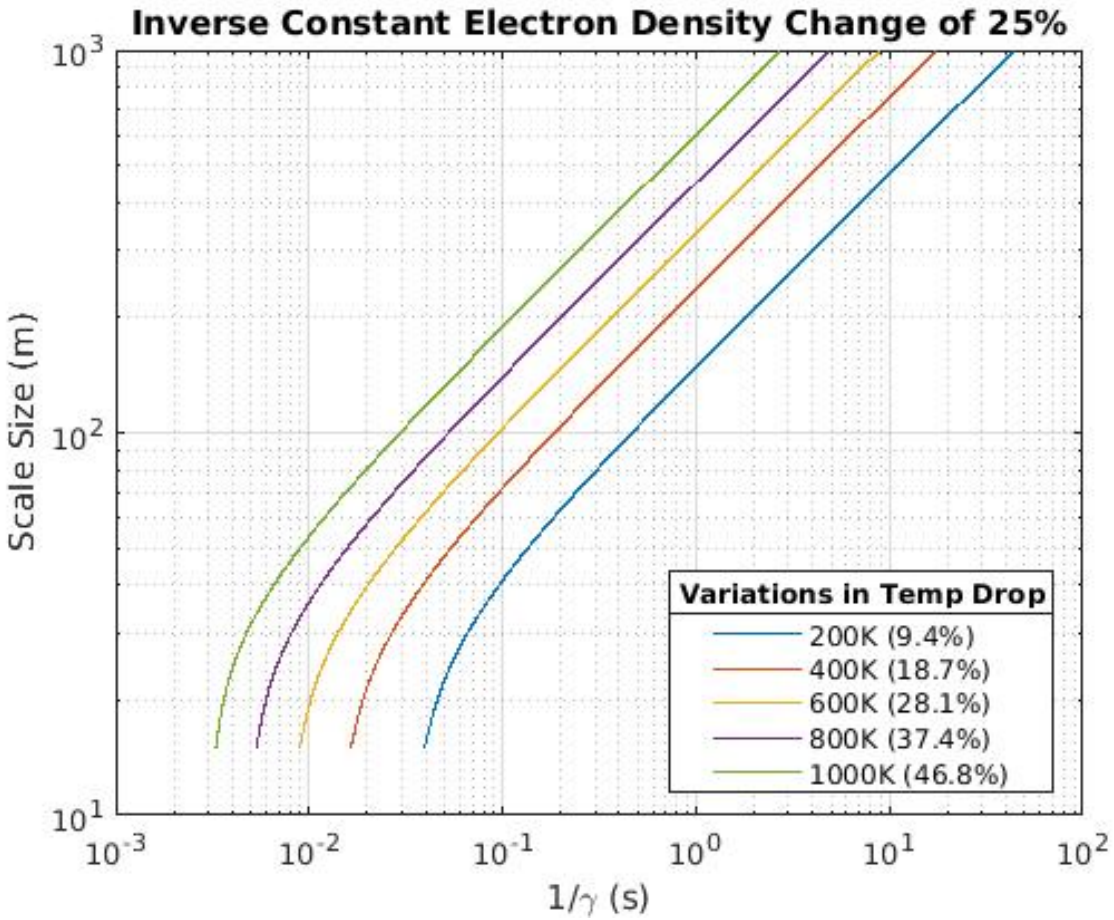

Figure A.4: Inverse temperature gradient instability growth rate by scale size with variations in electron temperature drop under a electron density drop of 25 percent.

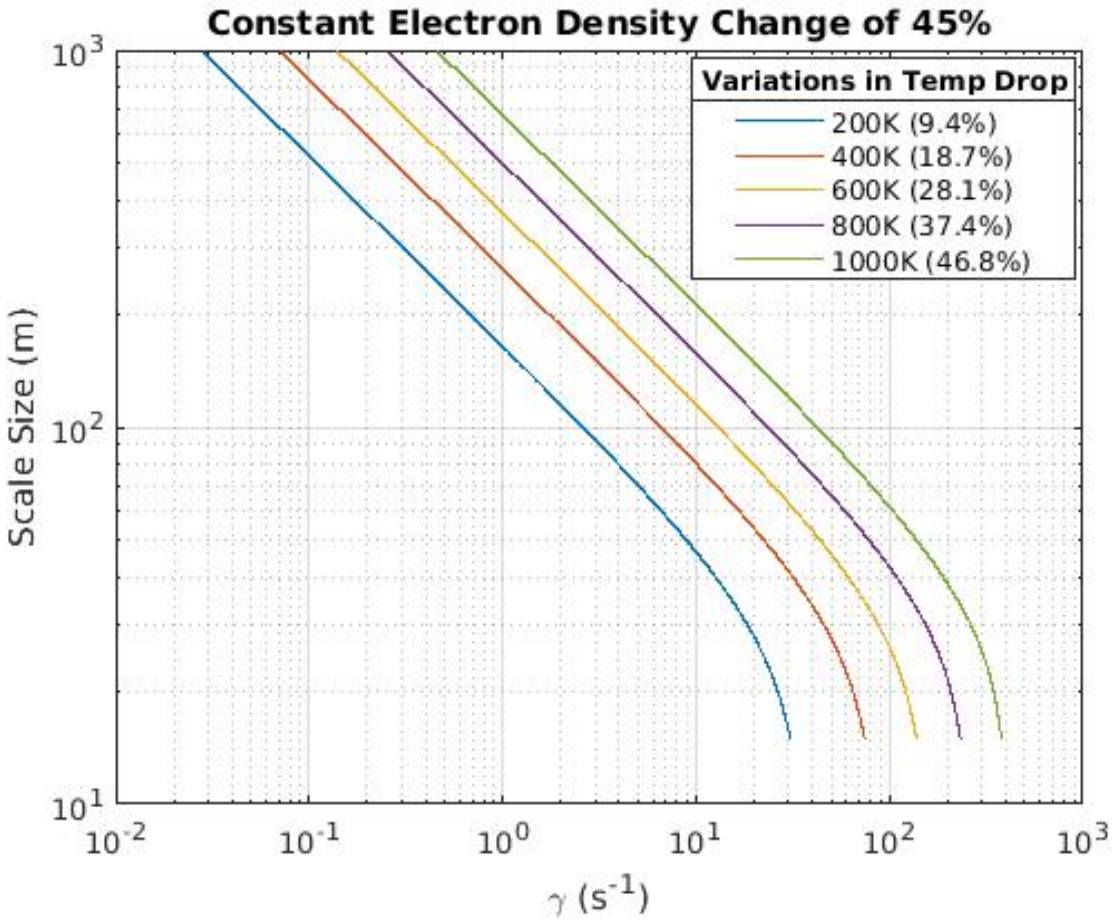

Figure A.5: Temperature gradient instability growth rate by scale size with variations in electron temperature drop under a electron density drop of 45 percent.

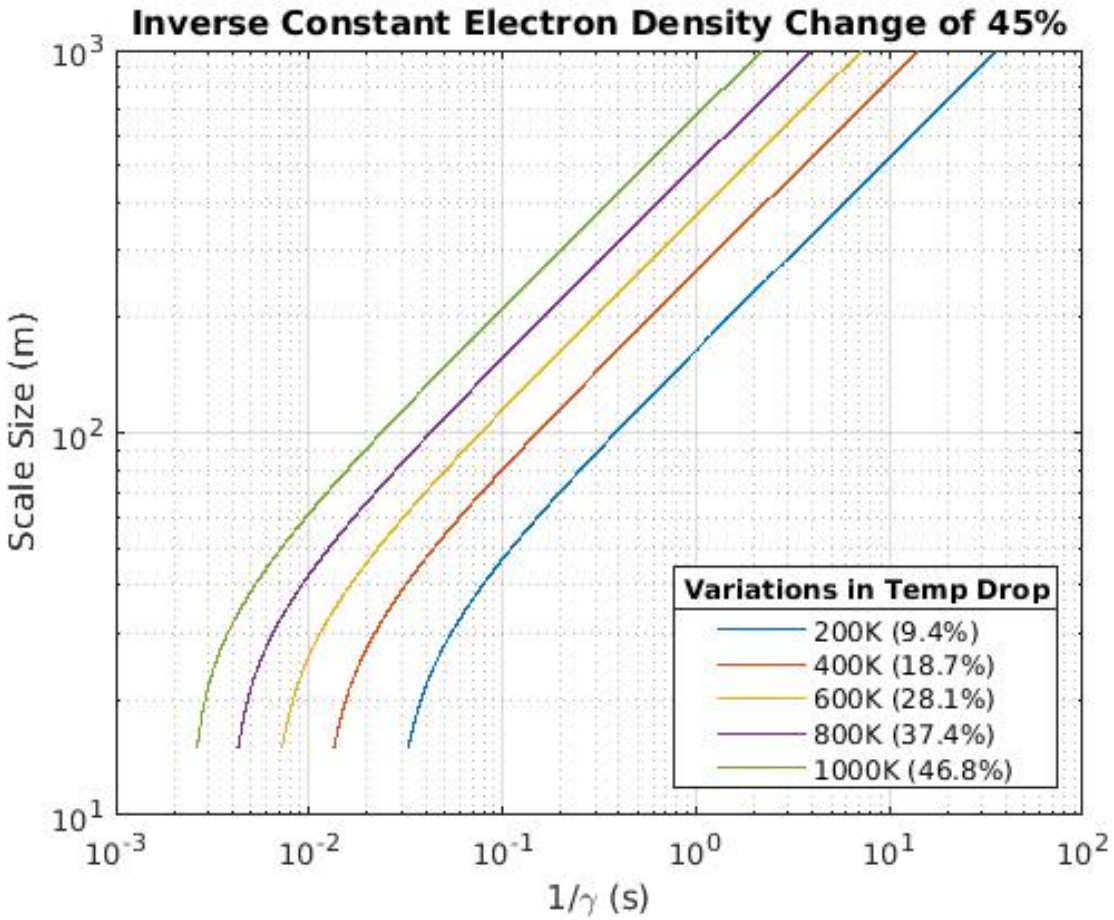

Figure A.6: Inverse temperature gradient instability growth rate by scale size with variations in electron temperature drop under a electron density drop of 45 percent.

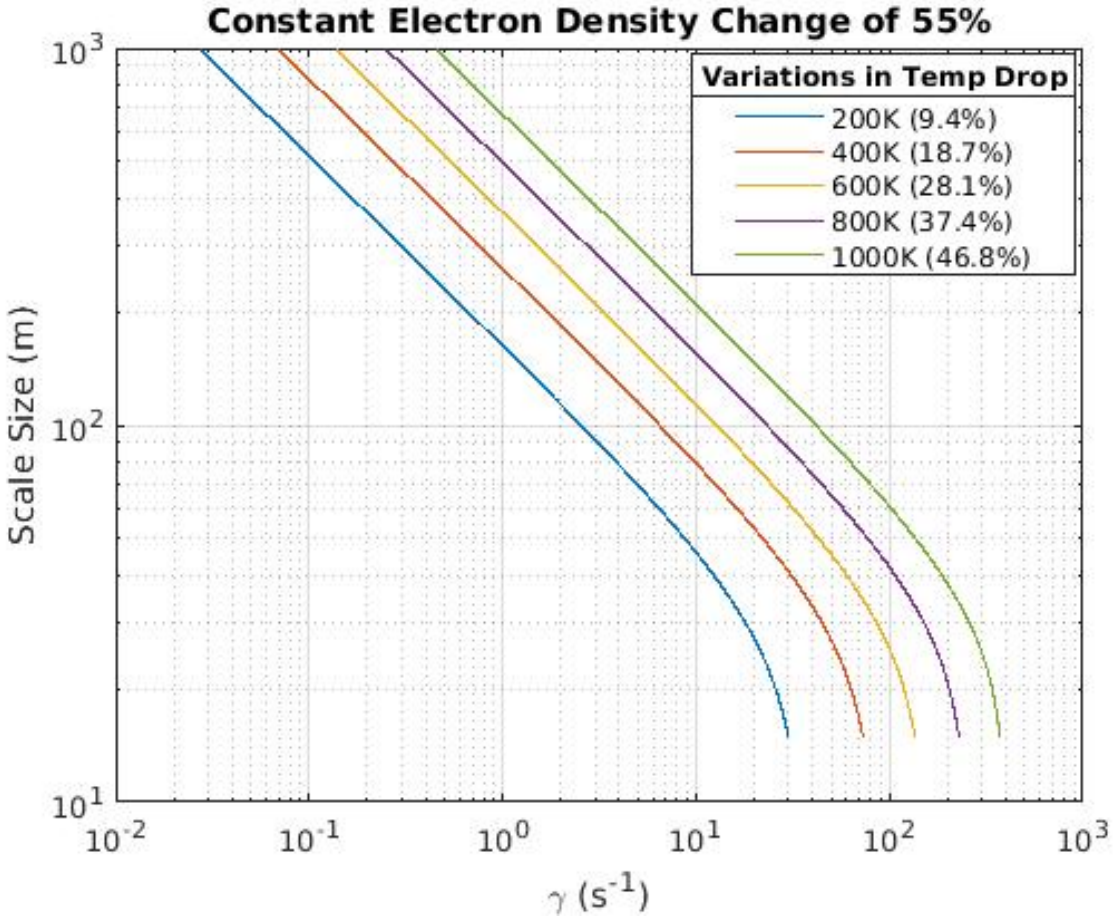

Figure A.7: Temperature gradient instability growth rate by scale size with variations in electron temperature drop under a electron density drop of 55 percent.

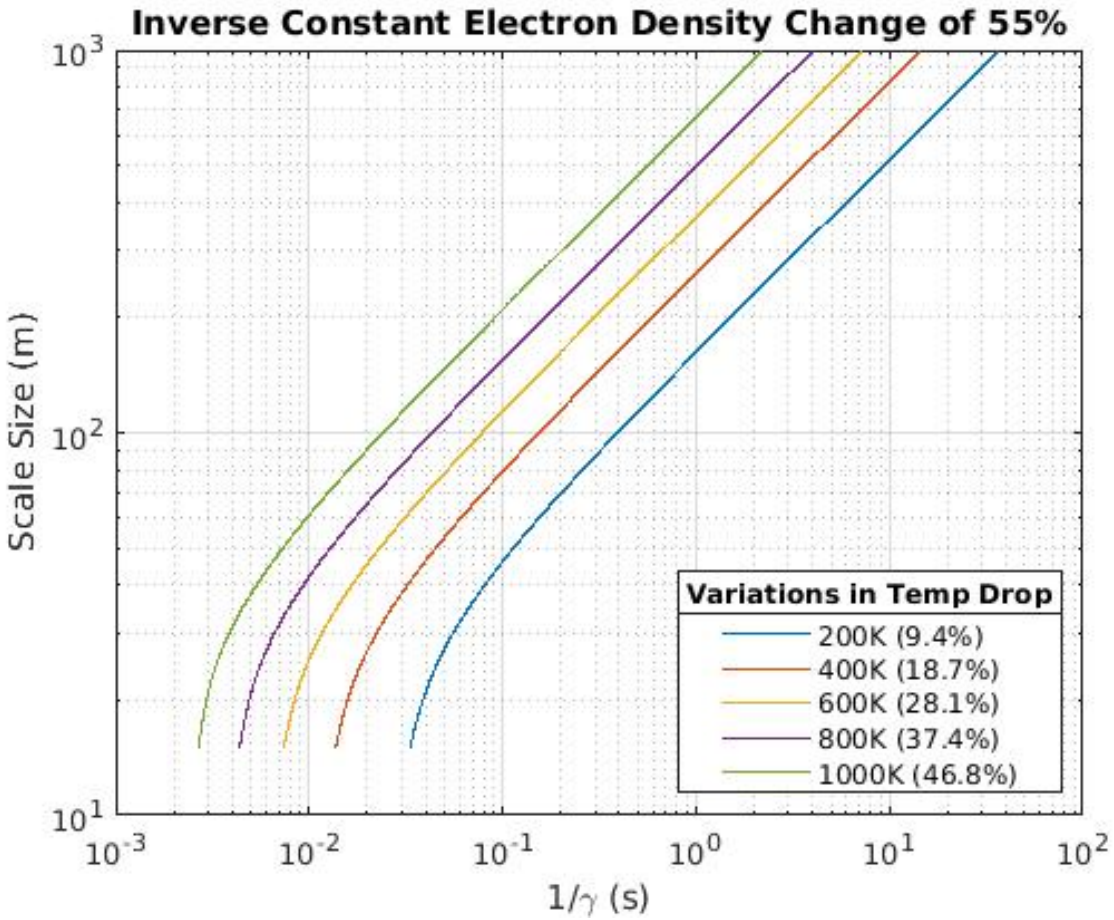

Figure A.8: Inverse temperature gradient instability growth rate by scale size with variations in electron temperature drop under a electron density drop of 55 percent.

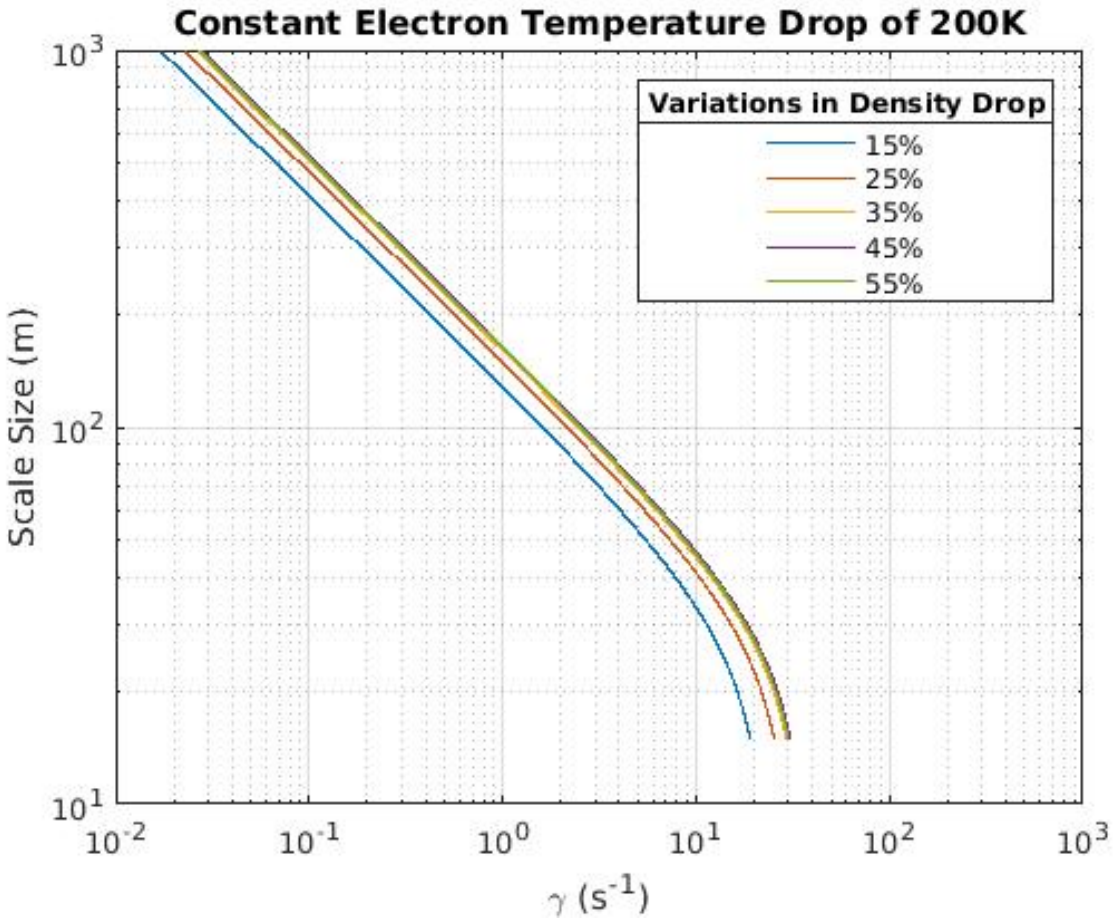

Figure A.9: Temperature gradient instability growth rate by scale size with variations in electron density drop under a electron temperature drop of 200 K.

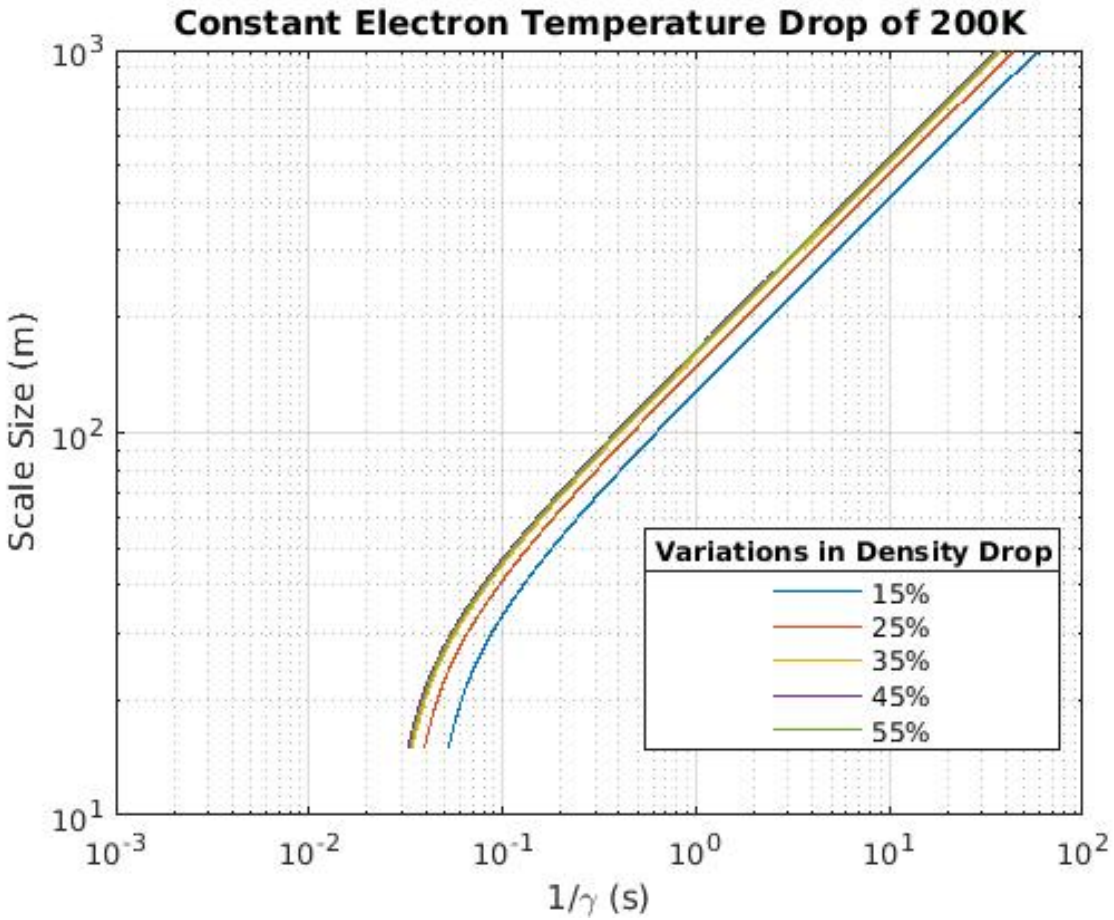

Figure A.10: Inverse temperature gradient instability growth rate by scale size with variations in electron density drop under a electron temperature drop of 200 K.

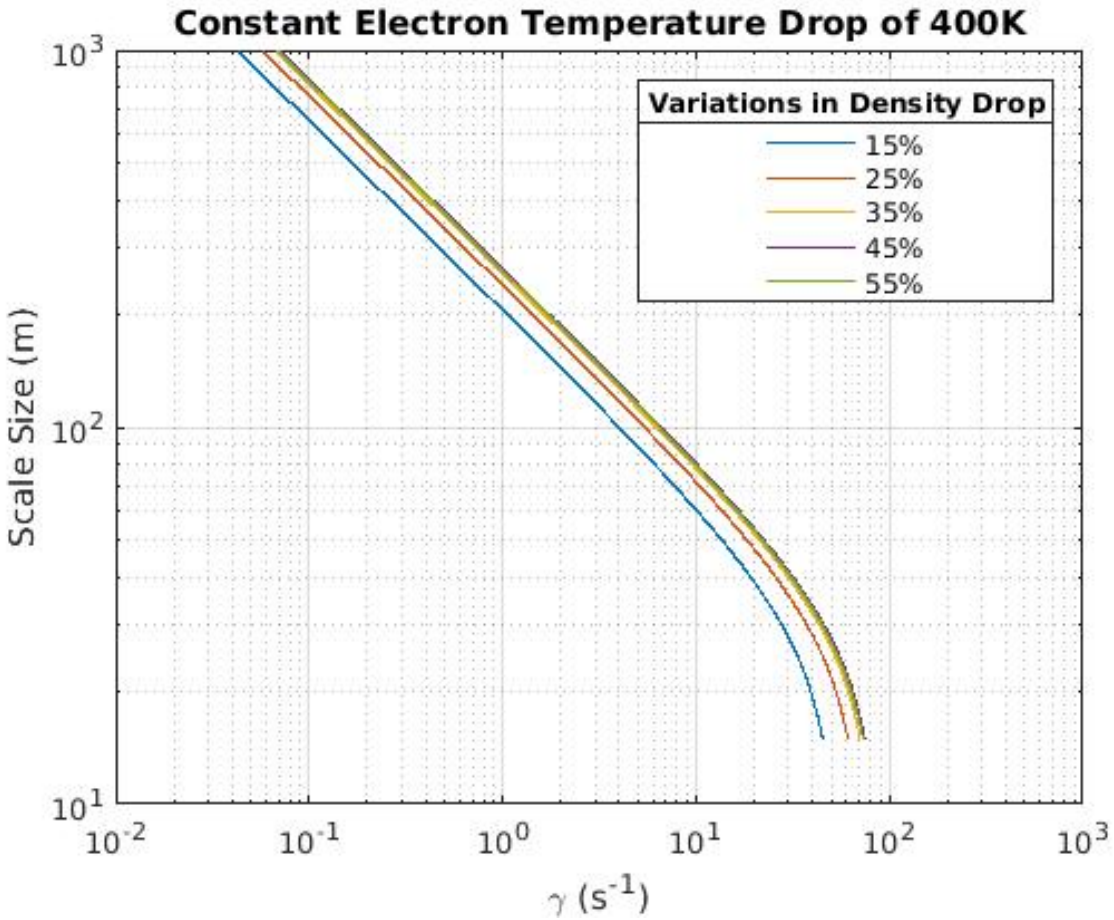

Figure A.11: Temperature gradient instability growth rate by scale size with variations in electron density drop under a electron temperature drop of 400 K.

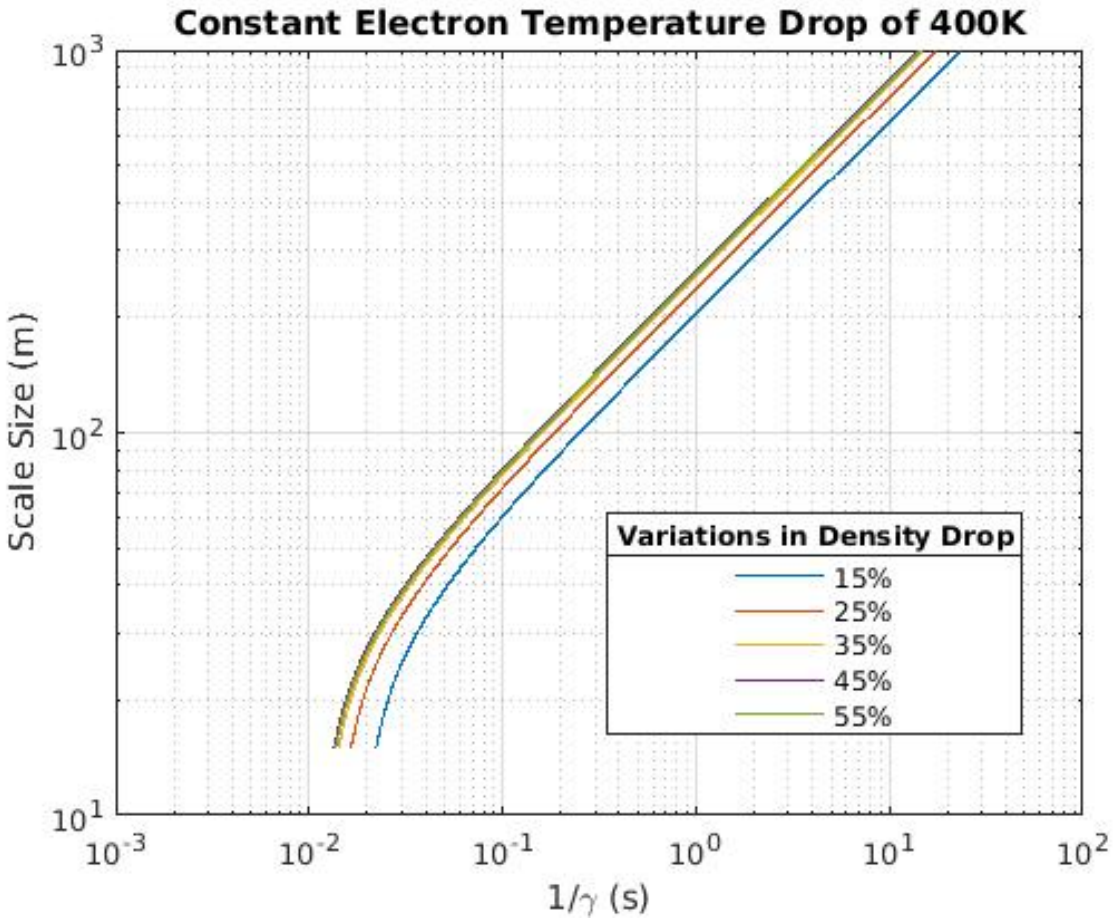

Figure A.12: Inverse temperature gradient instability growth rate by scale size with variations in electron density drop under a electron temperature drop of 400 K.

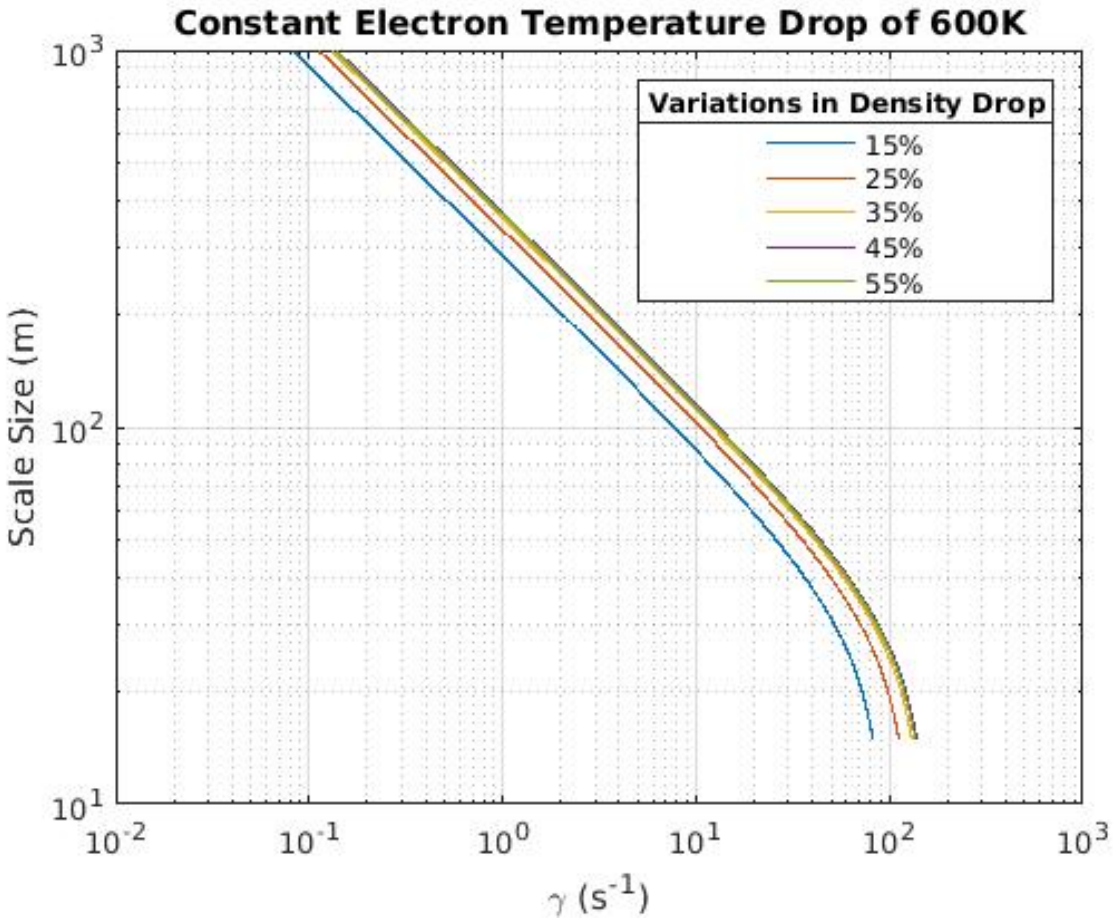

Figure A.13: Temperature gradient instability growth rate by scale size with variations in electron density drop under a electron temperature drop of 600 K.

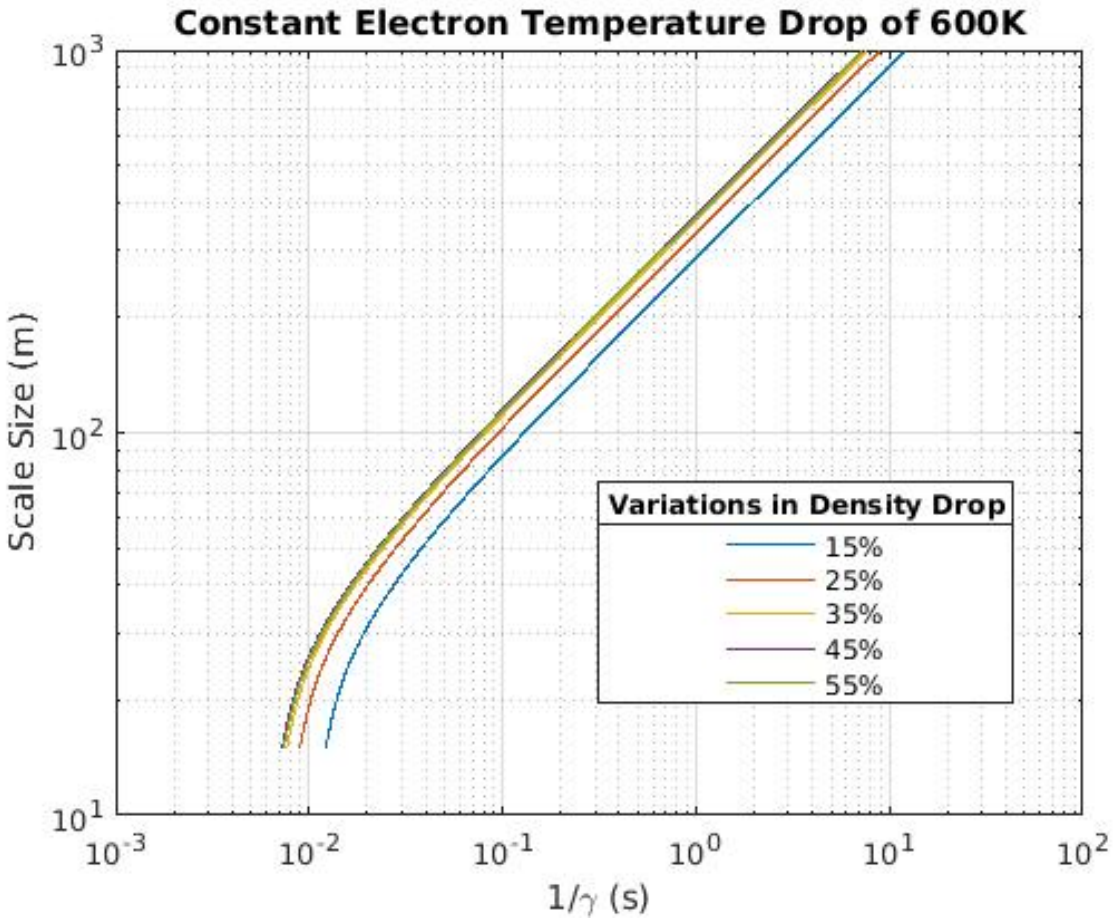

Figure A.14: Inverse temperature gradient instability growth rate by scale size with variations in electron density drop under a electron temperature drop of 600 K.

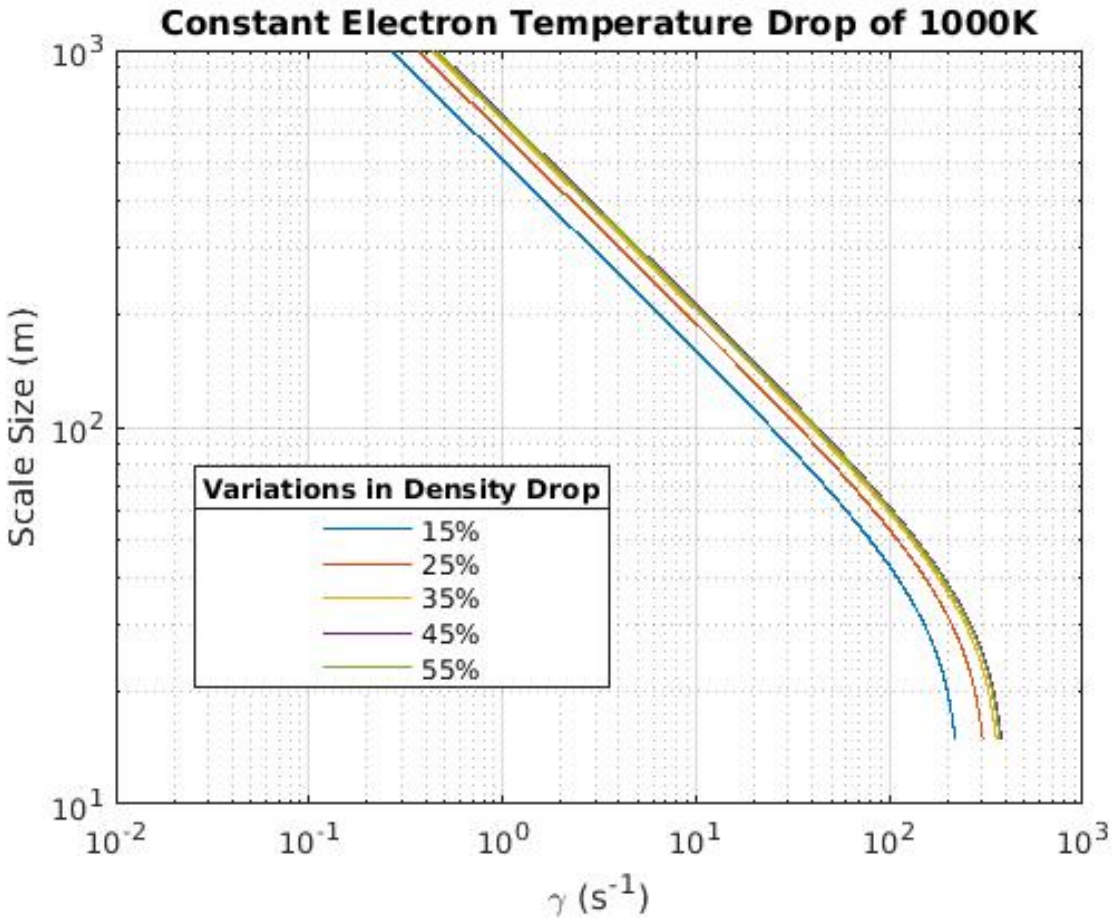

Figure A.15: Temperature gradient instability growth rate by scale size with variations in electron density drop under a electron temperature drop of 1000 K.

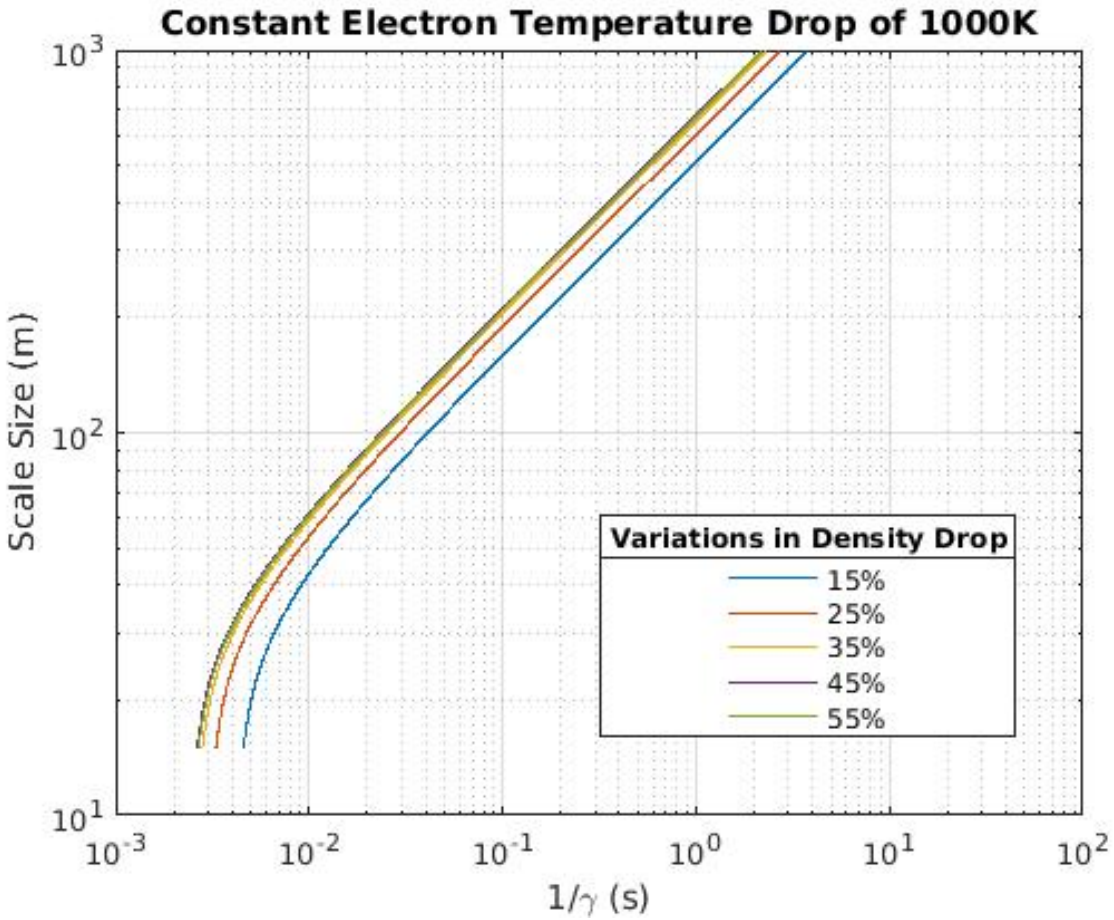

Figure A.16: Inverse temperature gradient instability growth rate by scale size with variations in electron density drop under a electron temperature drop of 1000 K.

Bibliography

[1] "Hathaway nasa/arc," https://solarscience.msfc.nasa.gov/, accessed: 2017-12-30.

[2] G. W. Prölss, *Physics of the Earths Space Environment: an Introduction*. New York: Springer-Verlag Berlin Heidelberg, 2004;.

[3] J. E. Allnutt, *Satellite-to-ground radiowave propagation*, 2nd ed. London: Institution of Engineering and Technology, 2012;, vol. 54.

[4] "Total solar eclipse: August 21, 2017," https://eclipse2017.nasa.gov/, accessed: 2017-06-10.

[5] J. M. Pasachoff, "2017 solar eclipse," *The Physics Teacher*, vol. 54, no. 2, pp. 68–68, 2016. [Online]. Available: http://dx.doi.org/10.1119/1.4940164

[6] M. E. Bakich, *What's All the Fuss About?* Cham: Springer International Publishing, 2016, pp. 1–5. [Online]. Available: http://dx.doi.org/10.1007/978-3-319-27632-8_1

[7] S. A. Bowhill, *Ionospheric Effects in Solar Eclipses*. Boston, MA: Springer US, 1970, pp. 3–17. [Online]. Available: http://dx.doi.org/10.1007/978-1-4684-1839-2_1

[8] J. O. Thomas, *The Earth's Exospheric Plasma with Some Comments on Eclipses as a Means of Studying the Ionosphere*. Boston, MA: Springer US, 1970, pp. 29–41. [Online]. Available: http://dx.doi.org/10.1007/978-1-4684-1839-2_3

[9] J. A. Kane, *D-Region Electron Density Measurements during the Solar Eclipse of May 20,1966*. Boston, MA: Springer US, 1970, pp. 199–210. [Online]. Available: http://dx.doi.org/10.1007/978-1-4684-1839-2_12

[10] J. O. Thomas and M. J. Rycroft, *Recent Ionospheric E and F Region Measurements during Solar Eclipses, and Their Interpretation*. Boston, MA: Springer US, 1970, pp. 237–251. [Online]. Available: http://dx.doi.org/10.1007/978-1-4684-1839-2_15

[11] M. Anastassiades, *The Annular Solar Eclipse on May 20 1966 and the Ionosphere*. Boston, MA: Springer US, 1970, pp. 253–271. [Online]. Available: http://dx.doi.org/10.1007/978-1-4684-1839-2_16

[12] A. A. Kovalev, A. G. Kolesnik, S. A. Kolesnik, A. A. Kolmakov, and R. R. Latypov, "Ionospheric effects of solar eclipses at midlatitudes," *Geomagnetism and Aeronomy*, vol. 49, no. 4, pp. 476–482, Aug 2009. [Online]. Available: http://dx.doi.org/10.1134/S0016793209040070

[13] S. S. De, B. K. De, B. Bandyopadhyay, B. K. Sarkar, S. Paul, D. K. Haldar, S. Barui, A. Datta, S. S. Paul, and N. Paul, "The effects of solar eclipse of august 1, 2008 on earth's atmospheric parameters," *Pure & Applied Geophysics*, vol. 167, no. 10, pp. 1273–1279, 10 2010, copyright - Springer Basel AG 2010; Last updated - 2014-08-09. [Online]. Available: http://login.ezproxy.lib.vt.edu/login?url=https://search-proquest-com.ezproxy.lib.vt.edu/docview/751529232?accountid=14826

[14] B. J. Adekoya, V. U. Chukwuma, and B. W. Reinisch, "Ionospheric vertical plasma drift and electron density response during total solar eclipses at equatorial/low latitude," *Journal of Geophysical Research: Space Physics*, vol. 120, no. 9, pp. 8066–8084, 2015, 2015JA021557. [Online]. Available: http://dx.doi.org/10.1002/2015JA021557

[15] I. Poole, "Radio waves and the ionosphere," http://www.arrl.org/files/file/Technology/pdf/119962.pdf,.

[16] F. Clette, L. Svalgaard, J. M. Vaquero, and E. W. Cliver, "Revisiting the sunspot number," *Space Science Reviews*, vol. 186, no. 1, pp. 35–103, Dec 2014. [Online]. Available: http://dx.doi.org/10.1007/s11214-014-0074-2

[17] G. W. Prölss, "Ionospheric storms at mid-latitude: A short review," in *Midlatitude ionospheric dynamics and disturbances*, J. M. Goodman, Ed., vol. 181. Naval Research Laboratory (U.S.), 2008, pp. 9–24.

[18] S. Bora, "Ionosphere and radio communication," *Resonance*, vol. 22, no. 2, pp. 123–133, Feb 2017. [Online]. Available: http://dx.doi.org/10.1007/s12045-017-0443-8

[19] W. G. Rees, *Physical principles of remote sensing*, 3rd ed. Cambridge: Cambridge University Press, 2013;.

[20] S. Priyadarshi, "A review of ionospheric scintillation models," *Surveys in Geophysics*, vol. 36, pp. 295–324, 2015.

[21] I. T. U. R. Sector, *Ionospheric propagation data and prediction methods required for the design of satellite services and systems*, 2012.

[22] K. Liu, G. Li, B. Ning, L. Hu, and H. Li, "Statistical characteristics of low-latitude ionospheric scintillation over china," *Advances in Space Research*, vol. 55, no. 5, pp. 1356 – 1365, 2015. [Online]. Available: http://www.sciencedirect.com/science/article/pii/S0273117714007388

[23] I. T. U. R. Sector, *The Global Ionospheric Scintillation Model (GISM)*, 2007.

[24] D. Rastogi and Vats, "Equatorial ionospheric scintillation in the indian zone," in *Effect of the Ionosphere on Space and Terrestrial Systems*, J. M. Goodman, Ed. Naval Research Laboratory (U.S.), 1978, pp. 14–24.

[25] A. S. H. A. Eltrass, "The mid-latitude ionosphere: Modeling and analysis of plasma wave irregularities and the potential impact on gps signals," Ph.D. dissertation, Virginia Polytechnic Institute and State University, 2015.

[26] P. M. Kintner, B. M. Ledvina, and E. R. de Paula, "Gps and ionospheric scintillations," *Space Weather*, vol. 5, no. 9, pp. n/a–n/a, 2007, s09003. [Online]. Available: http://dx.doi.org/10.1029/2006SW000260

[27] J. Mitola, "The software radio architecture," *IEEE Communications Magazine*, vol. 33, no. 5, pp. 26–38, May 1995.

[28] W. H. W. Tuttlebee, *Software defined radio: enabling technology.* New York: J. Wiley, 2002;.

[29] "Gnu radio," https://gnuradio.org/, accessed: 2017-06-10.

[30] J. Muslimin, A. L. Asnawi, A. F. Ismail, and A. Z. Jusoh, "Sdr-based transceiver of digital communication system using usrp and gnu radio," in *2016 International Conference on Computer and Communication Engineering (ICCCE)*, July 2016, pp. 449–453.

[31] C. Rathod, 4 2017, continuing work.

[32] W. A. Scales, A. Eltrass, J. M. Ruohoniemi, J. B. H. Baker, and P. J. Erickson, "Gps and radar data analysis of midlatitude ionospheric plasma wave irregularities," in *2016 United States National Committee of URSI National Radio Science Meeting (USNC-URSI NRSM)*, Jan 2016, pp. 1–2.

[33] A. Eltrass, A. Mahmoudian, W. A. Scales, S. deLarquier, J. M. Ruohoniemi, J. Baker, R. A. Greenwald, and P. J. Erickson, "Investigation of the temperature gradient instability as the source of midlatitude quiet time decameter-scale ionospheric irregularities: 2. linear analysis," *Journal of Geophysical Research: Space Physics*, vol. 119, no. 6, pp. 4882–4893, 2014. [Online]. Available: http://dx.doi.org/10.1002/2013JA019644

[34] A. Eltrass and W. A. Scales, "Nonlinear evolution of the temperature gradient instability in the midlatitude ionosphere," *Journal of Geophysical Research: Space Physics*, vol. 119, no. 9, pp. 7889–7901, 2014. [Online]. Available: http://dx.doi.org/10.1002/2014JA020314

[35] M. K. Hudson and M. C. Kelley, "The temperature gradient drift instability at the equatorward edge of the ionospheric plasma trough," *Journal of Geophysical Research*, vol. 81, no. 22, pp. 3913–3918, 1976. [Online]. Available: http://dx.doi.org/10.1029/JA081i022p03913

[36] R. A. Greenwald, K. Oksavik, P. J. Erickson, F. D. Lind, J. M. Ruohoniemi, J. B. H. Baker, and J. W. Gjerloev, "Identification of the temperature gradient instability as the source of decameter-scale ionospheric irregularities on plasmapause field lines," *Geophysical Research Letters*, vol. 33, no. 18, pp. n/a–n/a, 2006, l18105. [Online]. Available: http://dx.doi.org/10.1029/2006GL026581

[37] S. P. Gary, *Theory of space plasma microinstabilities*. New York: Cambridge University Press, 1993;.

[38] A. Eltrass, W. A. Scales, A. Mahmoudian, S. de Larquier, J. M. Ruohoniemi, J. B. H. Baker, R. A. Greenwald, and P. J. Erickson, "Investigation of the generation source of decameter-scale sub-auroral ionospheric irregularities during geomagnetically quiet periods," in *2014 XXXIth URSI General Assembly and Scientific Symposium (URSI GASS)*, Aug 2014, pp. 1–4.

[39] "Magnetic field calculators," https://www.ngdc.noaa.gov/geomag-web/?model=igrf, accessed: 2017-5-15.

[40] "International reference ionosphere," http://irimodel.org/, accessed: 2017-5-05.

[41] M. Moses and G. Earle, "Experiment design to assess ionospheric perturbations during a solar eclipse," 4 2017.

[42] "Space weather prediction center: National oceanic and atmospheric administration," http://www.swpc.noaa.gov/products/predicted-sunspot-number-and-radio-flux, accessed: 2017-06-20.

[43] J. M. Picone, A. E. Hedin, D. P. Drob, and A. C. Aikin, "Nrlmsise-00 empirical model of the atmosphere: Statistical comparisons and scientific issues," *Journal of Geophysical Research: Space Physics*, vol. 107, no. A12, pp. SIA 15–1–SIA 15–16, 2002, 1468. [Online]. Available: http://dx.doi.org/10.1029/2002JA009430

[44] S. Basu, S. Basu, J. Aarons, J. P. McClure, and M. D. Cousins, "On the coexistence of kilometer- and meter-scale irregularities in the nighttime equatorial f region," *Journal of Geophysical Research: Space Physics*, vol. 83, no. A9, pp. 4219–4226, 1978. [Online]. Available: http://dx.doi.org/10.1029/JA083iA09p04219

[45] M. C. Kelley, *The earth's ionosphere*. San Diego: Academic Press, 1989;, vol. 43rd.

[46] J. Huba and D. Drob, "Sami3 prediction of the impact of the august 21, 2017 total solar eclipse on the ionosphere/plasmasphere system," 3 2017.

[47] E. Afraimovich, E. Kosogorov, and O. Lesyuta, "Effects of the august 11, 1999 total solar eclipse as deduced from total electron content measurements at the gps network," *Journal of Atmospheric and Solar-Terrestrial Physics*, vol. 64, no. 18, pp. 1933 – 1941, 2002. [Online]. Available: http://www.sciencedirect.com/science/article/pii/S1364682602002213

[48] M. J. Keskinen, S. Basu, and S. Basu, "Midlatitude sub-auroral ionospheric small scale structure during a magnetic storm," *Geophysical Research Letters*, vol. 31, no. 9, pp. n/a–n/a, 2004, l09811. [Online]. Available: http://dx.doi.org/10.1029/2003GL019368

[49] "Inmarsat: Our coverage," http://www.inmarsat.com/about-us/our-satellites/our-coverage/, accessed: 2017-02-10.

[50] T. Pratt, C. Bostian, and J. Allnutt, *Satellite Communications*, 2nd ed. John Wiley & Sons, 2002.